Title
Metabolic Flux Signature Perturbations: Endoplasmic Reticulum Stress, Diet, and Aging

Author
Schneider, Catherine P

Publication Date
2021

Peer reviewed|Thesis/dissertation

Metabolic Flux Signature Perturbations: Endoplasmic Reticulum Stress, Diet, and Aging

By

Catherine P. Schneider

A dissertation submitted in partial satisfaction of the

requirements for the degree of

Doctor of Philosophy

in

Metabolic Biology

in the

Graduate Division

of the

University of California, Berkeley

Committee in Charge:

Professor Marc Hellerstein, Chair
Professor Andrew Dillin
Professor Denis Titov
Professor Anders Näär

Spring 2021

Abstract

Metabolic Flux Signature Perturbations: Endoplasmic Reticulum Stress, Diet, and Aging

by

Catherine P. Schneider

Doctor of Philosophy in Metabolic Biology

University of California, Berkeley

Professor Marc Hellerstein, Chair

The unfolded protein response in the endoplasmic reticulum (UPR^{ER}) is involved in a number of metabolic diseases, including non-alcoholic fatty liver disease. Here, we first characterize the UPR^{ER} induced metabolic changes in mouse liver through *in vivo* metabolic labeling and mass spectrometric analysis of proteome and lipid fluxes. We induced ER stress *in vivo* via tunicamycin treatment and measured rates of proteome-wide protein synthesis, *de novo* lipogenesis and cholesterol synthesis serially over a three-day period, thereby generating a metabolic "signature" of the UPR^{ER} over time. Synthesis of most proteins was suppressed under ER stress conditions, including proteins involved in lipogenesis, consistent with reduced *de novo* lipogenesis at 48 and 72 hours. The reduction in *de novo* lipogenesis was explicable by reduced food intake, shown in pair-feeding studies. Despite the lower *de novo* lipogenesis rates, electron microscopy revealed striking morphological changes to ER and H&E staining showed lipid droplet enriched livers under ER stress. Pre-labeling of adipose tissue prior to ER stress induction revealed mobilization of lipids from adipose to the liver. Interestingly, the source of these lipids in liver was uptake of free fatty acids, not whole triglycerides or phospholipids from lipoproteins, as demonstrated by replacement of the triglyceride-glycerol moiety in liver concurrently with increased incorporation of labeled palmitate from adipose tissue. We also induced ER stress by a high-fat diet and observed similar metabolic flux signatures, suggesting that this mechanism may play a role in the progression of fatty liver disease.

Using these same stable isotope labeling approaches, several changes in protein synthesis across ontologies were noted with age, including a more dramatic suppression of translation under ER stress in aged mice as compared to young mice. *De novo* lipogenesis rates decreased under ER stress conditions in aged mice, including both triglyceride and phospholipid fractions. In young mice, a significant reduction was only seen in the triglyceride fraction. These data indicate that aged mice have an exaggerated response to ER stress, which may indicate less effective mechanisms of protein clearance after inducing the UPR^{ER}. These flux-based approaches provide a powerful tool to identify novel regulators of ER stress and potential targets for pharmacological intervention.

We applied the same stable isotope labeling techniques to generate region-specific metabolic flux signatures of mouse brains. Assessing how metabolic flux signatures of the brain are perturbed through different interventions, including anti-aging therapeutics and preventative lifestyle interventions, could provide a powerful tool to assess cell-specific and region-specific changes with age, and provide a kinetic metric to assess intervention effectiveness.

Table of Contents

1. Introduction 1
1.1 Overview of the unfolded protein response in the endoplasmic reticulum 1
1.2 Aging and proteostasis 2
1.3 Dynamic proteomics and lipid kinetics 3
1.4 The aging brain 6
1.5 Summary 7

2. Metabolic flux signatures of the ER unfolded protein response *in vivo* reveal decreased hepatic *de novo* lipogenesis and mobilization of lipids from adipose tissue to liver 8
2.1 Introduction 8
2.2 Results 8
2.3 Discussion 17
2.4 Materials and Methods 36

3. Aging alters the metabolic flux signature of the ER unfolded protein response 40
3.1 Introduction 40
3.2 Results 41
3.3 Discussion 47
3.4 Materials and Methods 54

4. Region-specific shifts in metabolic flux in the aging brain 58
4.1 Introduction 58
4.2 Results 58
4.3 Discussion 69
4.4 Materials and Methods 70

5. Conclusion and Future Outlook 74

References 76

Acknowledgements

Although I have thoroughly enjoyed broadly learning the intricacies of metabolism, the endoplasmic reticulum, neuroscience, and their dysregulation during diseased states, the people I have worked with, learned from, and have been supported by in graduate school have made my experience at UC Berkeley so special.

Firstly, my lab. I am so grateful to have had Marc give me the opportunity to both have free reign over my project in the lab and pursue pretty much whatever sparked my curiosity, but also to support me in my pursuit of completing the requirements to become a registered dietitian concurrently during graduate school. As a fellow clinician, you challenged me to think about the bigger picture when reading papers and designing experiments and to think physiologically about an organism as a whole instead of just separated cells. The lab environment cultivated through collaborations with a myriad of scientists provided diverse learning experiences which I much enjoyed. I am so grateful for the support of my entire lab during the course of my PhD training. I will miss working at my bench in the lab and talking with Mark Fitch, Marcy, Edna, and Naveed about a cool paper one of us had read. I miss the daily support Katie Walker and I provided for each other at our neighboring desks, with many conversations about what I might be baking that weekend or a writing project she was pursuing to provide levity during long days in the lab. Hussein, Edna, and Mark Fitch, thank you for your patience and technical assistance in running my mass spec samples and for training me to analyze my data. Kelvin and Shubha, thank you for teaching me to analyze my data and helping me troubleshoot my data analysis and experimental approaches. Shubha, thank you especially for teaching me how to dissect mouse brains and for our neuroscience lessons. Hector, thank you for taking me under your wing in my early days in the lab and training me on mouse handling techniques and helping me study for my qualifying exam. Alec and Mo, thank you for the many conversations at the bench and always helping me out around the lab. Naveed, thank you for attempting to teach me how to code and helping me troubleshoot my data analysis in the lab, and for the many conversations that also distracted us from this. Marcy, I am so grateful for our friendship which grew from our many chats at our neighboring benches over the years. I so appreciate you listening to my anxieties, complaints, and accomplishments each day and for our many conversations about hiking and camping, cooking, the best type of gel for manicures, and countless other things to distract from dissecting mice or the alike. Lucy, Sam, John, Michael, and Rozalina - thank you for being the best undergraduate mentees I could ask for. Mentoring you all during graduate school was one of my favorite things about the lab and I am so lucky to have been able to teach such inquisitive and passionate budding scientists.

I am also so grateful for the support of my second mentor, Andy Dillin, for welcoming me to join your weekly lab meetings in which I was able to learn from and collaborate with your lab. Ashley, I am especially thankful for your guidance and mentorship. Thank you to the whole lab for your thoughtful feedback on my experiments, and for teaching me all about the UPR. I am also so grateful for my cycling friends I have made through the lab - Koning, Cory, and Melissa - our rides this past year when in-person time was so limited were always a highlight of my week.

Thank you to my dietetics mentors, Mikelle and Mary, for guiding me through the DPD program and answering all of my many questions. You both provided such support and inspiration for me during my program for which I am so grateful. I would not be at completing the UCSF dietetic internship this year if not for you. The clinical addition to my training has added a component which I really enjoy, so I am so grateful for your support and guidance as I navigated the next steps for what I envision my future career to entail.

Thank you to the rest of my thesis committee members, Denis Titov and Anders Näär, for providing feedback and encouragement throughout the duration of my PhD. I appreciate the many experiments and approaches you both suggested during thesis meetings which helped to guide my projects. Thank you to my qualifying exam committee members, James Olzmann, Joe Napoli, and Sona Kang for your guidance during the early stages of my project and helping to hone in on my critical thinking skills - crucial for the remainder of my graduate school career. Thank you to the entirety of the NST department for a community during graduate school which I was so happy to be a part of. Our department was small, but I always loved seeing smiling faces in the hallways and taking a minute to chat with you all in your labs as I came to borrow a reagent or use a piece of equipment. Thank you to my cohort - Clark, Diyala, Pete, and Kim, for support and community which were especially important those first years of grad school. Thank you to my friends I made during my lab rotations - Jessica Spradlin, Jessica Counihan, Charlie, Elizabeth, Melanie, Carl - thank you for support and laughs in and outside of the lab. Jessica Spradlin and Jessica Counihan, I am especially thankful for our friendship and for our bike rides this past year - as mentioned above - our rides this past year when in-person time was so limited were always a highlight of my week. Carl - thank you for the many many laughs over the past several years, friendship, and welcoming me into your family through introducing me to Fred.

Fred - thank you for being my biggest fan. Your support the past several years has helped me to grow as a scientist and as a person in general, and I am so thankful to have met you during graduate school. When we started dating right before I took my qualifying exam you were such a positive and supportive partner; I couldn't believe how lucky I was to have you in my life. That support only got greater as we have built our life together, and I am so lucky to have you by my side through it all. Whether it be an El Toyonal TT, or a long night of mouse dissections, I knew I could always count on you to support me. You help me to be the best version of myself. I am so thankful for the many ways in which you support me, including, but not limited to, technical and figure making support, cooking me dinner when I am tired after work, and listening to and supporting all of my aspirations. I am so excited to see what the future holds for our life together.

Mom and Dad - thank you for listening to me talk about science every night at dinner when I lived with you for the year before graduate school, and well, and throughout my whole childhood before that. You always helped cultivate my curiosity through the microscope, crystal growing kit, and alike Christmas presents. You always supported me and built me up through school and college, and had confidence in me as I applied to graduate schools. I am so lucky to have such supportive parents. Your faith in me helped me to develop confidence in myself to pursue my interests and dreams. I am so grateful for our family. Emily, Madeline, and Zachary - thank you for being the best siblings I could ask for. I always truly looked forward to making it home for the holidays to spend time with you guys, and am so thankful for the many laughs and memories we have together. On days an experiment would fail in the lab, or things wouldn't go as planned, I would look on my phone for pictures of us all together on a trip or fun memory because knowing I have all these amazing memories with you as my family could put things in perspective and put a smile back on my face. I am so appreciative for you all as my support network.

Gerty, Eric, Alice - thank you for welcoming me into your family and being so supportive. Our 'Sneaky's' group text put a smile on my face many days. I appreciate all of your support over the past few years, and am so grateful for you all as my new family.

Adam, Amy, and Dan - I am so thankful for you as my 'quarantine pod' over the last year. Our weekly dinners helped keep me sane and I am so grateful for you all as my friends. Allie, Amanda, Gabby, and Andie - I am so appreciative for you all as my Bay Area pod of friends when

I started graduate school, and continued friendship over Facetimes and calls after you all left the Bay. Our many hikes, yoga classes, and dinners and nights out in San Francisco and Berkeley provided much needed escapes from the academic world and space to take a step back and provide perspective outside of my scientist only world at school. Katie, Cassie, and Chelsea - thank you for always listening to me through our many Facetimes over the years. Your support, encouragement, and our laughs together helped me to push through when things were tough.

1. Introduction

Metabolism is complicated. Its many pathways and feedback loops are often dysregulated, leading to and exacerbating disease. During graduate school, I became especially interested in the intertwining of metabolism and diseases of aging. Some of my early projects focused on the aging brain in effort to better understand the region-specific metabolic differences that in the brain as organisms age. I later focused on applying these same techniques to the liver in effort to better understand the metabolic differences in diseased states, specifically, diseases characterized by protein misfolding.

Proteins carry out nearly all of the chemistry and much of the structural organization of cells. Proteins are long chains of small amino acids linked together and adopt unique folds that determine their function. Nearly one third of newly synthesized proteins are misfolded, necessitating assistance from molecules known as chaperones. The maintenance of proper protein folding and synthesis, also known as protein homeostasis, is essential for survival. Protein homeostasis is maintained by several mechanisms, including the endoplasmic reticulum unfolded protein response (UPR^{ER}). The UPR^{ER} includes changes in protein translation and membrane lipid synthesis in effort to combat the accumulation of misfolded proteins in the endoplasmic reticulum (ER), a cellular compartment responsible for distributing proteins to their correct location. The UPR^{ER} is thought to be a central pathway in the progression of several diseases, including both non- alcoholic fatty liver disease (NAFLD) and non-alcoholic steatohepatitis (NASH). Through better understanding the metabolic flux of diseases of aging and protein misfolding, we can identify novel regulators of ER stress and aging and potential targets for pharmacological intervention.

1.1 Overview of the unfolded protein response in the endoplasmic reticulum

Proteostasis, or protein homeostasis, is important in maintaining a healthy cellular environment under stressful conditions[1]. Dietary changes such as high intake of fatty acids or the accumulation of misfolded proteins can perturb proteostasis and thereby initiate the endoplasmic reticulum unfolded protein response (UPR^{ER})[2–4]. The role of the UPR^{ER} in metabolic diseases such as non-alcoholic fatty liver disease has been hypothesized to be due to dysregulation of lipid homeostasis but remains poorly understood[5–8]. In this work, we characterized metabolic flux changes of UPR^{ER}, including rates of lipid synthesis and protein synthesis across the proteome.

The UPR^{ER} consists of three arms, led by ER-membrane-anchored IRE1α, PERK, and ATF6. In times of ER stress, BiP, a key chaperone, moves away from the ER membrane to combat the accumulation of misfolded protein and activates these three arms[9] (figure 1.1). Hallmarks of the UPR^{ER} include suppressed global protein translation with the exception of key ER stress responders such as chaperones[10]. Although these responses have been characterized at the mRNA and protein concentration level, rates of protein synthesis (translation rates) in response to induction of the ER stress response *in vivo* remain unmeasured. Here we used heavy water labeling to measure newly synthesized proteins after tunicamycin-induced ER stress in mice. As synthesis of most proteins is suppressed under ER stress conditions, identifying any upregulated exceptions is a powerful tool to identify novel features or regulators of ER stress. Translation rate also may shift over time, and which proteins are synthesized at different points after ER stress induction has not yet been established.

Another hallmark of the UPR^{ER} is thought to be an increase of lipogenesis to facilitate the

expansion of ER lipids. This has been studied mostly in cell culture models[11]. Controversy about this canonical pathway exists, however, as it has been shown *in vivo* that lipogenic gene expression is reduced in mice under ER stress[12,13]. Increase in lipogenesis under ER stress conditions may be important in providing added surface for resolution of ER protein synthetic stress through re-folding and clearance of misfolded proteins in the ER lumen[14], but other metabolic sources could be responsible for increases in ER lipids, especially in living animals.

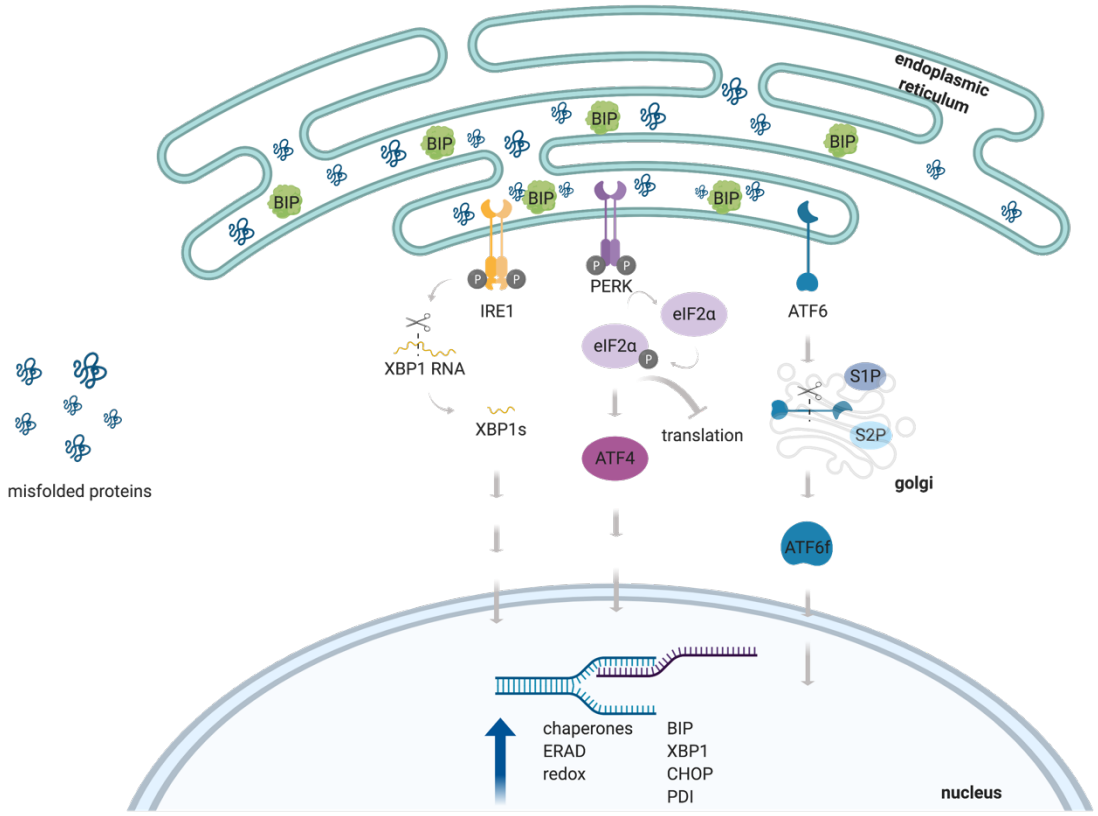

Figure 1.1. Overview of UPR^{ER}.

1.2 Aging and proteostasis

Age is a risk factor for numerous diseases, including neurodegenerative diseases, cancers, and diabetes. Loss of protein homeostasis, or proteostasis, is a central hallmark of aging and may explain why certain diseases become manifest as organisms grow older[15]. Although the UPR has been implicated to decline with age in *C. elegans*[16], among other organisms, it is not fully understood how age induced shifts in metabolism may impair an organisms' ability to handle proteotoxic stress. In this work, we characterized how metabolic flux changes of UPR^{ER}, including rates of lipid synthesis and protein synthesis across the proteome, shift with age.

1.3 Dynamic proteomics and lipid kinetics

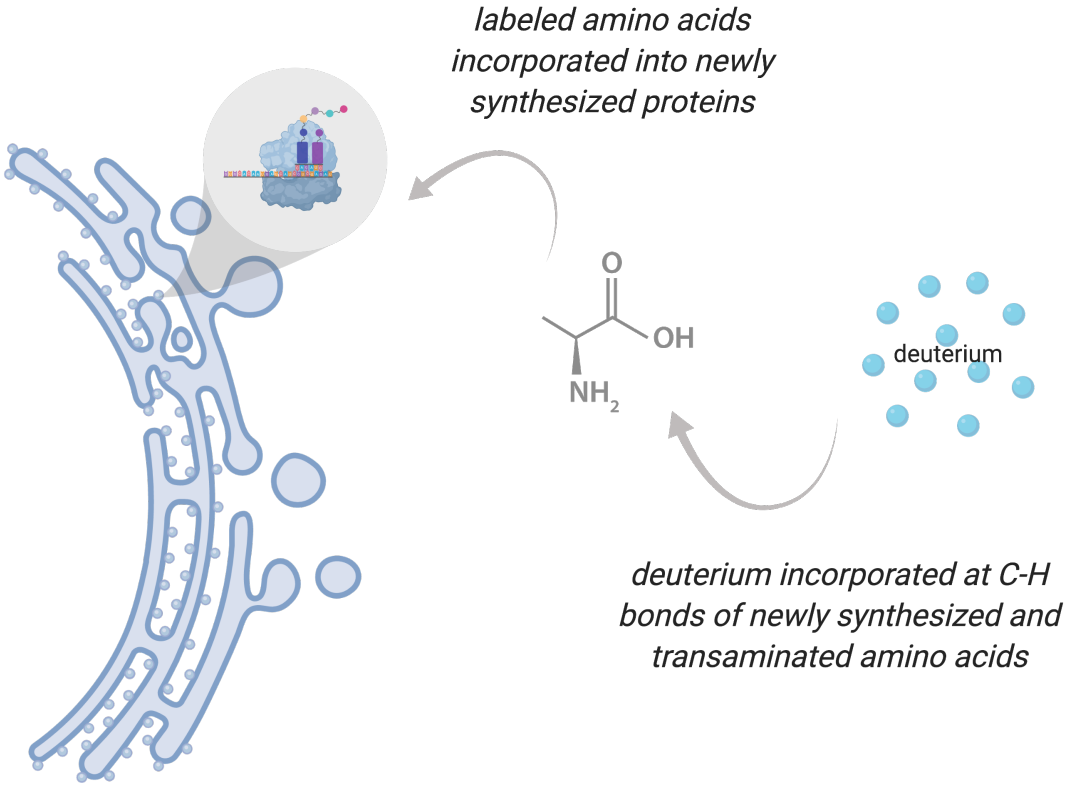

Figure 1.2 a) Schematic of deuterium incorporation into newly synthesized proteins.

Stable isotope labeling is a powerful technique for quantifying translational dynamics *in vivo*. To measure protein synthesis rates, mice are labeled with deuterated water (heavy water, D_2O) beginning at time point 0 (t^0) until the end of the experiment. Proteins synthesized after t^0 will incorporate deuterium-labeled amino acids, thus enabling the measurement of proteins synthesized during the period of exposure to heavy water (figure 1.2). Deuterium is rapidly incorporated throughout the body of an organism after treatment and can be maintained through the intake of ^2H_2O in drinking water, thus making it an optimal labeling approach for *in vivo* experimental study. To provide an environment by which deuterium is available to be incorporated into newly synthesized proteins and lipids, mice are initially injected intraperitoneally (IP) with 100% ^2H_2O containing either drug for treatment, or vehicle control. This brings the percent enrichment in the body water of the animal to around 5%. To maintain this level of deuterium enrichment, mice are provided with deuterated drinking water over the duration of the labeling period. Mice are sacrificed after from several hours to days after t^0, at which point tissues of interest are collected. Determining the enrichment of each individual organism is important for calculating the degree of deuterium incorporation into amino acids used in protein synthesis. To determine the exact percent of deuterium enrichment in the body water of the animal, water is first distilled from liver tissue and used to assess percent enrichment with deuterium through an acetone transfer method. Hydrogen and deuterium from the body water will exchange with the hydrogen on acetone, which is used for GCMS analysis to determine overall deuterium body water enrichment of each animal to calculate percent palmitate enrichment. These values are needed to calculate the

probability that deuterium would be incorporated into each amino acid chain or lipid as they are being synthesized. Fractional synthesis rate (FSR) of proteins at time t (treatment period) is measured as the fraction (f) of new protein synthesized.

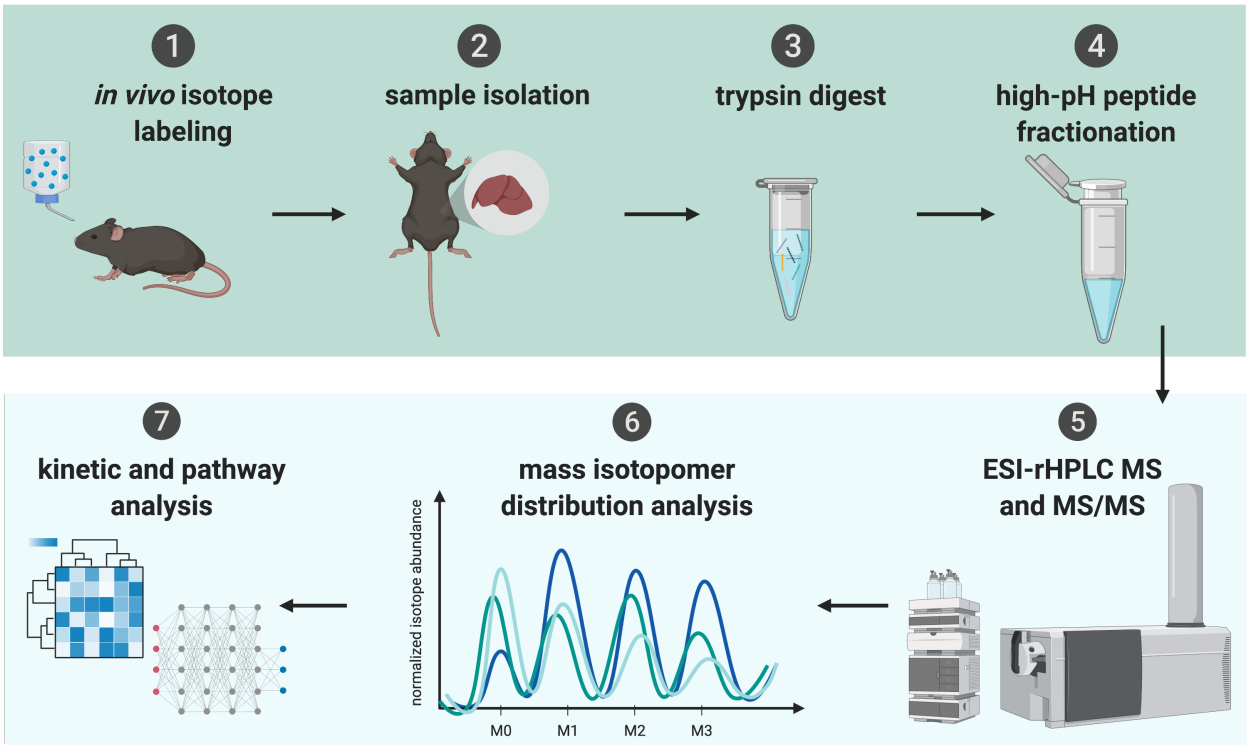

Figure 1.3. a) Experimental overview of dynamic proteomics approach. b) Experimental overview of measurement of *de novo* lipogenesis.

To prepare tissue samples for mass spectrometry analysis, samples are homogenized and used for in-solution digest preparation for liquid chromatography mass spectrometry analysis (LCMS/MS). Incorporation of deuterium into newly synthesized proteins is analyzed by using reversed-phase liquid chromatography coupled to tandem mass spectrometry (rHPLC– MS/MS) for peptide identification and rHLPC–MS for measurement of stable isotope enrichment and labeling pattern. These mass spectrometric data sets in combination with each organism's percent body water enrichment can be used to calculate fractional synthesis rates of proteins. The calculation model involves application of Mass Isotopomer Distribution Analysis (MIDA), or combinatorial probabilities of deuterium incorporation in polymerized amino acids[17–19]. Every amino acid has a defined number of hydrogen atoms in C-H bonds that are derived from or exchange with solvent water in cells and thus are capable of being enriched in the presence of D_2O. Measurement of D_2O enrichment in body water, the 'background concentration' of exchangeable deuterium, allows calculation of the likelihood that a hydrogen of an amino acid will exchange with a deuterium prior to being incorporated into a protein. These combinatorial probability calculations are used to calculate protein replacement rates (figure 1.3). Through this methodology developed by our lab, I was able to identify variances in fractional synthesis rates across the proteome to uncover diet and age related differences in protein synthesis rates with and without

UPR^{ER} induction. To better understand my data as a whole, I grouped proteins into KEGG gene ontology pathways and analyzed changes in synthesis rates across pathways and categories.

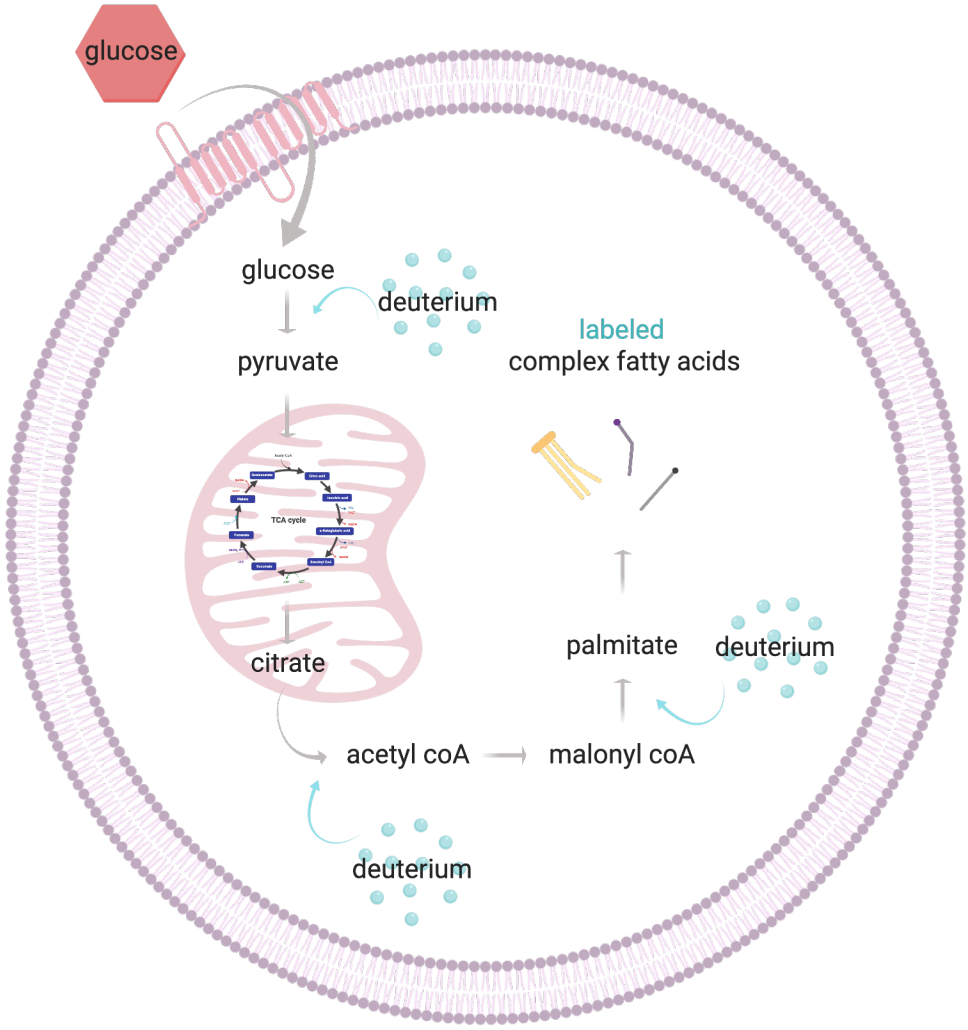

Figure 1.4. Schematic of deuterium incorporation into newly synthesized lipids.

To measure rates of lipid synthesis, I employed a similar labeling approach. Using gas chromatography mass spectrometry (GCMS), I was able calculate palmitate deuterium enrichment in each sample to determine rates of *de novo* lipogenesis *in vivo*[20]. As lipids are synthesized, (figure 1.4) deuterium is incorporated into fatty acids, such as palmitate. Through measuring palmitate enrichment with deuterium, I could assess synthesis rates of palmitate in selected lipid species of interest. To prepare samples for GCMS analysis, a chloroform methanol extraction was used to isolate lipids from mouse tissue. I then separated out lipid species of interest, including triglycerides and phospholipids, via TLC plate, followed by GCMS quantitation of each species of interest (figure 1.5).

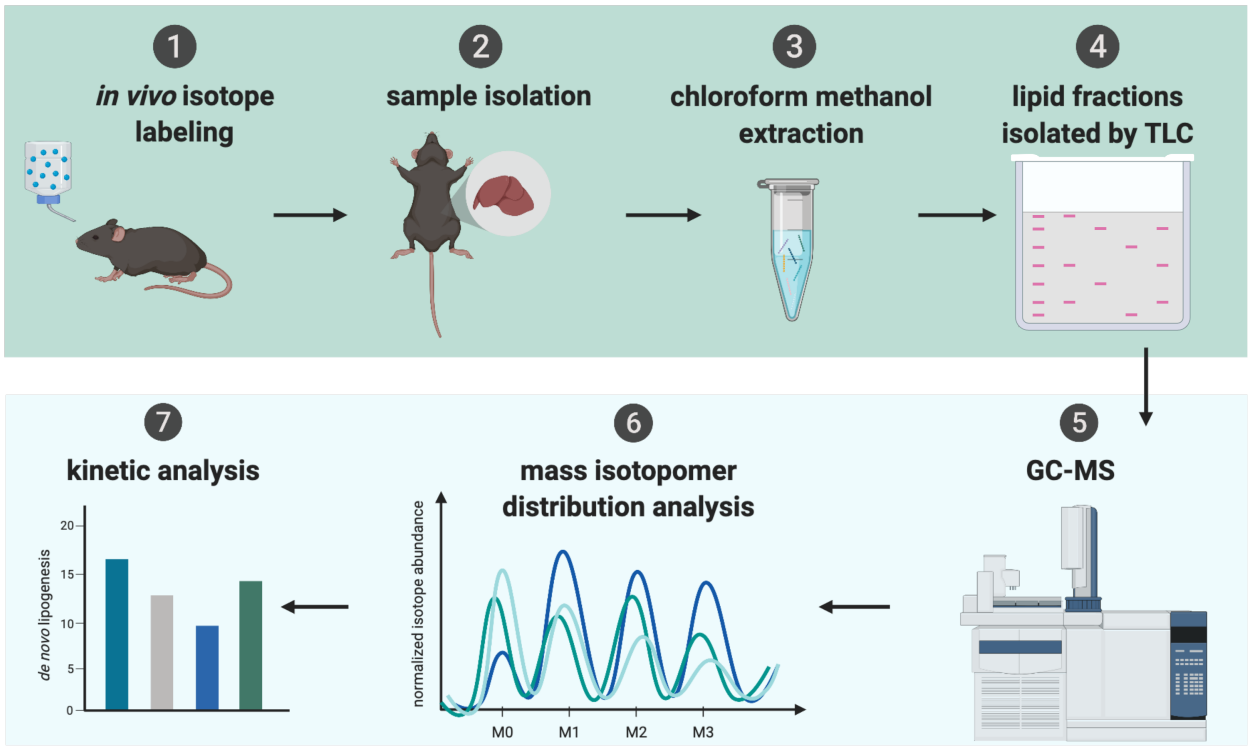

Figure 1.5. Experimental overview of measurement of *de novo* lipogenesis.

1.4 The aging brain

Aging is a known risk factor for the increase of neurodegenerative disease[21]. Though there are many phenotypes associated with the decline in cognition - ranging from increased permeability of the blood brain barrier leading to neuroinflammation[22] to broad dysregulation of metabolism [23] - a main hallmark of aging includes decreased ability to maintain proteostasis[15]. Cells lose their ability to clear damaged proteins due to changes in translation rates which leads to a decrease in the production of chaperones and loss of function of protein degradation machinery. Proteasome dysfunction and downregulation of autophagic response with aging is another problem with protein clearance, increasing accumulation of protein inclusions. In the brain, decline in proteasome activity has been seen with aging in the cerebral cortex and hippocampus. These changes in protein clearance mechanisms can lead to increased protein aggregation, UPR^{ER} induction, and apoptosis if dysfunction in protein clearance continues due to decreased efficiency of the proteostasis mechanisms as age increases[24–26]. Dysregulation of proteostasis can lead to buildup of potentially toxic protein aggregates, inducing neuronal cell death, thus increased rates of protein misfolding neurodegenerative diseases with age. For example, Alzheimer's disease pathogenesis occurs with the dysregulation of amyloid-β and tau, α-synuclein dysregulation has been observed in Parkinson's disease, Huntington's disease displays late onset generation of protein inclusion bodies caused by mutant huntingtin protein, and motor neuron degeneration occurs in ALS due to protein misfolding and aggregation[27–29]. Though many phenotypes have been

identified in the aging brain, we still lack effective therapeutic strategies to combat aging, including dysregulation of proteostasis and metabolic changes.

Location and cell type are important in understanding these metabolic and proteostasis changes that occur in aging, especially in an organ as complex as the brain. In this work we characterized changes in metabolic flux signatures that occur in the aging brain to better understand regional differences in both global proteome wide protein synthesis and lipid synthesis as organisms age, and assess differences across regions. Through quantifying which proteins are being translated at slower or faster rates with age in specific regions, we can assess which pathways are perturbed with aging through KEGG-pathway analysis.

1.5 Summary

In this work, I applied stable isotope labeling and mass spectrometry to quantify protein and lipid synthesis rates across a range of stress-inducing conditions in a mouse model, including age and tunicamycin induced ER stress. The data generated reveal organ specific metabolic flux signatures to understand both at the biomolecule level and KEGG-pathway specific variances across age and stress induction. Through quantifying both lipid synthesis and protein translation rates, we can assess kinetic changes occurring acutely after stress induction for a metabolic snapshot into the complexities of stress response. With this information, we can better design future therapeutic approaches to combat stress and aging.

2. Metabolic flux signatures of the ER unfolded protein response *in vivo* reveal decreased hepatic *de novo* lipogenesis and mobilization of lipids from adipose tissue to liver

2.1 Introduction

We were curious how lipogenesis rates change over time after ER stress induction *in vivo* and how this might be integrated with changes in protein translation rates. We used heavy water labeling to measure rates of *de novo* lipogenesis, cholesterol synthesis, and protein synthesis rates across the proteome in the liver over a three-day labeling period after tunicamycin-induced ER stress. We performed RNA-seq on the liver tissue to compare mRNA levels to rates of protein synthesis and lipogenesis. We report a decline in lipogenesis by all these metrics: reduced *de novo* lipogenesis and cholesterol synthesis flux rates, reduced synthesis rates of lipogenic proteins, and reduced expression of lipid-synthesis related genes. Even so, electron microscopy and hematoxylin and eosin staining visualized lipid accumulation and changes in ER membrane morphology over this time course. To explain the metabolic source of hepatic lipid accumulation, we then labeled adipose triglycerides by long-term heavy water administration prior to ER stress induction and allowed body water label to die-away. We demonstrate that the lipids incorporated into ER membranes or that accumulate in lipid droplets during ER stress in the liver *in vivo* are mobilized from other tissues and taken up as non-esterified fatty acids.

2.2 Results

RNA-seq of mouse liver under induced ER stress reveals decreased expression of genes involved in lipid and cholesterol synthesis

To investigate what happens over the time following initiation of the UPR^{ER}, we used tunicamycin to induce ER stress in mice and took liver samples over the subsequent three days (figure 2.1a). RNA-seq of the liver tissue revealed many significant changes, including decreased expression of genes involved in lipid synthesis, cholesterol metabolism, and glutathione synthesis. Upregulated ontologies included genes involved in response to ER stress, ERAD, and ribosome biogenesis (figure 2.1b-g). Expression of genes involved in the UPR^{ER} shift over time post ER-stress induction (figure 2.1b-f).

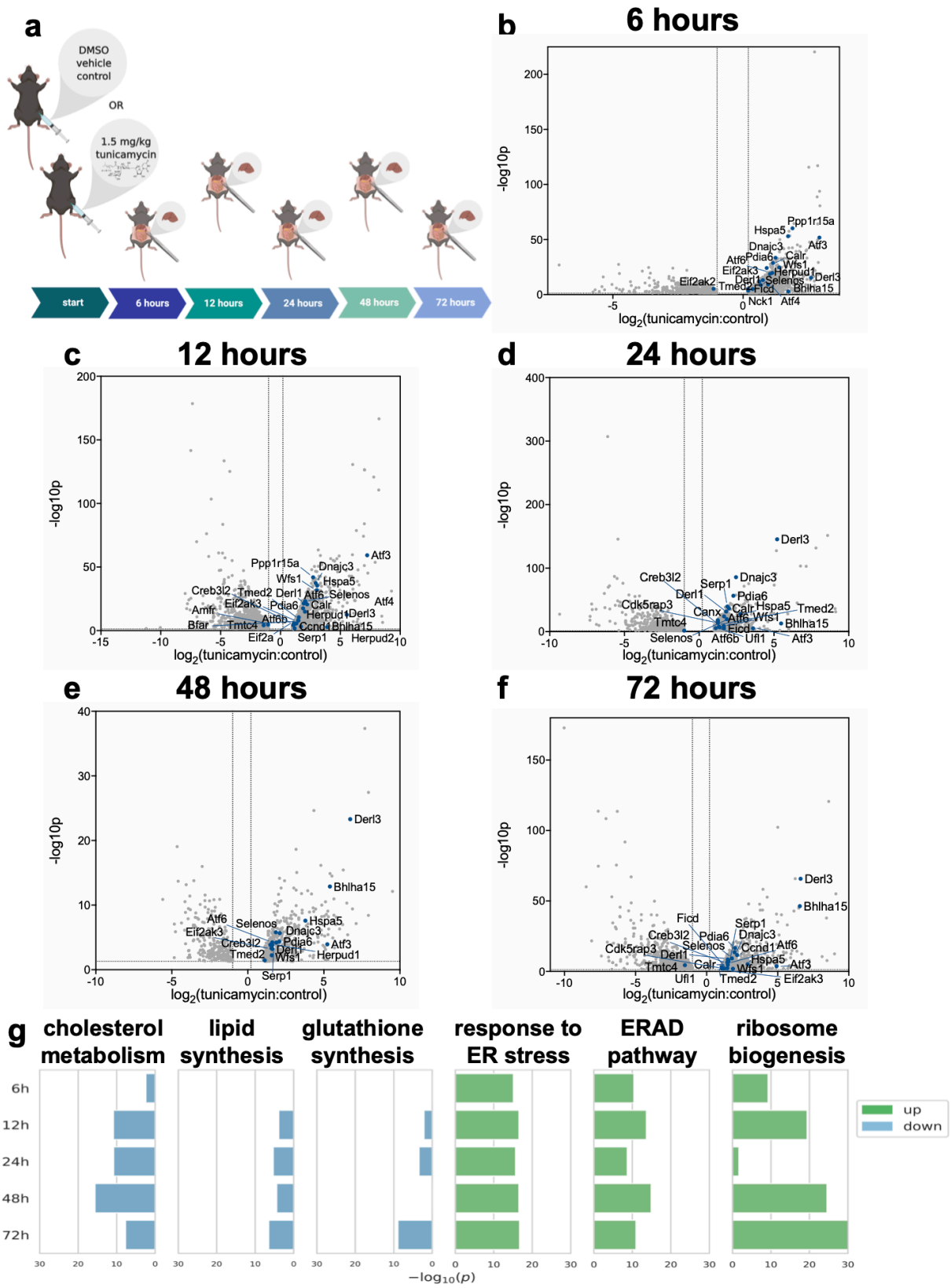

Figure 2.1. (a) Experimental overview. Mice (n=5 per group) were treated with either DMSO or 1.5 mg/kg tunicamycin. Tissues were taken 6-72 hours post-treatment. (b-f) Volcano plot of all genes for which RNA-seq

measured expression. Points expressed as log2 fold-change tunicamycin treated/control on x-axis and - log10(p-value), obtained from 2-tailed t-test, on y-axis. (g) GO (gene ontology) analysis for genes for which tunicamycin treatment significantly changed gene expression. GO-terms indicate groups for which a significant number of genes where changed in relation to the remainder of the data set for each time point. GO with significant decreased gene expression: cholesterol metabolic process (GO: 0008203), lipid biosynthetic process (GO: 0008610), glutathione biosynthetic process (GO: 0006749). GO with significant increased gene expression: response to ER stress (GO: 0034976), ERAD pathway (GO: 0036503), ribosome biogenesis (GO: 0042254).

Dynamic proteomics measurements reveal decreased global protein synthesis rates, including those involved in lipid synthesis but not key UPR^{ER} proteins

We asked whether protein translation rates would match the trends identified via RNA-seq using the dynamic proteomic approach[19] to measure translation rates of proteins after UPR^{ER} induction. Deuterated water was administered concurrently with tunicamycin to label nascent proteins that were translated over the three-day treatment period. During the first 12 hours post-tunicamycin, synthesis rates of most proteins measured were suppressed, with the exception of proteins involved in ER stress, including BiP, protein disulfide isomerases, and other chaperones (figures 2.2a-f). Proteins for which translation rates were significantly increased or decreased with induction of ER stress as compared to controls were organized into KEGG-pathways for analysis (figure 2.2g). Synthesis of proteins involved in fatty acid metabolism were decreased starting at 6 hours post tunicamycin treatment (figure 2.2g), as were most proteins characterized as being involved in "metabolic pathways". By 12 hours post treatment, some protein translation rates began to recover, while others remained reduced through 48 hours. Most protein synthesis rates returned to baseline values at the final time point measured, 72 hours (figure 2.2g). KEGG-pathway analysis revealed significantly increased synthesis rates of proteins involved in protein processing in the ER from the 12-hour time point continuing to the 72-hour time point, which can be attributed to the many chaperones and other UPR^{ER} responders. In particular, BiP showed a marked increase in synthesis rate at earlier time points, and though trending down over time, remained elevated at 72 hours (figure 2.2c). KEGG pathway analysis showed markedly decreased synthesis rates of proteins involved in lipid metabolism at 24 and 48 hours (figure 2.2g). Decreased synthesis of proteins involved in glutathione synthesis matched the decline observed in the RNA-seq data (figure 2.1b, figure 2.2g). Proteins involved in ribosomal biogenesis were also increased at the 48-hour timepoint, matching the RNA-seq data (figure 2.1b, figure 2.2g).

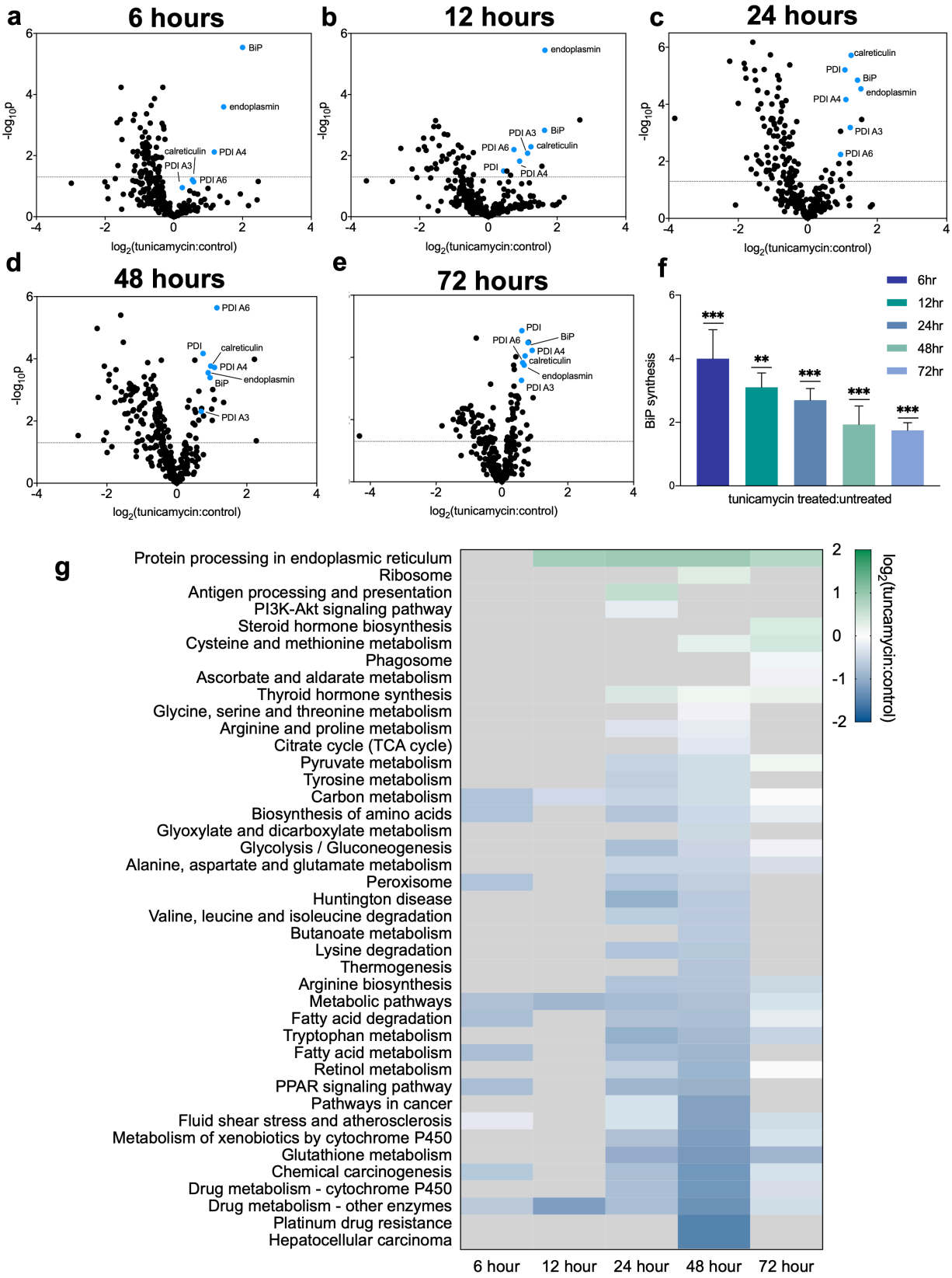

Figure 2.2. (a-f) Volcano plot of all proteins for which fractional synthesis rates were measured 12-72 hours post tunicamycin treatment. Points expressed as log2 fold-change tunicamycin treated/control on x-axis and - log10(p-

value), obtained from 2-tailed t-test, on y-axis. (f) ratio of protein translation rates of BiP in tunicamycin treated/control. ns= no significance, * = <0.05, ** = <0.01, *** = <0.001. (g) KEGG-pathway analysis for fractional synthesis rates of significant (p=<0.05 per 2-tailed t-test) proteins from tunicamycin treated/control. n=at least 5 proteins per pathway.

Changes in ER morphology by electron microscopy

We asked how the decline of gene expression and protein synthesis rates of lipid synthesis proteins correlated with ER membrane expansion reported by other groups under ER stress conditions[14]. Electron microscopy was carried out to visualize liver taken at each time point over the three-day treatment period. We observed distinct morphological changes to ER structure beginning at 12 hours post-tunicamycin treatment and continuing through the 72-hour endpoint. ER in the control samples presented as stacked and ribosome studded, as expected, whereas the ER observed in the tunicamycin-treated animals appeared like bubbles, or cobblestone, and appeared to be barren of the usual ribosomes (figure 2.3a).

ER stress induced lipid accumulation by histology

Hematoxylin and eosin (H&E) staining of liver taken from mice treated with tunicamycin or DMSO revealed lipid accumulation in the liver starting at 48-hours post ER stress induction. Earlier time points revealed no lipid differences as compared to controls (figure 2.3b).

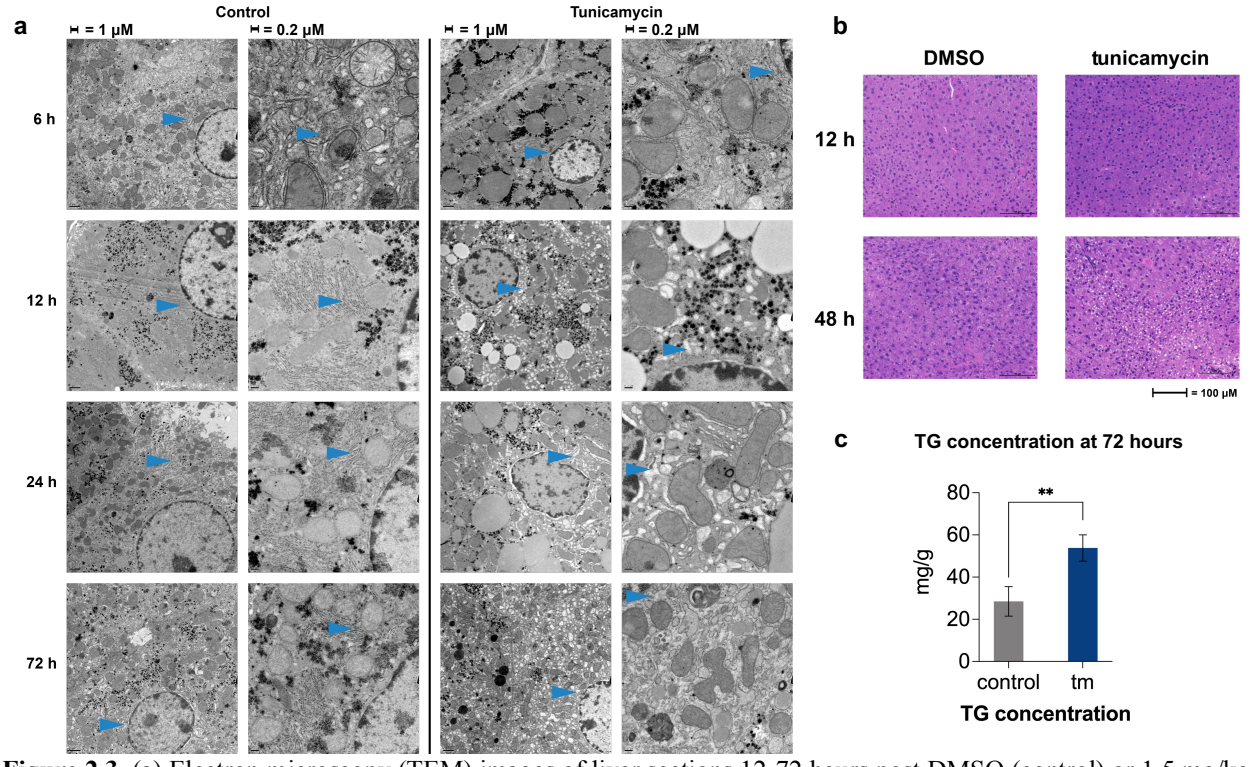

Figure 2.3. (a) Electron microscopy (TEM) images of liver sections 12-72 hours post DMSO (control) or 1.5 mg/kg tunicamycin treatment. Arrows point out ER in both treated and control to highlight changes in morphology. (b) H&E staining of liver sections 12 and 48 hrs post DMSO or 1.5 mg/kg tunicamycin treatment. (c) Concentration of triglycerides in mouse liver post DMSO (control) or 1.5 mg/kg tunicamycin treatment. (Tm=tunicamycin-treated).

Lipid and cholesterol synthesis rates decreased at later time points post-ER stress induction

Due to the striking morphological changes, we asked if lipids in the newly expanded ER membrane and droplets were coming from *de novo* synthesis. This was measured from the heavy water

labeling of fatty acids in phospholipids and triglycerides and in free and esterified cholesterol[31]. The contribution from *de novo* lipogenesis to palmitate in hepatic triglycerides and phospholipids was significantly decreased in both fractions beginning at 48-hours post tunicamycin treatment and continued through the last time point at 72-hours (figure 2.4a-b). *De novo* synthesis of both free and esterified cholesterol in the liver was also significantly decreased at 48 and 72-hours post ER stress initiation (figure 2.4c), consistent with the significant decline in expression of cholesterol synthesis genes in liver.

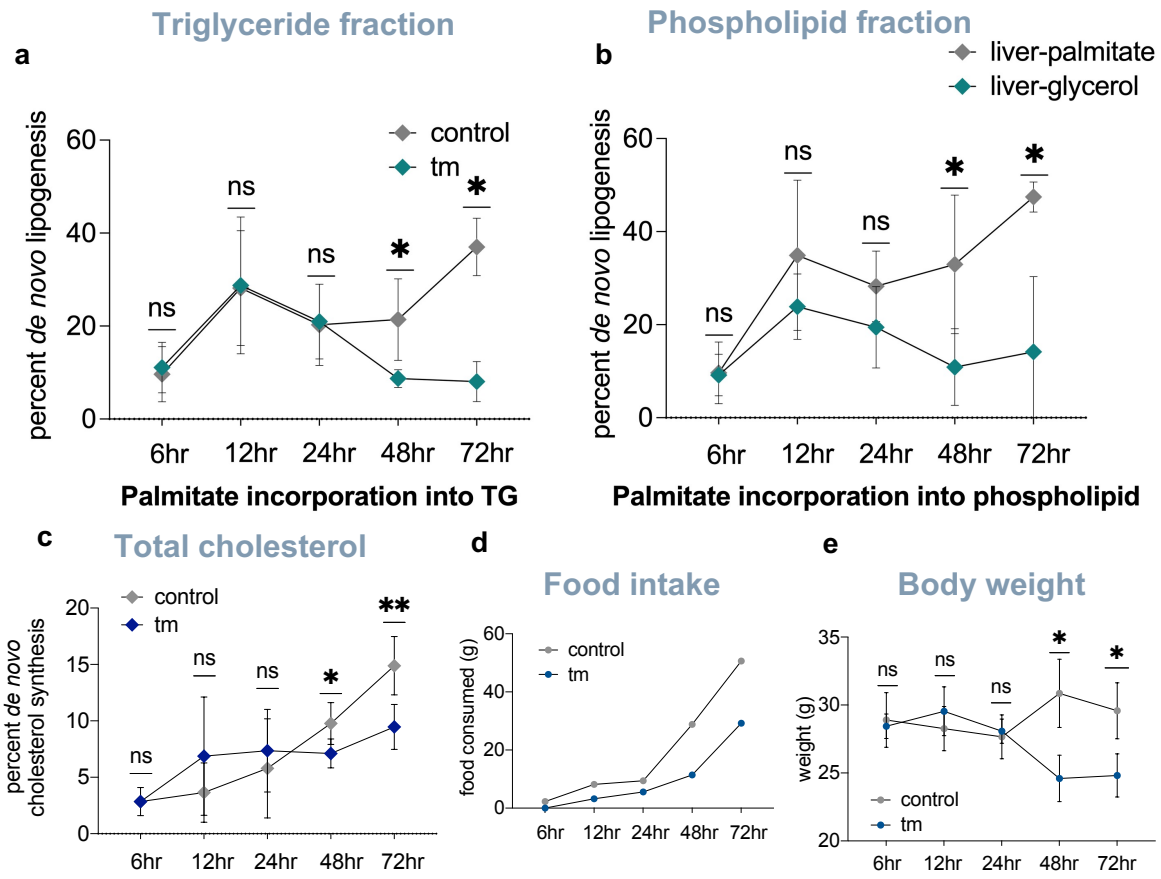

Figure 2.4. *De novo* lipogenesis rates of palmitate incorporated into triglycerides in control and tunicamycin treated mice 12-72 hours post treatment (n=5 per group). (b) *De novo* lipogenesis rates of palmitate incorporated into phospholipids in control and tunicamycin treated mice 12-72 hours post treatment (n=5 per group). (c) *De novo* cholesterol synthesis (free and esterified) rates in control and tunicamycin treated mice 12-72 hours post treatment (n=5 per group). (d) Food intake in mice control and tunicamycin 12-72 hours post treatment (n=5 per group). (e) Average body weight of control and tunicamycin treated mice 12-72 hours post treatment (n=5 per group). ns= no significance, * = <0.05, ** = <0.01, *** = <0.001.

Mobilization of lipids from adipose tissue to liver under ER stress conditions

To answer the question of where lipids in the liver were coming from if not from *de novo* synthesis, we devised a protocol to pre-label extrahepatic triglycerides (i.e., primarily adipose tissue lipid stores) prior to inducing ER stress. Mice were given deuterated water for 7 weeks to incorporate newly synthesized fatty acids into adipose tissue. We then discontinued heavy water intake for 2

weeks to allow deuterium enrichment to die away in body water and in liver triglycerides, which have much shorter half-lives than triglycerides in adipose tissue[32] (figure 2.5).

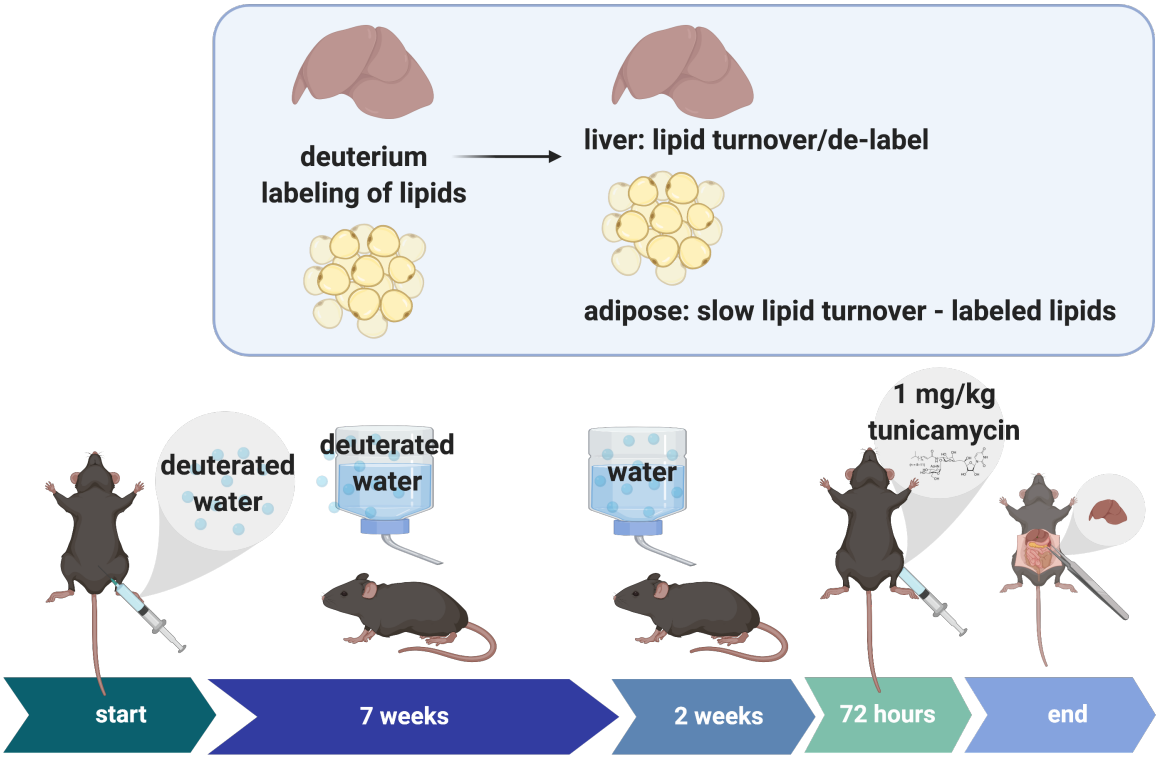

Figure 2.5. Experimental overview of pre-labeling experiment.

After tunicamycin-induced ER stress, deuterium enrichment of palmitate in hepatic triglycerides increased whereas deuterium enrichment of palmitate in adipose tissue triglycerides decreased compared to controls (figure 2.6a-c), consistent with lipid mobilization from adipose tissue to the liver. Additionally, we observed a reduction in enrichment of glycerol in phospholipids in the liver, indicating that intact phospholipids were rapidly turned over to the free glycerol level under ER stress conditions (figure 2.6d). A decline in triglyceride-glycerol enrichment in the liver concurrently with increased palmitate enrichment indicates that pre-existing hepatic triglycerides were hydrolyzed free fatty acids and free glycerol, not to the level of mono- or di-glycerides, and that the influx of palmitate is in the form of free fatty acids as opposed to transport of whole triglycerides or phospholipids from lipoproteins (figure 2.6c-d).

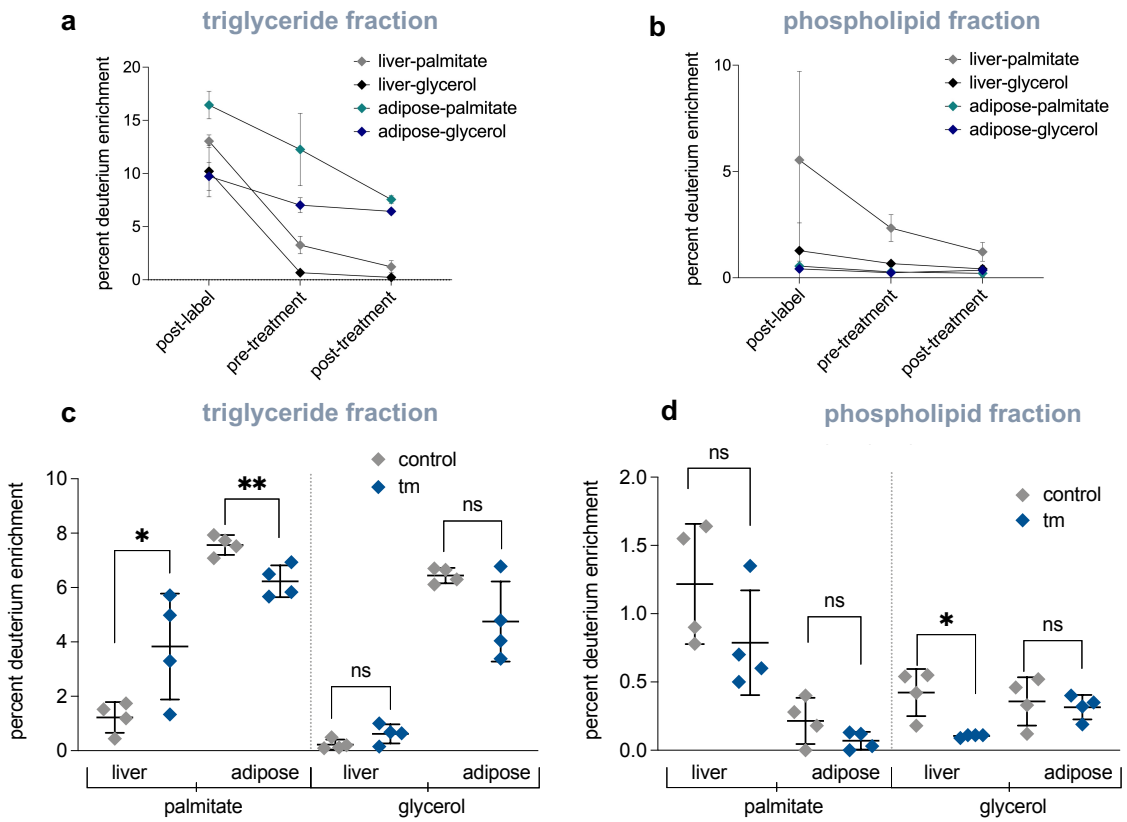

Figure 2.6. (a) Pre-labeling of triglycerides in control (DMSO) mice: percent deuterium enrichment of palmitate incorporated into triglycerides after 7 weeks of deuterium labeling (post-label), after a 2-week label free period (pre-treatment), and post 72-hour treatment period (n=3 per group). (b) Pre-labeling of phospholipids in control (DMSO) mice: percent deuterium enrichment of palmitate incorporated into phospholipids after 7 weeks of deuterium labeling (post-label), after a 2-week label free period (pre-treatment), and post 72-hour treatment period (n=3 per group). (c) Percent deuterium incorporated into palmitate and glycerol of triglycerides found in the liver or adipose after control (DMSO) or 1.5 mg/kg tunicamycin treatment after 72 hours (n=4 per group). (d) Percent deuterium incorporated into palmitate and glycerol of phospholipids found in the liver or adipose after control (DMSO) or 1.5 mg/kg tunicamycin treatment after 72 hours (n=4 per group). ns= no significance, * = <0.05, ** = <0.01, *** = <0.001.

Diet induced changes to protein and lipid metabolic flux signatures

To understand if this metabolic signature of was conserved under other models of UPR^{ER}, such as lipotoxicity, we used prolonged high-fat diet to induce ER stress *in vivo* (figure 2.7a), and also combined high-fat diet with tunicamycin treatment to determine their additive effects on the ER stress response. High-fat diet alone led to an overall increase in translation rates proteome wide, with many canonical UPR^{ER} proteins being significantly upregulated in their translation rates (figure 2.7c-d). We also saw a decrease in *de novo* lipogenesis rates in both triglyceride and phospholipid fractions through high-fat diet induced ER stress (figure 2.7b). When high-fat diet was coupled with tunicamycin stress induction, protein synthesis rates were mostly suppressed with the exception of canonical UPR^{ER} proteins (figure 2.7e-f), and an exaggerated decrease in *de novo* lipogenesis rates in both triglyceride and phospholipid fractions was seen (figure 2.7g).

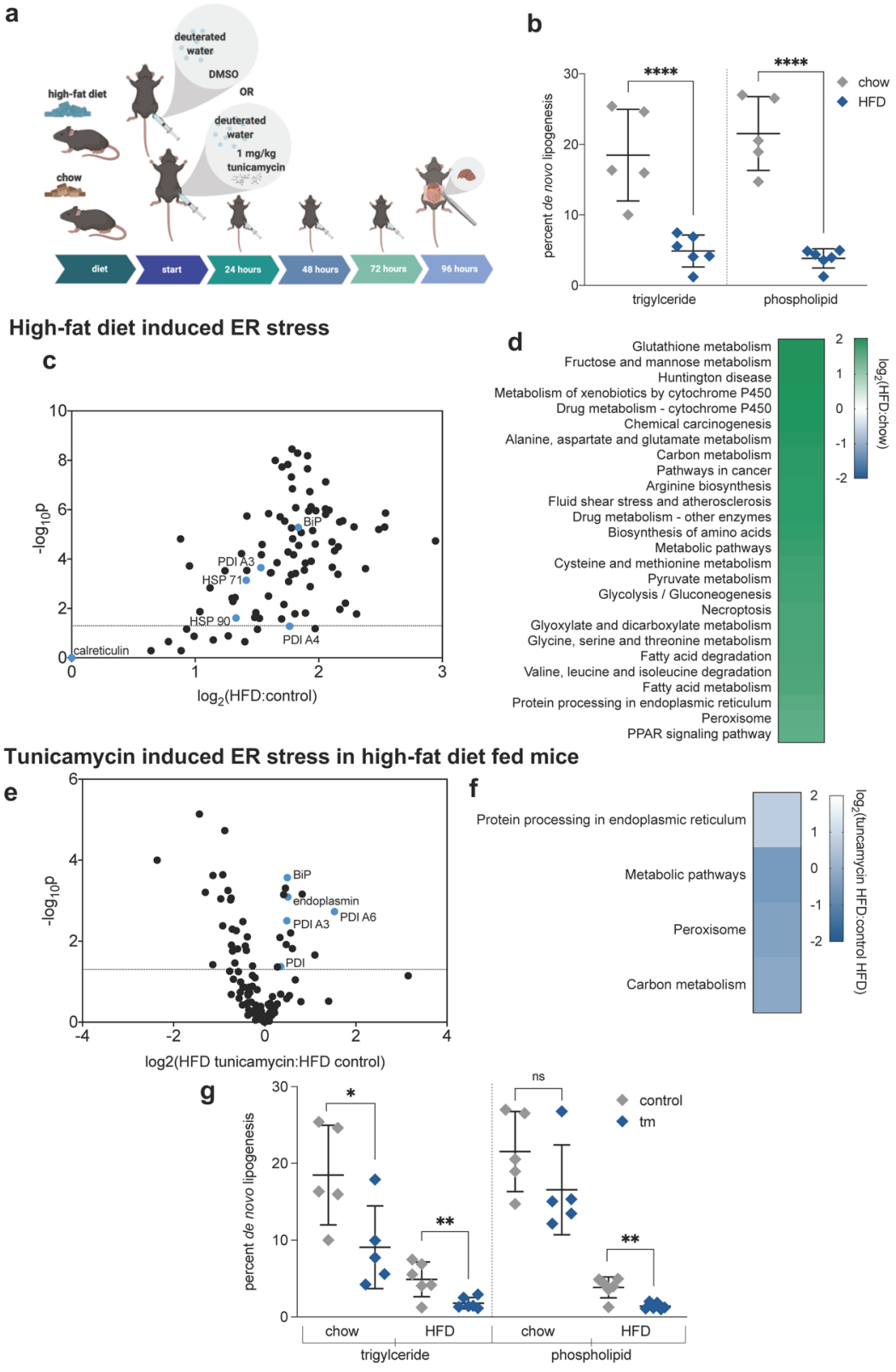

Figure 2.7. High-fat diet induced ER stress and effect of high-fat diet on ability to handle additive tunicamycin induced ER stress. All data from mouse livers. (a) Experimental overview: mice were given high-fat or chow diet for

6 weeks. Mice were challenged with a dose of 1 mg/kg tunicamycin daily until samples were taken at 96-hours post initial treatment. (b) Percent *de novo* lipogenesis of palmitate in high-fat diet compared to chow fed mice in both triglycerides and phospholipids. (c) Volcano plot of all proteins for which fractional synthesis rates were measured 96 hours after deuterium labeling in either chow or high-fat diet fed mice. Points expressed as log2 fold-change high-fat diet/chow on x-axis and - log10(p-value), obtained from 2-tailed t-test, on y-axis. (d) KEGG-pathway analysis for fractional synthesis rates of significant (p=<0.05 per 2-tailed t-test) proteins from high-fat diet/chow. n=at least 5 proteins per pathway. (e) Volcano plot of all proteins for which fractional synthesis rates were measured 96 hours after tunicamycin treatment in high-fat diet fed mice. Points expressed as log2 fold-change tunicamycin/control on x-axis and - log10(p-value), obtained from 2-tailed t-test, on y-axis. (f) KEGG-pathway analysis for fractional synthesis rates of significant (p=<0.05 per 2-tailed t-test) proteins from tunicamycin/control. n=at least 5 proteins per pathway. (g) Percent *de novo* lipogenesis of palmitate in tunicamycin compared to control treated high-fat diet fed mice in both triglycerides and phospholipids. n=6 mice per group. ns= no significance, * = <0.05, ** = <0.01, *** = <0.001.

2.3 Discussion

Metabolic responses to the initiation of the UPR^{ER} are not well understood[33]. We used metabolic labeling with stable isotopes to concurrently measure rates of fatty acid, cholesterol, and protein synthesis after inducing ER stress, with the goal of characterizing metabolic flux signatures over time and their relation to ultrastructural changes and gene expression patterns. Overall, proteome-wide protein synthesis rates declined with tunicamycin-induced ER stress, with the exception of chaperones and other key ER proteins recognized to be induced during the UPR^{ER}[34]. Protein synthesis rates generally matched the signatures measured through RNA-seq, which were similar to canonical UPR^{ER} signatures reported previously[35,36]. These data support the validity of using dynamic proteomics, as we have described previously[19,37], as a method to study tunicamycin-induced ER stress. This signature appears to be unique to the liver, as kidney tissues from the same tunicamycin treated mice failed to present a similar protein synthesis signature (figure 2.8). In other physiologic conditions, in contrast, clear dissociation between mRNA and protein synthesis rates has been observed[38–40]. Measurement of protein fluxes provides a potentially powerful tool for identifying UPR^{ER} regulators and signatures.

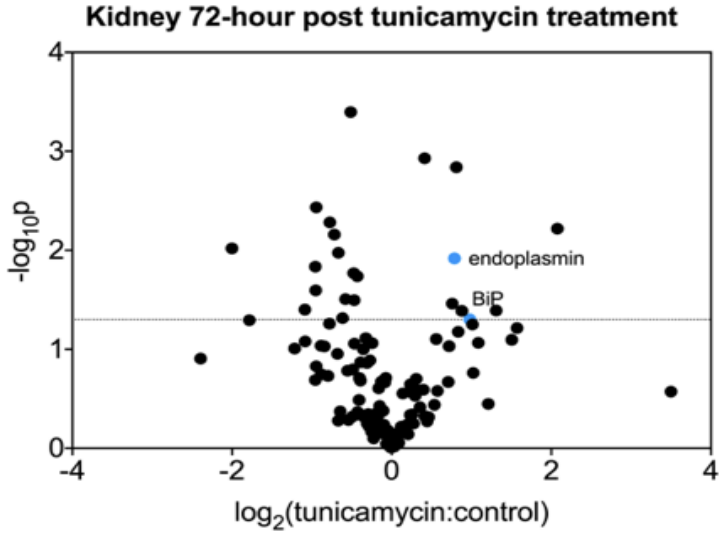

Figure 2.8. Ratio of tunicamycin:control treated mice kidneys. Volcano plot of all proteins for which fractional synthesis rates were measured 72 hrs post tunicamycin treatment. Points expressed as log2 fold-change tunicamycin treated/control on x-axis and - log10(p-value), obtained from 2-tailed t-test, on y-axis.

In particular, we found that synthesis rates of hepatic proteins involved in lipid metabolism and cholesterol synthesis were decreased in response to tunicamycin. In combination with similar reductions in gene expression for lipogenic proteins, this led us to investigate in depth *de novo* synthesis rates of lipids (palmitate in triglycerides and phospholipids) and cholesterol (free and esterified). These kinetic signatures somewhat surprisingly revealed significant decreases for both lipid and cholesterol synthesis rates over 72 hours under ER stress conditions.

These reductions in *de novo* lipid synthesis rates, gene expression, and protein synthesis rates for lipogenic enzymes were particularly striking in view of the well established changes in ER membrane structure and lipid stores during the UPR^{ER}[11]. Our ultrastructural observations confirmed that after 12 hours, ER membranes appeared strikingly different by electron microscopy. The ER appeared almost bubble-like, consistent with expansion believed to create space for chaperone refolding of accumulated misfolded proteins as part of the adaptation to restore protein homeostasis[14,41–43]. H&E staining also showed that lipids accumulated in the liver at 48 hours, the same time point at which *de novo* lipid synthesis rates were significantly decreased. These results in living mice differ from some studies in isolated cells[11,44,45], which have reported an increase in expression of genes involved in *de novo* synthesis during the UPR^{ER}. We then demonstrated directly that new lipids in the liver *in vivo* are mobilized from other tissues such as those in adipose stores. Interestingly, the biochemical form of this lipid import appears to be as free fatty acids, not transport of intact triglyceride or phospholipids in plasma lipoproteins, based on the replacement of pre-labeled glycerol moiety of hepatic triglycerides concurrent with increased palmitate import form adipose tissue. Tunicamycin-induced anorexia, as previously characterized by other groups[12], was observed in our studies. Mice treated with tunicamycin ate and weighed less than control mice, and presented with less adipose tissue upon dissection, supporting the observed mobilization of lipids from adipose to the liver. When we measured *de novo* lipogenesis of mice pair-fed to match the feeding patterns of tunicamycin-induced anorexia in mice, we observed similar decreased rates of lipid synthesis. However, calorie restricted mice are not known to accumulate lipid in their liver[46], as seen in our tunicamycin-treated mice, indicating that these results of lipid mobilization to the liver are independent from diet (figure 2.9).

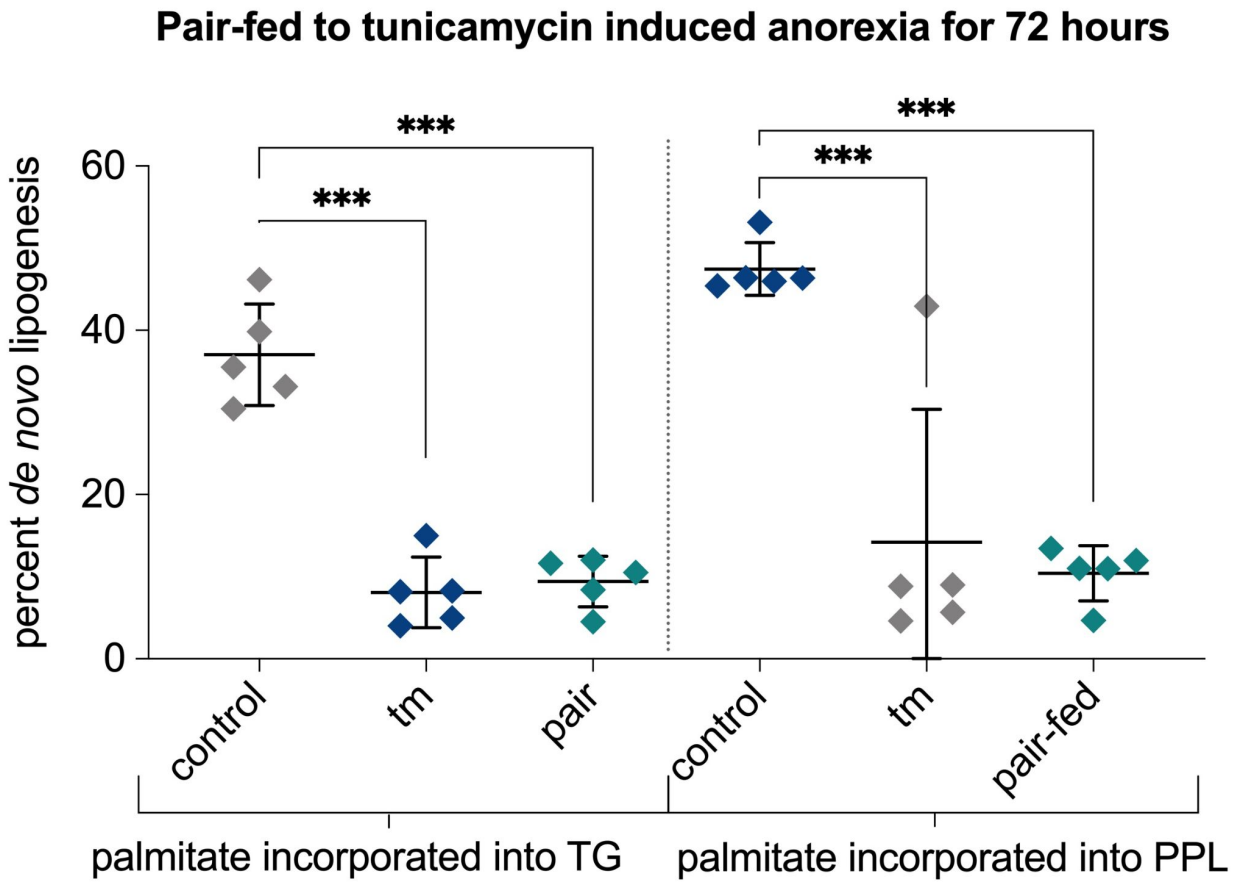

Figure 2.9. Percent *de novo* palmitate synthesis and incorporation into triglycerides and phospholipids in mice pair-fed to the amount eaten by mice experiencing tunicamycin induced anorexia. n=5 mice per group. ns= no significance, * = <0.05, ** = <0.01, *** = <0.001.

To evaluate these findings in a model more physiologically relevant to metabolic diseases, we also used a high-fat diet to induce ER stress through lipotoxicity and applied the same kinetic metrics to develop a metabolic flux signature[47]. Under a high-fat diet alone, most protein synthesis rates increased rather than decreased, including significant increases in canonical UPR^{ER} with similar increases to our findings with tunicamycin-induced ER stress. Lipid bilayer stress is thought to act though IRE1α sensors, initiating downstream effects of this arm of the UPR^{ER}[,48]. Because inhibition of translation occurs downstream of the PERK arm of the UPR^{ER}, it is reasonable to conclude that we did not see the same signature of proteome-wide suppression of protein synthesis in this lipotoxicity ER stress model as compared to the proteotoxicity model induced by tunicamycin. Other groups have also reported that a short term high-fat diet increases rather than decreases rates of protein translation[49,50]. We also saw decreased *de novo* lipogenesis rates under high-fat diet induced ER stress, which were exaggerated by the addition of tunicamycin induced ER stress. Tunicamycin also counteracted the widespread increases in protein synthesis rates induced by high-fat diet alone. We believe that this model demonstrates that livers under stress induced by high amounts of exogenous lipids exhibit a mixed handling of ER stress, which may not be as protective as with proteostatic stress alone and may be less able to restore normal homeostasis. This may further exacerbate a disease phenotype such as non-alcoholic fatty liver disease.

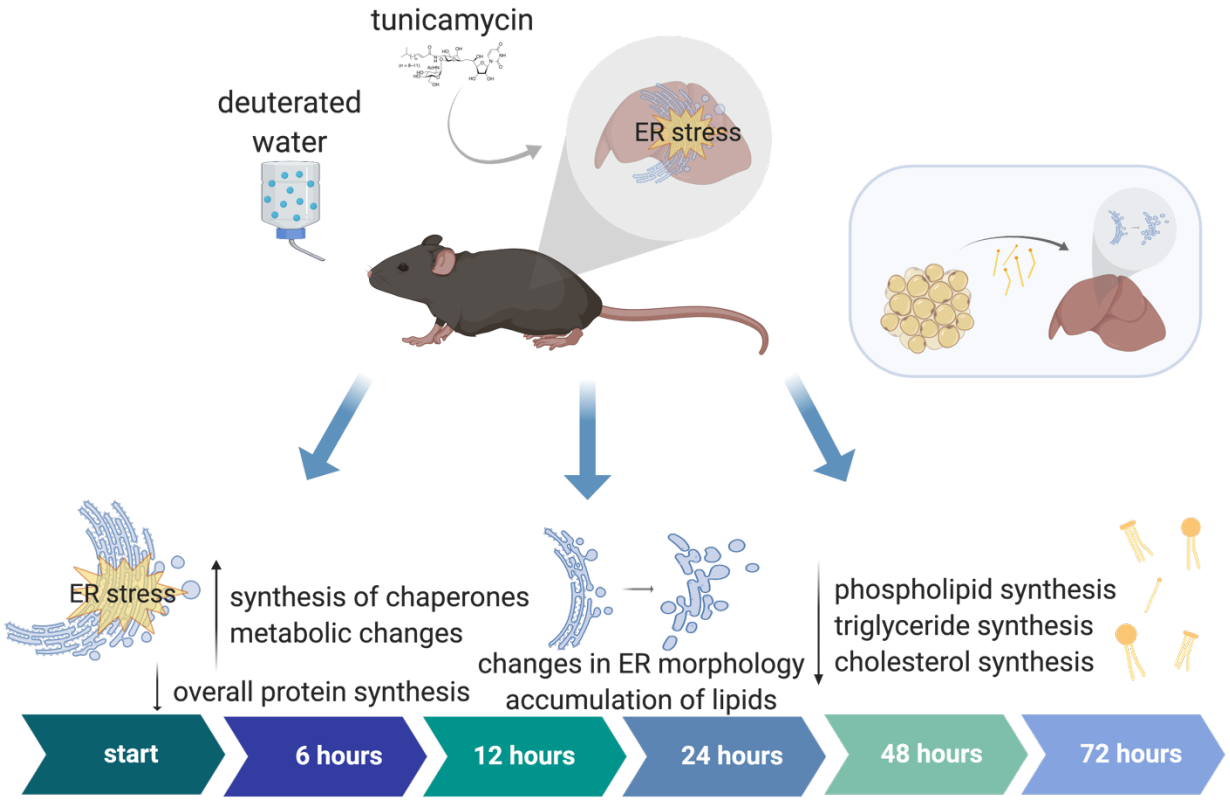

Figure 2.10. Summary figure shows metabolic flux signatures post tunicamycin induced ER stress in mouse liver. Overall protein synthesis declines with the exception of chaperones and UPRER related proteins. Proteins involved in lipogenesis are significantly decreased in their synthesis rates. At 12 hours post tunicamycin, ER stress induced changes in ER morphology in hepatocytes are evident, followed by lipid accumulation at 48 hours. At 48 hours post ER stress induction, palmitate incorporated into both phospholipids and triglycerides decline, as well as cholesterol synthesis. Lipids appear to be mobilized from the adipose tissue and deposited in the liver.

In summary, these data extend the metabolic alterations invoked during the UPR^{ER} and their importance in metabolic homeostasis (figure 2.10). The source of accumulated lipid droplets and ER lipids during ER stress in the liver *in vivo* is from lipids taken up from outside the liver not synthesized *de novo* locally. Under ER stress conditions, key metabolic pathways including lipid and cholesterol synthesis are reduced while other pathways are perturbed in complex and not entirely predictable ways, including mobilization of lipids from adipose tissue to the liver. Prolonged disruption of these pathways may lead to progression of diseases involving altered lipid and protein homeostasis such as non-alcoholic fatty liver disease. This finding is useful as a differential pathogenic signature of ER stress in contrast to insulin-induced lipid accumulation in the liver, for example, where *de novo* lipogenesis is highly elevated[51]. These findings support that the UPR^{ER} may have implications for metabolic diseases characterized by accumulation of lipids.

Table 2.1. Individual protein synthesis rate ratios of tunicamycin/control mice. Ratio of above 1 indicates a higher synthesis rate under ER stress. Ratio of below 1 indicates a lower synthesis rate under ER stress.

Protein	6 hr ratio	12 hr ratio	24 hr ratio	48 hr ratio	72 hr ratio
10 kDa heat shock protein, mitochondrial	0.63	0.79	1.41	1.03	1.10

14-3-3 protein beta/alpha	1.00	0.55	1.09	0.96	1.01
14-3-3 protein epsilon	1.47	0.27	0.21	0.63	0.76
14-3-3 protein gamma	3.82	0.56	1.05	1.01	1.08
14-3-3 protein zeta/delta	1.25	0.81	1.32	1.16	1.29
2-aminomuconic semialdehyde dehydrogenase	0.91	1.02	0.32	0.79	0.92
2-hydroxyacyl-CoA lyase 1	1.16	0.81	1.12	1.11	0.97
2-iminobutanoate/2-iminopropanoate deaminase	0.72	0.58	0.58	0.59	0.88
2,4-dienoyl-CoA reductase, mitochondrial	1.20	0.38	0.36	0.95	1.03
3-hydroxyanthranilate 3,4-dioxygenase	0.62	0.56	0.33	0.75	0.55
3-hydroxyisobutyrate dehydrogenase, mitochondrial	1.00	0.80	1.08	1.30	1.08
3-ketoacyl-CoA thiolase A, peroxisomal	0.53	0.52	0.77	0.86	0.98
3-ketoacyl-CoA thiolase B, peroxisomal	0.61	0.34	0.69	0.68	0.94
3-ketoacyl-CoA thiolase, mitochondrial	0.81	1.55	0.69	0.57	0.81
4-aminobutyrate aminotransferase, mitochondrial	1.62	0.54	1.51	0.66	
4-hydroxyphenylpyruvate dioxygenase	0.58	0.72	0.84	0.89	0.87
4-trimethylaminobutyraldehyde dehydrogenase	0.42	0.52	1.26	0.79	0.83
40S ribosomal protein S17	0.73	0.73	0.63	1.48	0.68
40S ribosomal protein S2			0.66	1.48	1.11
40S ribosomal protein S20		0.35	0.59	1.47	
40S ribosomal protein S28	0.35	1.08	1.46	1.25	1.63
40S ribosomal protein S3			1.10		
40S ribosomal protein S3a	1.23	1.29	0.87	1.10	1.25
40S ribosomal protein S4, X isoform			3.49		
40S ribosomal protein S7	0.51	0.96	1.18	1.27	1.24
40S ribosomal protein S8	0.73	4.60	1.09	1.15	1.29
40S ribosomal protein SA			1.18	1.06	1.52
6-phosphogluconate dehydrogenase, decarboxylating	0.96	1.56	0.94	0.82	0.88
6-phosphogluconolactonase	0.54	0.34	1.11	0.88	1.01
60 kDa heat shock protein, mitochondrial	0.60	1.36	0.95	1.00	1.24

60S acidic ribosomal protein P0	0.31			2.01	
60S ribosomal protein L12		0.24	1.38	2.00	1.54
60S ribosomal protein L23a	0.70			1.19	
60S ribosomal protein L27a			0.07	0.28	
60S ribosomal protein L4			3.62		
60S ribosomal protein L5	1.21		0.30		
60S ribosomal protein L6	0.72	0.82	1.09	1.29	1.30
Acetyl-CoA acetyltransferase, cytosolic	1.19	0.27	0.51	0.62	0.78
Acetyl-CoA acetyltransferase, mitochondrial	0.43	0.43	0.91	0.52	1.47
Aconitate hydratase, mitochondrial	1.12	1.21	1.62	0.86	0.79
Actin, alpha cardiac muscle 1	1.51	3.96	0.98	1.07	1.04
Actin, aortic smooth muscle	0.92	0.91	0.59	0.92	1.17
Actin, cytoplasmic 1	0.69	2.99	0.92	0.99	1.04
Acyl-CoA synthetase family member 2, mitochondrial	1.37	2.07	1.31	0.66	1.10
Acyl-CoA-binding protein	0.75	0.41	0.54	0.59	0.73
Acyl-coenzyme A synthetase ACSM1, mitochondrial	0.72	1.38	0.70	1.01	0.82
Adenosine kinase	0.67	0.74	0.91	1.00	1.21
Adenosylhomocysteinase	0.53	1.92	0.94	0.98	1.06
Adenylate kinase 2, mitochondrial	0.95	0.61	0.82	0.74	0.65
ADP/ATP translocase 2	0.98	0.93	0.76	0.76	0.93
Alanine aminotransferase 1	0.60	0.95	1.21	1.03	0.84
Alcohol dehydrogenase 1	0.61	0.68	0.49	0.33	0.52
Alcohol dehydrogenase class-3	0.98	0.94	1.02	0.65	0.90
Aldehyde dehydrogenase family 3 member A2	0.74	0.55	0.89	0.89	0.79
Aldehyde dehydrogenase, cytosolic 1	0.74	1.37	0.62	0.67	0.62
Aldehyde dehydrogenase, mitochondrial	0.54	0.79	0.80	0.72	0.86
Aldehyde oxidase 3	0.92	0.93	0.55	0.72	0.61
Aldo-keto reductase family 1 member A1	1.33	1.19	1.31	0.75	0.98
Aldo-keto reductase family 1 member C13	0.83	6.33	0.59	0.53	
Alpha-aminoadipic semialdehyde dehydrogenase	0.87	0.64	0.65	0.63	0.69

Alpha-aminoadipic semialdehyde synthase, mitochondrial	0.80	0.91	1.15	0.93	1.19
Alpha-enolase	0.65	1.09	0.59	0.67	0.81
Annexin A5	0.92			1.17	
Arginase-1	0.55	1.44	0.53	0.88	1.02
Argininosuccinate lyase	1.08	1.93	0.57	0.60	0.79
Argininosuccinate synthase	0.56	0.60	0.89	1.18	1.12
Aspartate aminotransferase, cytoplasmic	1.03	2.95	1.64	1.70	1.72
Aspartate aminotransferase, mitochondrial	0.74	1.94	0.93	0.85	1.07
ATP synthase F(0) complex subunit B1, mitochondrial			0.37	0.47	0.95
ATP synthase subunit alpha, mitochondrial	0.72	0.59	0.84	0.81	0.89
ATP synthase subunit beta, mitochondrial	0.59	2.33	0.53	0.78	1.01
ATP synthase subunit d, mitochondrial	0.63	0.45	0.76	0.78	0.90
ATP synthase subunit delta, mitochondrial	0.87	1.00	0.60	1.44	0.89
ATP synthase subunit O, mitochondrial	2.12	1.02	0.61	0.71	1.01
ATP-citrate synthase	0.83			0.54	
Beta-actin-like protein 2	0.80	2.73	0.91	0.92	1.03
Betaine--homocysteine S-methyltransferase 1	0.60	1.47	0.71	1.24	0.94
Bifunctional epoxide hydrolase 2	0.70	0.80	1.15	0.89	0.98
Bile acyl-CoA synthetase	5.48	0.24	0.40	0.96	1.00
C-1-tetrahydrofolate synthase, cytoplasmic	1.24	1.24	0.57	0.49	1.11
Calcium-binding mitochondrial carrier protein Aralar2	1.25	2.21	0.88	0.66	1.04
Calreticulin	1.45	2.36	2.38	1.96	1.63
Carbamoyl-phosphate synthase [ammonia], mitochondrial	0.63	1.08	0.57	0.66	0.74
Carbonic anhydrase 3	0.76	0.68	0.29	0.24	0.36
Carboxylesterase 1D	0.48	0.58	0.29	0.26	0.40
Carboxylesterase 1F	0.66	0.32	0.39	0.36	0.43
Carboxylesterase 3A	0.58	0.59	0.62	0.45	0.56

Carboxylesterase 3B	0.63	0.66	0.63	0.54	0.54
Catalase	0.59	1.23	0.65	0.86	0.94
Catechol O-methyltransferase	0.70	1.31	0.49	0.80	
Clathrin heavy chain 1	1.49	0.65	2.30	1.53	1.11
Cystathionine gamma-lyase	0.87	0.94	1.06	1.43	1.28
Cysteine sulfinic acid decarboxylase	0.75	0.66	0.37	0.35	0.46
Cytochrome b-c1 complex subunit 1, mitochondrial	0.95	0.70	0.97	0.70	0.87
Cytochrome b-c1 complex subunit 2, mitochondrial			0.44		
Cytochrome b-c1 complex subunit 6, mitochondrial	0.44	0.65	0.54	0.71	0.77
Cytochrome b5	0.79	1.59	0.91	0.95	1.10
Cytochrome c oxidase subunit 2	0.55	1.31	0.95	0.84	1.04
Cytochrome c oxidase subunit 4 isoform 1, mitochondrial	0.80			0.96	
Cytochrome c1, heme protein, mitochondrial	0.65	1.90		1.39	0.86
Cytochrome P450 1A2	0.50	0.69	0.95		
Cytochrome P450 2A12	1.01		1.43		1.23
Cytochrome P450 2C29	0.51	0.57	0.47	0.42	0.73
Cytochrome P450 2D10	0.65	0.74	0.89	0.79	1.24
Cytochrome P450 2D26	0.75	0.53	1.21	1.04	1.24
Cytochrome P450 2D9	0.75	0.85	0.94	0.76	1.21
Cytochrome P450 2E1	0.73	0.91	0.97	1.04	0.99
Cytochrome P450 2F2	0.57	0.59	0.69	0.51	0.76
Cytochrome P450 3A11	0.70	0.80	0.83	0.92	1.02
Cytoplasmic aconitate hydratase	0.78	0.72	0.46	0.57	1.00
Cytosol aminopeptidase	1.04	0.71	0.87	0.95	1.23
Cytosolic 10-formyltetrahydrofolate dehydrogenase	0.45	1.11	0.55	0.74	0.89
D-beta-hydroxybutyrate dehydrogenase, mitochondrial	0.61	0.43	0.67	0.60	0.95
D-dopachrome decarboxylase	0.81	1.72	1.11	1.17	1.00
Delta-1-pyrroline-5-carboxylate dehydrogenase, mitochondrial	0.94	2.14	0.68	0.71	0.91

Dihydrolipoyl dehydrogenase, mitochondrial	1.28	0.65	1.42	0.61	1.22
Dihydropteridine reductase	1.73	0.48	0.79	0.82	
Dihydropyrimidinase	0.50	0.52	0.47	0.40	
Dimethylaniline monooxygenase [N-oxide-forming] 5	0.77	0.83	0.73	0.72	0.83
Dimethylglycine dehydrogenase, mitochondrial	2.95	0.69	0.74	0.78	0.72
Electron transfer flavoprotein subunit alpha, mitochondrial	1.16	0.80	0.74	0.75	0.82
Electron transfer flavoprotein subunit beta	0.79	0.86	1.03	0.70	0.85
Electron transfer flavoprotein-ubiquinone oxidoreductase, mitochondrial				0.82	
Elongation factor 1-alpha 1	0.55	0.68	0.90	0.88	1.26
Elongation factor 1-alpha 2	0.75		1.24	0.85	1.73
Elongation factor 1-beta	1.09	1.00	1.99	0.94	
Elongation factor 1-delta	0.96	1.25	1.16	1.54	1.42
Elongation factor 1-gamma	4.50	0.87	1.23	1.46	1.33
Elongation factor 2	0.53	0.60	0.89	0.84	1.08
Endoplasmic reticulum chaperone BiP	4.00	3.10	2.70	1.93	1.75
Endoplasmin	2.73	3.13	2.89	1.86	1.60
Enoyl-CoA delta isomerase 1, mitochondrial	0.26	0.95	1.21	0.84	0.92
Enoyl-CoA hydratase, mitochondrial	1.85		2.30	0.25	0.72
Epoxide hydrolase 1	0.81	0.70	0.69	0.69	0.80
Estradiol 17 beta-dehydrogenase 5	0.44	1.68	0.49	0.30	0.54
Farnesyl pyrophosphate synthase	0.80	1.50	1.18	1.49	1.12
Fatty acid synthase	0.52	0.57	0.42	0.37	0.71
Fatty acid-binding protein, liver	0.58	0.89	0.28	0.33	0.52
Ferritin light chain 1	0.63	1.10	1.15	1.13	1.04
Fibrinogen gamma chain	1.09		2.26	2.53	1.93
Flavin reductase (NADPH)	1.39	0.14	0.98	0.50	0.96
Formimidoyltransferase-cyclodeaminase	0.80	1.27	1.05	0.98	1.03
Fructose-1,6-bisphosphatase 1	0.81	0.67	1.11	1.45	1.32
Fructose-bisphosphate aldolase B	0.69	0.84	1.05	1.08	1.02

Fumarate hydratase, mitochondrial	0.58	1.00	1.20	0.87	1.30
Fumarylacetoacetase	0.75	0.70	0.75	0.88	1.00
Glucose-6-phosphate isomerase			1.39	0.45	0.68
Glutamate dehydrogenase 1, mitochondrial	0.57	0.84	0.44	0.43	0.56
Glutamine synthetase	0.82	1.33	0.64	0.37	0.28
Glutaryl-CoA dehydrogenase, mitochondrial	0.98	0.50	0.95	1.69	1.09
Glutathione peroxidase 1	0.92	0.61	0.44	0.61	0.62
Glutathione S-transferase A1				0.25	0.68
Glutathione S-transferase A3	0.46	1.40	0.51	0.45	0.59
Glutathione S-transferase A4	0.50	0.52	0.62	0.29	0.44
Glutathione S-transferase Mu 1	0.69	3.79	1.23	0.96	0.95
Glutathione S-transferase Mu 2	0.13	0.58	1.35	0.97	0.99
Glutathione S-transferase Mu 3	0.51	3.66	1.31	0.99	1.06
Glutathione S-transferase P 1	0.74	2.34	0.72	0.40	0.49
Glutathione S-transferase P 2	0.68	1.85	0.61	0.38	0.59
Glyceraldehyde-3-phosphate dehydrogenase	0.54	0.59	1.19	0.87	1.11
Glycerol-3-phosphate dehydrogenase [NAD(	0.26				
Glycine N-acyltransferase	1.73	1.81	1.11	0.76	0.97
Glycine N-methyltransferase	0.66	1.33	0.94	1.15	1.23
Glycogen phosphorylase, liver form	0.87	0.60	0.70	0.42	0.62
Glyoxylate reductase/hydroxypyruvate reductase	0.58	0.50	0.73	0.94	0.95
GTP:AMP phosphotransferase AK3, mitochondrial			0.24	0.23	1.82
Heat shock 70 kDa protein 1-like		0.90	1.25	0.88	1.74
Heat shock cognate 71 kDa protein	0.93	0.58	0.92	1.07	1.01
Heat shock protein HSP 90-alpha	0.73	0.31	0.72	0.81	0.95
Heat shock protein HSP 90-beta	0.70	0.61	0.77	0.97	0.93
Hemoglobin subunit alpha	1.36	1.37	1.14	1.41	0.44
Hemoglobin subunit beta-1	0.78	4.18	1.36	0.47	0.53
Hemoglobin subunit beta-2	0.36	1.25	1.73	0.21	0.42
Histidine ammonia-lyase	0.61	0.71	0.52	0.67	0.93

Histidine triad nucleotide-binding protein 1	0.92	1.08	1.17	1.20	1.26
Homogentisate 1,2-dioxygenase	0.84	0.60	0.50	0.69	0.82
Hydroxyacyl-coenzyme A dehydrogenase, mitochondrial	1.33	0.85	0.46	0.62	0.56
Hydroxymethylglutaryl-CoA lyase, mitochondrial	0.63	2.54	1.01	0.78	1.12
Hydroxymethylglutaryl-CoA synthase, mitochondrial	0.60	2.19	0.80	0.86	1.12
Hypoxia up-regulated protein 1	0.51	1.49	2.93	2.04	1.73
Indolethylamine N-methyltransferase	1.99	0.62	0.38	0.30	0.41
Interleukin-12 receptor subunit beta-2	0.97	0.81	0.74	0.57	0.90
Isochorismatase domain-containing protein 2A	0.52	1.27	1.09	1.64	1.38
Isocitrate dehydrogenase [NADP] cytoplasmic	1.62	0.91	0.77	0.65	0.90
Isovaleryl-CoA dehydrogenase, mitochondrial	0.42		0.56	1.00	0.95
L-lactate dehydrogenase A chain	0.81	0.40	0.44	0.74	1.40
Lactoylglutathione lyase	0.44	0.57	0.55	0.47	0.80
Lipoamide acyltransferase component of branched-chain alpha-keto acid dehydrogenase complex, mitochondrial		0.36	0.82	1.09	1.52
Liver carboxylesterase 1	0.32	0.86	0.58	0.26	0.44
Lon protease homolog, mitochondrial				4.83	
Long-chain-fatty-acid--CoA ligase 1	0.77	0.84	0.35	0.48	0.67
Lysine-specific demethylase 5A	0.92				
Macrophage migration inhibitory factor	0.25	0.30	1.56	1.23	1.22
Major urinary protein 1	0.81	0.96	0.79	0.91	0.86
Major urinary protein 11	0.79	0.96	0.97	0.87	0.99
Major urinary protein 17	0.80	0.95	1.01	0.94	0.84
Major urinary protein 18	0.82	0.96	0.76	0.97	0.83
Major urinary protein 2	0.84	0.95	0.79	0.92	0.93
Malate dehydrogenase, cytoplasmic	0.99	1.99	1.14	1.27	1.10
Malate dehydrogenase, mitochondrial	0.85	0.45	1.57	1.43	1.38
Maleylacetoacetate isomerase	0.60	0.91	0.89	0.99	1.00
Mediator of RNA polymerase II			0.42	0.21	

transcription subunit 23					
Medium-chain specific acyl-CoA dehydrogenase, mitochondrial	0.48	0.61	0.94	0.87	1.02
Membrane-associated progesterone receptor component 1	0.79	0.37	1.17	0.53	1.22
Methanethiol oxidase	0.73	0.62	0.37	0.40	0.44
Methylmalonate-semialdehyde dehydrogenase [acylating], mitochondrial	1.17	0.89	0.86	0.94	1.20
Methyltransferase-like protein 7B			2.30	1.52	1.32
Microsomal glutathione S-transferase 1	1.07	0.60	0.53	0.42	
Microsomal triglyceride transfer protein large subunit	2.54		0.95		
Microtubule-associated protein 2		0.90	1.03	1.35	1.25
Multiple epidermal growth factor-like domains protein 8	1.38	0.74	0.96	0.45	0.73
NAD-dependent protein deacetylase sirtuin-3		1.28	0.44	0.59	
NADH dehydrogenase [ubiquinone] 1 alpha subcomplex subunit 9, mitochondrial			0.79	0.87	
NADH-cytochrome b5 reductase 3	1.03	0.09	0.51	0.50	0.75
NADH-ubiquinone oxidoreductase 75 kDa subunit, mitochondrial	0.85			0.89	
NADPH--cytochrome P450 reductase	0.88	1.20	0.68	0.64	
Nesprin-1				0.45	
Nicotinate-nucleotide pyrophosphorylase [carboxylating]	0.85	0.25	0.73		0.89
Non-specific lipid-transfer protein	0.59	0.56	0.60	0.57	0.81
Nucleoside diphosphate kinase A	0.73			1.23	
Nucleoside diphosphate kinase B	0.74	0.56	1.86	1.43	1.34
Ornithine aminotransferase, mitochondrial	0.59	0.67	0.87	0.94	1.06
Ornithine carbamoyltransferase, mitochondrial	1.16	2.37	0.36	0.35	0.53
Peptidyl-prolyl cis-trans isomerase A	0.83	0.39	1.02	0.77	0.95
Peptidyl-prolyl cis-trans isomerase B			1.45	1.55	1.22
Peroxiredoxin-1	0.69	0.51	0.59	0.76	1.01
Peroxiredoxin-2	0.46	0.17	0.78	0.68	1.33

Peroxiredoxin-5, mitochondrial	1.12	1.98	0.73	0.73	0.81
Peroxiredoxin-6	0.86	0.78	0.72	0.67	0.81
Peroxisomal acyl-coenzyme A oxidase 1	0.62	0.71	0.86	1.13	1.29
Peroxisomal bifunctional enzyme	1.06	0.80	0.66	1.10	1.13
Peroxisomal multifunctional enzyme type 2	1.10	0.51	1.16	1.35	1.59
Phenazine biosynthesis-like domain-containing protein 1	0.69	0.84	0.77	0.62	0.63
Phenazine biosynthesis-like domain-containing protein 2	0.70	0.81	0.62	0.71	0.69
Phenylalanine-4-hydroxylase	0.56	0.72	0.99	0.88	1.09
Phosphoglucomutase-1	0.80	0.47	0.81	0.82	1.06
Phosphoglycerate kinase 1	0.81	0.86	1.27	1.18	1.26
Phosphoglycerate mutase 1	0.84	0.49	1.27	0.72	0.91
Polyubiquitin-B	0.74	1.07	1.06	1.10	1.22
Pregnancy zone protein	0.63			1.23	
Probable helicase senataxin	0.44	0.44		0.38	0.63
Probable imidazolonepropionase				1.21	
Profilin-1	0.65	1.65			
Prohibitin	0.55	0.54	1.80	0.93	0.84
Protein ABHD14B		0.70	0.82		0.85
Protein disulfide-isomerase	0.92	1.36	2.10	1.68	1.52
Protein disulfide-isomerase A3	1.18	2.20	2.33	1.62	1.51
Protein disulfide-isomerase A4	2.26	1.88	2.14	2.11	1.89
Protein disulfide-isomerase A6	1.49	1.68	1.92	2.21	1.55
Protein NDRG2	0.94			0.92	
Protein PRRC2A					
Protein/nucleic acid deglycase DJ-1	1.92		1.10		0.95
Pyrethroid hydrolase Ces2a	0.57	0.59	0.63	0.42	0.76
Pyruvate carboxylase, mitochondrial	0.72	0.79	0.83	0.82	1.07
Pyruvate kinase PKLR	0.54	2.33	1.09	0.40	
Rab GDP dissociation inhibitor beta	1.27	0.93	1.06		
Radixin				1.07	
Ras-related protein Rab-1A	0.94			1.09	
Regucalcin	0.88	2.28	0.61	0.33	0.46

Retinal dehydrogenase 1	0.53	1.46	0.56	0.67	0.77
Rho GDP-dissociation inhibitor 1	0.47	2.28	0.78	0.75	0.90
S-adenosylmethionine synthase isoform type-1	0.65	0.71	1.34	1.18	1.21
S-formylglutathione hydrolase	0.97	0.71	0.99	1.02	1.14
Sarcosine dehydrogenase, mitochondrial	0.81	0.81	0.92	1.02	1.17
SEC14-like protein 2	0.84	0.77	1.04	0.74	0.90
Selenium-binding protein 2	0.61	0.79	0.41	0.39	0.41
Sepiapterin reductase			1.35	1.00	1.28
Serine protease inhibitor A3K	0.34	0.37	0.46	0.50	0.38
Serine protease inhibitor A3M	0.32	0.33	0.25	0.45	0.05
Serotransferrin	0.35	0.28	0.45		0.85
Serum albumin	0.34	1.87	0.51	0.39	0.67
Short-chain specific acyl-CoA dehydrogenase, mitochondrial	1.00	0.68	1.27	0.67	0.70
Sorbitol dehydrogenase	0.71	0.68	0.60	0.65	0.85
Staphylococcal nuclease domain-containing protein 1	0.47	0.21	1.92	2.10	1.22
START domain-containing protein 10	1.32	0.29	0.66	0.77	
Stress-70 protein, mitochondrial	0.84	1.13	1.92	1.22	1.21
Succinate dehydrogenase [ubiquinone] flavoprotein subunit, mitochondrial	0.74	0.55	0.68	0.88	0.93
Succinate--CoA ligase [GDP-forming] subunit beta, mitochondrial	1.12	0.78	0.97	0.94	0.93
Succinate-semialdehyde dehydrogenase, mitochondrial	1.29	0.53	0.38	0.60	0.88
Superoxide dismutase [Cu-Zn]	0.80	2.34	0.52	0.71	0.87
Superoxide dismutase [Mn], mitochondrial	1.60		0.98	0.58	0.81
T-complex protein 1 subunit gamma	1.02	2.47	1.00	0.97	0.80
T-complex protein 1 subunit zeta	0.92	0.54	1.02	0.99	0.96
Thioredoxin domain-containing protein 12	0.45	0.32	0.35	0.53	0.58
Thiosulfate sulfurtransferase	0.64	0.85	0.82	0.74	0.85
Trans-1,2-dihydrobenzene-1,2-diol dehydrogenase		0.66	0.78	0.69	1.04
Transitional endoplasmic reticulum	1.08	1.95	1.59	0.95	1.29

ATPase					
Transketolase	0.89	1.34	0.68	0.60	0.55
Trifunctional enzyme subunit alpha, mitochondrial	0.97	2.78	0.66	0.85	0.96
Trifunctional enzyme subunit beta, mitochondrial	0.62	0.90	0.73	0.92	0.96
Triokinase/FMN cyclase	0.75	0.98	0.70	0.65	0.82
Triosephosphate isomerase	0.76	0.83	0.60	0.78	0.78
Tripeptidyl-peptidase 1	5.36			0.14	
Tubulin alpha-1A chain		0.96	1.17	0.80	0.86
Tubulin alpha-1B chain	1.09	0.84	1.09	0.73	0.66
Tubulin alpha-1C chain	1.03	0.72	0.92	0.69	0.71
Tubulin alpha-4A chain	0.75	1.48	0.93	0.69	0.61
Tubulin alpha-8 chain	0.60	1.07	0.65		0.61
Tubulin beta-2A chain	0.85	1.30	1.38	1.23	1.09
Tubulin beta-2B chain					1.36
Tubulin beta-4A chain		1.28	2.31	1.19	1.22
Tubulin beta-4B chain	1.11	1.45	1.49	1.38	1.42
Tubulin beta-5 chain	2.20	1.48	1.63	1.18	1.68
Ubiquitin-40S ribosomal protein S27a	0.53	0.63	1.25	0.49	1.10
Ubiquitin-like modifier-activating enzyme 1	0.78	1.16	1.01	1.11	1.22
UDP-glucose 6-dehydrogenase	1.52	0.72	0.48	0.54	0.87
UDP-glucuronosyltransferase 1-1	0.69	0.82	0.78	1.14	1.30
UDP-glucuronosyltransferase 1-6		0.30	0.92		1.37
UDP-glucuronosyltransferase 1-9	0.55	1.21	1.15	1.10	1.29
UDP-glucuronosyltransferase 2B17	0.58	0.80	0.63	0.94	1.02
Uricase	0.59	0.60	0.88	0.96	
Urocanate hydratase	0.59	0.58	0.37	0.52	0.40
UTP--glucose-1-phosphate uridylyltransferase	0.74	0.91	1.22	1.05	1.07
Valacyclovir hydrolase	0.67	0.60	0.48	0.56	0.72
Very long-chain acyl-CoA synthetase	0.99	0.71	0.61	0.90	0.99
Very long-chain specific acyl-CoA dehydrogenase, mitochondrial	0.86	1.21	0.84	0.87	1.08

Vitamin D-binding protein	0.68	0.86	0.92	4.66	

Table 2.2. First row shows individual protein synthesis rate ratios of high-fat diet/control mice. Ratio of above 1 indicates a higher synthesis rate under a high-fat diet. Ratio of below 1 indicates a lower synthesis rate with under high-fat diet. Second row shows individual protein synthesis rate ratios of tunicamycin/control high-fat diet fed mice. Ratio of above 1 indicates a higher synthesis rate under ER stress. Ratio of below 1 indicates a lower synthesis rate under ER stress.

Protein	Ratio HFD/chow	Ratio HFD TM/DMSO
10 kDa heat shock protein, mitochondrial	3.92	1.09
2-aminomuconic semialdehyde dehydrogenase		0.69
2-iminobutanoate/2-iminopropanoate deaminase	3.62	0.79
3-ketoacyl-CoA thiolase B, peroxisomal	2.05	1.16
3-ketoacyl-CoA thiolase, mitochondrial	3.83	0.80
40S ribosomal protein S17		1.08
40S ribosomal protein S26		0.92
40S ribosomal protein S3a		1.77
40S ribosomal protein S4, X isoform	7.70	1.03
40S ribosomal protein SA		0.88
60 kDa heat shock protein, mitochondrial	4.16	0.89
60S ribosomal protein L29	2.67	1.37
60S ribosomal protein L3		1.46
60S ribosomal protein L6	3.25	1.48
60S ribosomal protein L7		1.10
Actin, cytoplasmic 1		1.06
Adenosylhomocysteinase	3.36	0.86
ADP/ATP translocase 2		0.95
Alcohol dehydrogenase 1	3.44	0.37
Aldehyde dehydrogenase family 8 member A1	1.99	
Aldehyde dehydrogenase, mitochondrial	2.47	0.62
Alpha-2-HS-glycoprotein		1.09
Alpha-enolase	3.22	1.03
Arginase-1	3.05	1.08
Argininosuccinate lyase		0.69
Argininosuccinate synthase	3.45	1.08

Aspartate aminotransferase, mitochondrial	4.87	0.74
ATP synthase subunit alpha, mitochondrial	4.31	0.92
ATP synthase subunit beta, mitochondrial	3.30	0.97
ATP synthase subunit d, mitochondrial		0.60
Betaine--homocysteine S-methyltransferase 1	2.67	0.54
Bifunctional epoxide hydrolase 2	4.15	0.60
C4b-binding protein		1.07
Calreticulin	1.00	0.98
Carbamoyl-phosphate synthase [ammonia], mitochondrial	3.55	0.77
Carbonic anhydrase 3	4.45	0.19
Carboxylesterase 1D	3.71	0.45
Carboxylesterase 3A	2.59	0.51
Catalase	1.84	0.83
Cystathionine gamma-lyase	4.37	1.06
Cytochrome b-c1 complex subunit 1, mitochondrial		0.93
Cytochrome b5 type B		1.08
Cytochrome c oxidase subunit 5A, mitochondrial		0.82
Cytosol aminopeptidase		1.14
Cytosolic 10-formyltetrahydrofolate dehydrogenase	2.91	0.83
D-dopachrome decarboxylase	1.72	1.16
Delta-1-pyrroline-5-carboxylate dehydrogenase, mitochondrial	4.95	0.77
Double-stranded RNA-specific editase 1		0.82
Electron transfer flavoprotein subunit alpha, mitochondrial	3.46	0.59
Electron transfer flavoprotein subunit beta	2.87	0.75
Elongation factor 1-alpha 1	3.43	1.52
Elongation factor 1-gamma		1.16
Elongation factor 2	2.81	1.11
Endoplasmic reticulum chaperone BiP	3.56	1.41
Endoplasmin	3.57	1.42
Estradiol 17 beta-dehydrogenase 5	3.43	0.53

Fatty acid-binding protein, liver	4.16	0.61
Formimidoyltransferase-cyclodeaminase	2.64	0.85
Fructose-1,6-bisphosphatase 1	3.37	1.12
Fructose-bisphosphate aldolase B	3.26	0.72
Fumarylacetoacetase	3.02	0.99
Glutamate dehydrogenase 1, mitochondrial	3.51	0.57
Glutamine synthetase	3.38	0.78
Glutathione peroxidase 1	4.46	0.77
Glutathione S-transferase A3	3.75	0.65
Glutathione S-transferase Mu 1	5.82	0.95
Glutathione S-transferase Mu 2		0.87
Glutathione S-transferase P 1	3.93	0.83
Glyceraldehyde-3-phosphate dehydrogenase	1.91	1.40
Glycine N-methyltransferase	2.46	1.21
Glycogen phosphorylase, liver form	5.20	0.60
Glyoxylate reductase/hydroxypyruvate reductase	3.50	1.16
Heat shock cognate 71 kDa protein	2.66	0.87
Heat shock protein HSP 90-beta	2.51	0.67
Hemoglobin subunit alpha	4.31	0.53
Hemoglobin subunit beta-1	4.50	0.68
Hemoglobin subunit beta-2		0.77
Histidine triad nucleotide-binding protein 1		1.33
Homogentisate 1,2-dioxygenase	2.84	0.78
Hydroxyacyl-coenzyme A dehydrogenase, mitochondrial	1.56	0.96
Hydroxymethylglutaryl-CoA lyase, mitochondrial	2.21	1.21
Hydroxymethylglutaryl-CoA synthase, mitochondrial	3.13	0.94
Isocitrate dehydrogenase [NADP] cytoplasmic	3.86	0.97
L-lactate dehydrogenase A chain	2.90	1.09
LARGE xylosyl- and glucuronyltransferase 1		8.87
Malate dehydrogenase, cytoplasmic	3.83	0.99
Malate dehydrogenase, mitochondrial	4.64	0.99

Maleylacetoacetate isomerase	2.79	1.08
Methylmalonate-semialdehyde dehydrogenase [acylating], mitochondrial	2.41	2.14
Microsomal glutathione S-transferase 1	3.43	0.76
Non-specific lipid-transfer protein	2.36	0.64
Nucleoside diphosphate kinase B	2.17	0.87
Ornithine carbamoyltransferase, mitochondrial	4.24	0.99
Peptidyl-prolyl cis-trans isomerase A	2.50	0.89
Peptidyl-prolyl cis-trans isomerase B		1.59
Peroxiredoxin-1	3.02	0.97
Peroxiredoxin-5, mitochondrial		0.66
Peroxiredoxin-6	3.71	0.61
Peroxisomal acyl-coenzyme A oxidase 1	3.16	0.97
Prohibitin		0.87
Protein disulfide-isomerase	3.06	1.28
Protein disulfide-isomerase A3	2.89	1.40
Protein disulfide-isomerase A4	3.40	1.09
Protein disulfide-isomerase A6	3.92	2.89
Protein NipSnap homolog 1		1.73
Pyruvate carboxylase, mitochondrial	3.29	1.00
Pyruvate kinase PKLR		0.41
Regucalcin	3.51	0.71
Retinal dehydrogenase 1	3.47	1.39
S-adenosylmethionine synthase isoform type-1	1.94	0.72
Sarcosine dehydrogenase, mitochondrial	3.81	0.98
Selenium-binding protein 2	3.78	0.78
Serum albumin	3.80	0.60
Sorbitol dehydrogenase	4.58	0.46
Stress-70 protein, mitochondrial		1.02
Superoxide dismutase [Cu-Zn]	3.69	0.90
Trans-1,2-dihydrobenzene-1,2-diol dehydrogenase		2.64
Trifunctional enzyme subunit alpha, mitochondrial	5.79	0.73
Triokinase/FMN cyclase	3.76	0.88

Triosephosphate isomerase	5.60	1.08
Tubulin alpha-1B chain		0.96
Tubulin beta-4B chain	4.50	1.26
Tubulin beta-5 chain		1.27
Urocanate hydratase		0.88
Valacyclovir hydrolase	1.85	0.99

2.4 Materials and Methods

Animals

C57BL/6J male mice acquired from The Jackson Laboratory were used for this study. Mice were 12 weeks of age. All mice were housed according to the Animal Care and Use Committee (ACUC) standards in the animal facility at UC Berkeley. Mice were fed a standard chow diet and water ad libitum. Mice on a high-fat diet were fed a 60% high-fat diet (Research Diets, D12492) for 6 weeks.

Deuterated water labeling and tunicamycin treatment in mice

Mice were labeled with deuterated water (heavy water, ^2H_2O) beginning at time point 0 (t^0) through the end of the experiment. Proteins synthesized after t^0 will incorporate deuterium-labeled amino acids, thus enabling the measurement of proteins synthesized during the period of exposure to heavy water. Deuterium is rapidly incorporated throughout the body of an organism after treatment, bringing the deuterium enrichment in body water up to 5%. Deuterium enrichment is maintained through the intake of 8% ^2H_2O given as drinking water, thus making it an optimal labeling approach for *in vivo* experimental study. Mice are injected intraperitoneally (IP) with 100% ^2H_2O containing either tunicamycin dissolved in DMSO, or DMSO control. Mice were treated with 1.5 mg/kg tunicamycin dissolved in DMSO at t^0, or DMSO control, and tissues were harvested 6, 12, 24, 48, and 72 hours after the initial injection (n=5 mice per group).

Deuterated water labeling and tunicamycin treatment in mice: pre-label of adipose tissue triglycerides

Mice were labeled with deuterated water (heavy water, ^2H_2O) for 7 weeks to saturate tissues with deuterium *in vivo*. Deuterium is rapidly incorporated throughout the body of an organism after treatment, bringing the deuterium enrichment in body water up to 5%. Deuterium enrichment is maintained through the intake of 8% ^2H_2O given as drinking water, thus making it an optimal labeling approach for a long-term *in vivo* experimental study. Mice were then given non-labeling drinking water to wash deuterium label out of faster generating tissues (i.e. the liver), but not enough time to significantly reduce label in slower lipid turnover tissues such as the adipose. After 2 weeks, mice were injected intraperitoneally (IP) with either tunicamycin dissolved in DMSO, or DMSO control. Mice were treated with 1.5 mg/kg tunicamycin dissolved in DMSO, or DMSO control, and tissues were harvested 72 hours after the initial injection (n=4 mice per group).

Body water enrichment analysis

Mouse liver were distilled overnight upside down on a bead bath at 85°C to evaporate out body water. Deuterium present in the body water were exchanged onto acetone, and deuterium

enrichment in the body water was measured via gas chromatography mass spectrometry (GC-MS)[52].

Tissue preparation for liquid chromatography-mass spectrometry (LC-MS)
Tissues were flash frozen after harvest and homogenized in homogenization buffer (100 mM PMSF, 500 mM EDTA, EDTA-free Protease Inhibitor Cocktail (Roche, catalog number 11836170001), PBS) using a 5 mm stainless steel bead at 30 hertz for 45 seconds in a TissueLyser II (Qiagen). Samples were then centrifuged at 10,000 rcf for 10 minutes at 4°C. The supernatant was saved and protein was quantified using a Pierce BCA protein assay kit (ThermoFisher, catalog number 23225). 100 ug of protein was used per sample. 25 uL of 100 mM ammonium bicarbonate solution, 25 uL TFE, and 2.3 uL of 200 mM DTT were added to each sample and incubated at 60°C for 1 hour. 10 uL 200 mM iodoacetamide was then added to each sample and allowed to incubate at room temperature in the dark for 1 hour. 2 uL of 200 mM DTT was added and samples were incubated for 20 minutes in the dark. Each sample was then diluted with 300 uL H_2O and 100 uL 100 mM ammonium bicarbonate solution. Trypsin was added at a ratio of 1:50 trypsin to protein (trypsin from porcine pancreas, Sigma Aldrich, catalog number T6567). Samples were incubated at 37°C overnight. The next day, 2 uL of formic acid was added. Samples were centrifuged at 10,000 rcf for 10 minutes, collecting the supernatant. Supernatant was speedvac'd until dry and re-suspended in 50 uL of 0.1 % formic acid/3% acetonitrile/96.9% LC-MS grade water and transferred to LC-MS vials to be analyzed via LC-MS.

Liquid chromatography-mass spectrometry (LC-MS) analysis
Trypsin-digested peptides were analyzed on a 6550 quadropole time of flight (Q-ToF) mass spectrometer equipped with Chip Cube nano ESI source (Agilent Technologies). High performance liquid chromatography (HPLC) separated the peptides using capillary and nano binary flow. Mobile phases were 95% acetonitrile/0.1% formic acid in LC-MS grade water. Peptides were eluted at 350 nl/minute flow rate with an 18 minute LC gradient. Each sample was analyzed once for protein/peptide identification in data-dependent MS/MS mode and once for peptide isotope analysis in MS mode. Acquired MS/MS spectra were extracted and searched using Spectrum Mill Proteomics Workbench software (Agilent Technologies) and a mouse protein database (www.uniprot.org). Search results were validated with a global false discovery rate of 1%. A filtered list of peptides was collapsed into a nonredundant peptide formula database containing peptide elemental composition, mass, and retention time. This was used to extract mass isotope abundances (M0-M3) of each peptide from MS-only acquisition files with Mass Hunter Qualitative Analysis software (Agilent Technologies). Mass isotopomer distribution analysis (MIDA) was used to calculate peptide elemental composition and curve-fit parameters for predicting peptide isotope enrichment based on precursor body water enrichment (p) and the number (n) of amino acid C-H positions per peptide actively incorporating hydrogen (H) and deuterium (D) from body water. Subsequent data handling was performed using python-based scripts, with input of precursor body water enrichment for each subject, to yield fractional synthesis rate (FSR) data at the protein level. FSR data were filtered to exclude protein measurements with fewer than 2 peptide isotope measurements per protein. Details of FSR calculations and data filtering criteria have been described in detail previously (Holmes et al., 2015).

Calculation of fractional replacement (f) and replacement rate constant (k) for individual proteins

Details of f calculations were previously described[19].

Statistical analysis
Data were analyzed using GraphPad Prism software (version 8.0).

KEGG pathway analysis
Protein fractional synthesis rates were weighted by the peptide count and averaged according to their KEGG pathway involvements. We used the Uniprot.ws package in R from Bioconductor to find mappings between UniProt accession numbers and their corresponding KEGG IDs for each protein. Tables were generated for the entire known proteome for mice. We then used the Bio.KEGG module of Biopython in Python to access the REST API of the KEGG database to get a list of pathways to which each protein belongs. A set of all the pathways relevant to the experiment was generated and each protein and its corresponding fold change value were assigned to each pathway. KEGG pathways with no less than five proteins were used for representation of the data.

Tissue preparation for gas chromatography-mass spectrometry (GC-MS)
A chloroform methanol extraction was used to isolate lipids from the liver tissue. These lipids were run on a thin-layer chromatography (TLC) plate to separate phospholipid and triglyceride fractions. These fractions containing the palmitate were further derivatized for GC-MS analysis.

Gas chromatography-mass spectrometry (GC-MS) analysis
Palmitate and cholesterol isotopic enrichments were measured by GC-MS (Agilent models 6890 and 5973; Agilent, Inc., Santa Clara, CA) using helium carrier gas, a DB-225 (DB 17 for cholesterol and DB 225 for palmitates) fused silica column (30M x 0.25mm ID x 0.25um), electron ionization mode, and monitoring m/z 385, 386, and 387 for palmitates, and 368, 369, 370 for cholesterol acetyl derivatives, for M0, M1, and M2 respectively, as previously described[53,54]. Palmitate methyl ester enrichments were determined by GC-MS using a DB-17 column (30M x 0.25mm ID x 0.25um), with helium as carrier gas, electron ionization mode, and monitoring m/z 270, 271, and 272 for M0, M1, and M2. Baseline unenriched standards for both analytes were measured concurrently to correct for abundance sensitivity.

Calculation of de novo lipogenesis (DNL) and cholesterol synthesis
The measurement of newly synthesized fatty acids and total cholesterol formed during $^{2}H_2O$ labeling period was assessed using a combinatorial model of polymerization biosynthesis, as described previously[53,54]. Mass isotopomer distribution analysis (MIDA) along with body $^{2}H_2O$ enrichment, representing the precursor pool enrichment (p), is used to determine the theoretical maximum enrichment of each analyte. Using the measured deuterium enrichments, fractional and absolute contributions from DNL are then calculated. The value for f DNL represents the fraction of total triglyceride or phospholipid palmitate in the depot derived from DNL during the labeling period, and absolute DNL represents grams of palmitate synthesized by the DNL pathway.

RNAseq
RNA was isolated using standard Trizol protocol and RNA concentrations were obtained using a Nanodrop. Library preparation was performed using Kapa Biosystems mRNA Hyper Prep Kit. Sequencing was performed using NovaSeq, mode SR100 through the Vincent J. Coates Genomic

Sequencing Core at University of California, Berkeley. Trimmed fastq reads were then aligned to the mouse genome and analyzed using Qiagen CLC Workbench Software. Differentially expressed genes were initially separated based on their direction (up/down). We then looked at which processes were enriched given the differentially expressed gene set with GOrilla[55]. We did a negative-log transform of the p-values for each significant enrichment and generated a figure using the Matplotlib package in Python.

Electron Microscopy

Electron microscopy was performed at the UC Berkeley Electron Microscope Laboratory. Samples were no larger than 0.5 mm and were agitated at each step. Samples were fixed for 1 hour in 2% glutaraldehyde in 0.1M sodium cacodylate buffer, pH 7.2, rinsed for 10 minutes in 0.1M sodium cacodylate buffer, pH 7.2 three times, put in 1% osmium tetroxide in 1.6% potassium ferricyanide for 1 hour, rinsed for 10 minutes in 0.1M sodium cacodylate buffer, pH 7.2, three times. Dehydrated in acetone: 35% acetone 10 minutes, 50% acetone 10 minutes, 70% acetone 10 minutes, 80% acetone 10 minutes, 95% acetone 10 minutes, 100% acetone 10 minutes, 100% acetone 10 minutes, 100% Acetone 10 minutes. Samples were then infiltrated with 2:1 acetone:resin (accelerator) for 1 hour, 1:1 acetone:resin for 1 hour, 75% acetone 25% resin overnight. The next morning, samples were put in pure resin for 1 hour, changed three times, and then pure resin plus accelerator for 1 hour. Samples were embedded into molds at 60℃ for 2 days with pure resin and accelerator. Samples were then visualized via the TECNAI 12 TEM.

Hematoxylin and eosin staining

Hematoxylin and eosin staining was performed at the UCSF Biorepository and Tissue. Images were collected with a Zeiss Plan-Apochromat 20x/0.8NA (WD=0.55mm) M27 Biomarker Technology Core. Imaging was conducted in a Zeiss Axio Scan.Z1 whole slide scanner objective lens in the brightfield mode with Hitachi HV-F202 camera.

3. Aging alters the metabolic flux signature of the ER unfolded protein response

3.1 Introduction

Loss of protein homeostasis, or proteostasis, is a central hallmark of aging and may explain why certain diseases become manifest as organisms grow older[15]. Proteostasis involves coordination of the synthesis of new proteins, quality control of the proteome and adaptive mechanisms to reduce unfolded and misfolded proteins and prevent abnormal protein aggregation[1]. Proteins are synthesized in the endoplasmic reticulum (ER) and chaperones aid in the proper folding of newly synthesized proteins and assist when protein misfolding occurs. Accumulation of misfolded proteins in the ER stimulates the unfolded protein response (UPR^{ER}), an integrated set of adaptations that clear misfolded protein aggregates and either restore more normal proteostasis or ultimately eliminate affected cells through apoptosis[10,57]. The UPR^{ER} consists of three downstream pathways initiated by inositol-requiring enzyme-1 (IRE1), PKR-like ER kinase (PERK), and activating transcription factor 6 (ATF6), all of which are anchored in the ER membrane. ER-localized binding immunoglobulin protein (BiP), also identified as glucose-regulated protein 78-kD (GRP78), is one of the responders to misfolded proteins in the ER and acts as a regulator of the UPR^{ER} [9]. Downstream effects include global suppression of protein translation, with the exception of key proteins involved in a rescue response such as chaperones and lipogenic proteins[34]. If ER stress is unable to be resolved, cells undergo apoptosis[58]. Unmitigated ER stress may be a central component of many diseases, including metabolic disorders such as fatty liver disease and insulin resistance[2,59].

In addition to aiding in restoration of proteostasis through slowing of global protein translation, the UPR^{ER} initiates ER membrane expansion through incorporation of fatty acids into the membrane to accommodate for aggregating proteins and chaperones that are recruited to assist in disaggregation or refolding[14]. Added ER surface may also help with the synthesis of necessary compensatory factors, such as nascent proteins and lipids. The source of these lipids incorporated into hepatocyte ER was previously unknown, but we recently discovered that the source in liver was mobilized free fatty acids from adipose tissue during ER stress rather than from local *de novo* lipogenesis[30]. Tunicamycin induced ER stress in mice leads to reduction of lipogenic gene expression and *de novo* lipogenesis in the liver [30,12,13]. Alterations in protein and lipid fluxes, including membrane expansion, are crucial elements of the ER stress response yet remain poorly understood metabolically [2–5]..

Although the UPR^{ER} has been shown to decline with age in *C. elegans*[16], among other organisms, it is not fully understood how age induced shifts in metabolism may impair an organisms' ability to handle proteotoxic stress. Because proteins involved in the UPR may continue to be rapidly translated whereas translation of other proteins is suppressed through phosphorylation of eIF2α by PERK[60,19], measurement of protein fluxes provides a potentially powerful tool for identifying UPR^{ER} regulators and signatures. In this study, we measured both proteome-wide replacement rates and *de novo* lipogenesis (DNL) through stable isotope labeling. We describe a flux "signature" of the unfolded protein response in mice, which reveals proteins

potentially involved in the rescue response of the UPR^{ER}. Heavy water labeling in this experiment also allowed measurement of newly synthesized fatty acids, such as palmitate, and incorporation into both phospholipids and triglycerides under induced ER stress [54]. Phospholipids are especially of interest due to their incorporation into ER membranes under times of ER stress[61,62]. We show changes in metabolic fluxes in response to ER stress that reveal less effective proteostasis with age.

3.2 Results

12-week-old and 80-week-old male mice (n=5 per group) were treated with 1 mg/kg tunicamycin once per day over a 4-day treatment period or received DMSO injections (controls) to generate chronic ER stress. Tunicamycin inhibits N-linked glycosylation, leading to the accumulation of misfolded proteins[6]. Mice were administered $^{2}H_2O$ (deuterated or heavy water), beginning at the time of the initial tunicamycin treatment. Proteins synthesized after tunicamycin treatment incorporate deuterium-labeled amino acids, whereas pre-existing proteins will not have ^{2}H label in covalent C-H bonds of amino acids, enabling the measurement of proteins that were newly synthesized during the period of exposure to tunicamycin[19]. The metabolic labeling with heavy water also quantifies newly synthesized lipids *in vivo* (figure S1). Response to tunicamycin induced activation of the UPR^{ER} was characterized by proteome wide changes in translation rates and changes in *de novo* synthesis of palmitate incorporated into isolated phospholipid or triglyceride fractions.

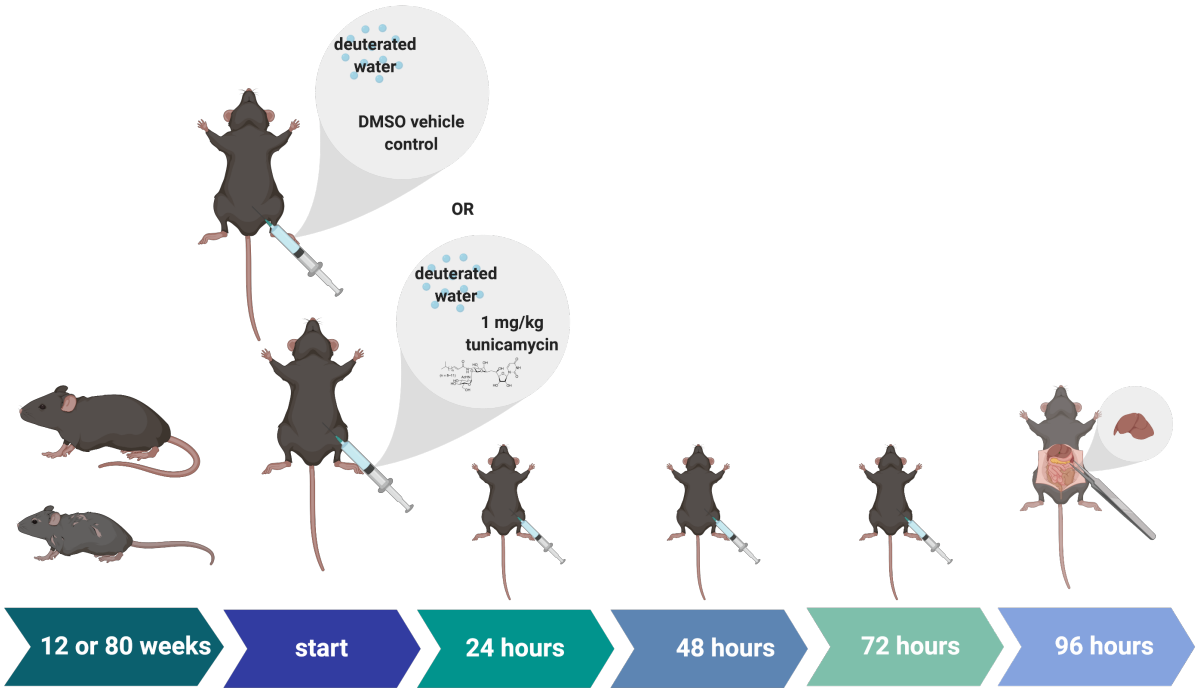

Figure 3.1. Study design. 12-week-old or 80-week-old mice (n=5 per group) were treated with 1 mg/kg tunicamycin or vehicle control, DMSO, once per day for 3 days. Mice were injected with 35uL/g deuterated water on day 1. Mice were sacrificed and livers were taken on day 4.

Proteome wide changes in translation signatures with initiation of the UPR

The fractional synthesis or replacement rates of proteins translated during the treatment period were measured. Key UPR^{ER} proteins, including protein disulfide isomerases, BiP, endoplasmin,

and calreticulin, were translated at higher rates than most global protein translation at 96 hours post initial tunicamycin treatment (figure 1a). We have elsewhere shown that global protein synthesis rates are markedly suppressed during the first 6 – 72 hours after acute tunicamycin administration in livers of young mice[30]. Global protein translation rates here in young mice under chronic ER stress were generally not different from controls at 96 hours (figure 1b). Proteins were organized by their KEGG-pathways to calculate pathway specific rates of protein translation and determine the fold-change in protein synthesis rate by KEGG-pathway (figure 1c). Under chronic ER stress conditions in young mice, protein processing in the ER was the most upregulated ontology at 2.6-fold higher under ER stress conditions as compared to control. *Fatty acid degradation* and *PPAR signaling* were two of the most suppressed ontologies. Other ontologies were mostly unaffected.

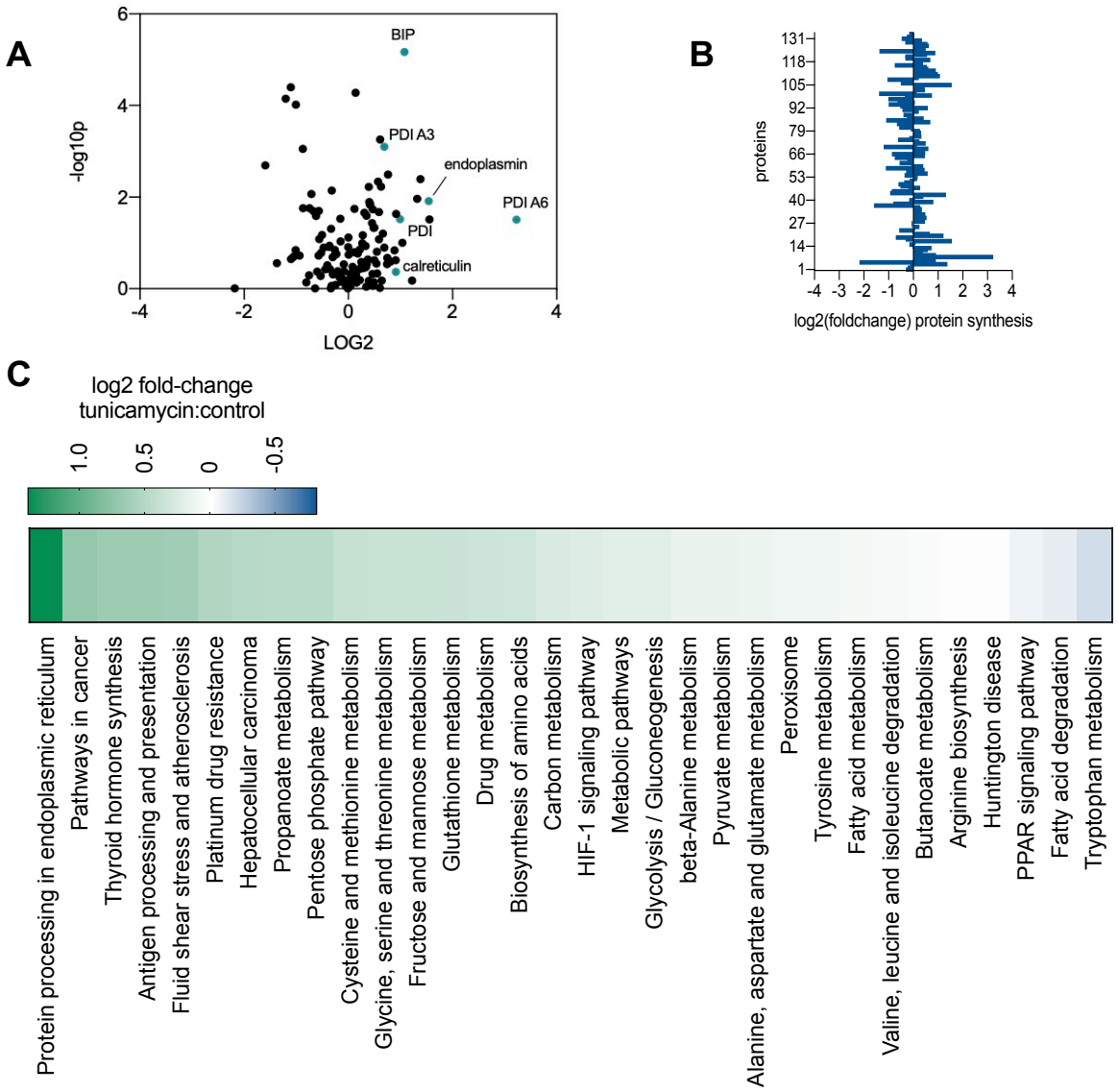

Figure 3.2. (a) Volcano plot of all hepatic proteins for which fractional synthesis rates were measured (n=136) in 12-week-old mice. Points expressed as log2 fold-change tunicamycin treated/control on x-axis and - log10(p-value),

obtained from 2-tailed t-test, on y-axis. (b) log2 fold-change of individual protein translation rates of tunicamycin treated/control. (c) KEGG-pathway analysis for fractional synthesis rates of proteins from 12-week-old mice tunicamycin treated/control. n = at least 5 proteins per pathway.

Age induced changes to characterized UPR signature

In contrast, aged mice exhibited a strikingly different response to chronic ER stress compared to their younger counterparts (figure 2a-b). Aged mice experienced broad inhibition of protein translation at 4 days of tunicamycin administration, with most ontologies showing suppression of protein synthesis. Proteins in the ontology *protein processing in the ER* remained more highly upregulated than in the young mice, with a 2.6-fold increase in synthesis rates compared to tunicamycin challenged young mice. Ontologies pertaining to lipid metabolism, including *PPAR signaling*, *fatty acid metabolism*, and *fatty acid degradation* were more suppressed in the aged mice as compared to young mice challenged with tunicamycin (figure 2b). Overall, when challenged with tunicamycin, aged mice showed much lower rates of translation across most ontologies than in control age-matched animals (figure 3). In contrast, those ontologies that were upregulated remained as highly translated as the younger mice. When compared directly, under ER stress conditions most ontologies in aged mice were significantly suppressed in their synthesis compared to young mice (figure 3), with the exception of higher rates of synthesis of the ontology *protein processing in the ER*.

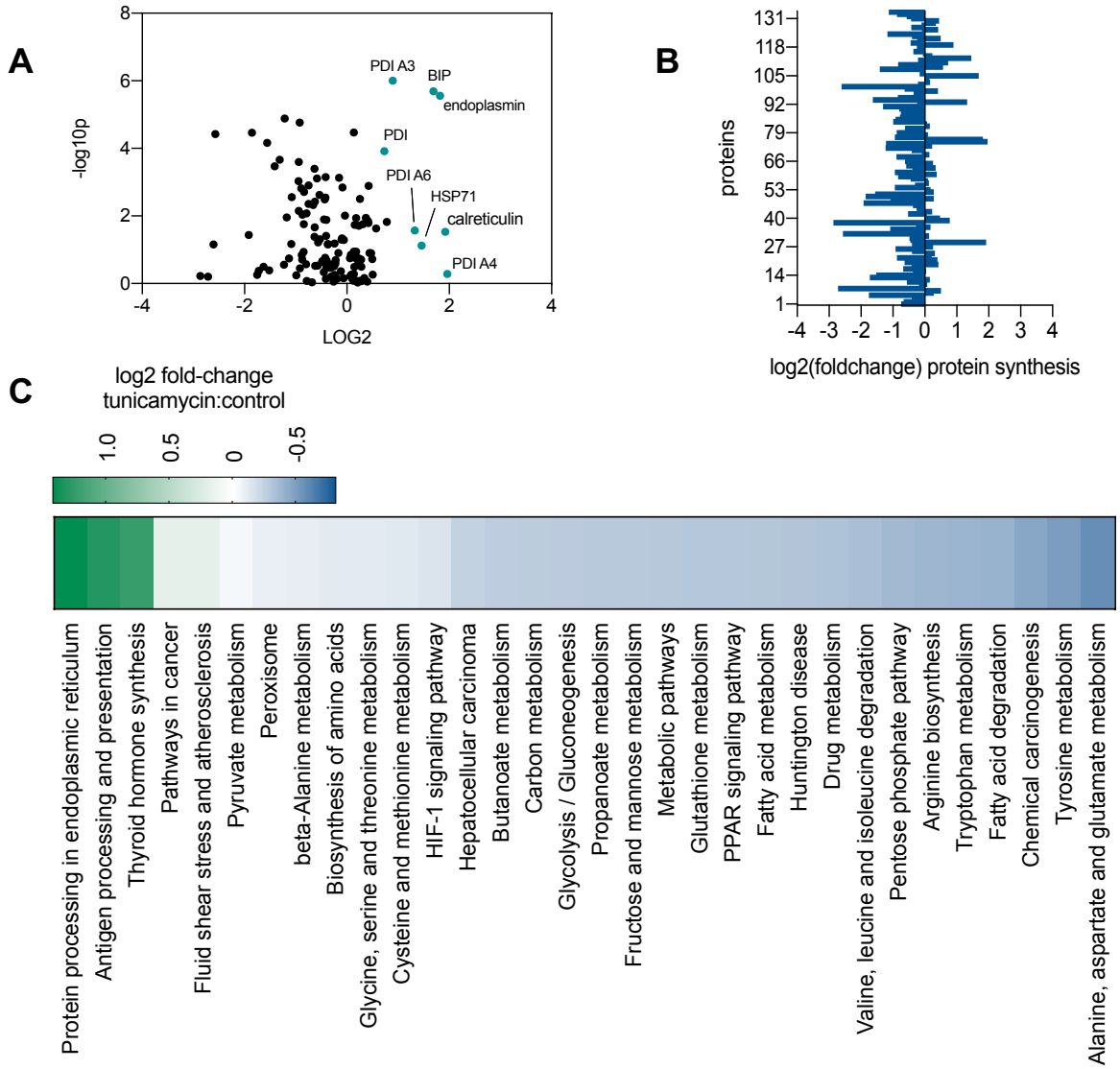

Figure 3.3. (a) Volcano plot of all proteins for which fractional synthesis rates were measured (n=136) in 80-week-old mice. Points expressed as log2 fold-change tunicamycin treated/control on x-axis and - log10(p-value), obtained from 2-tailed t-test, on y-axis. (b) log2 fold-change of individual protein translation rates of tunicamycin treated/control. (c) KEGG-pathway analysis for fractional synthesis rates of proteins from 80-week-old mice tunicamycin treated/control. n = at least 5 proteins per pathway.

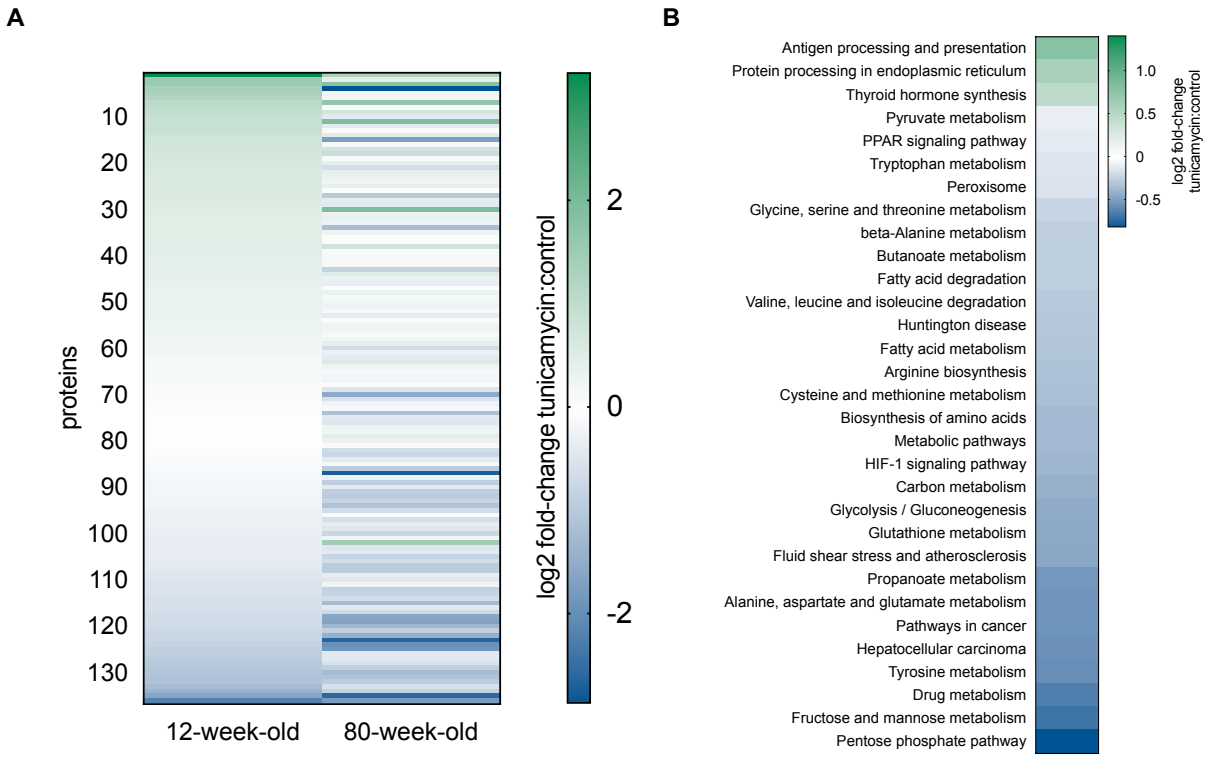

Figure 3.4. Effects of age on global protein synthesis rates with tunicamycin treatment for paired proteins in young and aged mice. (a) Proteome-wide tunicamycin induced changes in individual protein translation rates (n=136 proteins). Values expressed as log2 fold-change of tunicamycin treated/control. 12-week-old mice values expressed on the left, and protein matched 80-week-old values expressed on the right. (b) KEGG-pathway analysis of the log2 fold-change of 80-week-old-mice treated with tunicamycin to 12-week-old-mice treated with tunicamycin (1=no change). n = at least 5 proteins per pathway.

BiP synthesis is higher with aging under ER stress conditions

BiP, a key chaperone involved in the UPR, was much more rapidly synthesized in aged mice challenged with tunicamycin compared to young mice (figure 4). BiP synthesis increased by ~2-fold in young mice under ER stress but by more than 3-fold in aged mice under ER stress conditions, showing significant greater translation of BiP in aged tunicamycin challenged compared to young ($p < 0.001$). To compare rates of translation to mRNA levels, *bip* mRNA was measured via RT-qPCR. *bip* mRNA in liver showed no significant difference in young mice challenged with tunicamycin, however, was 9.2-fold higher in aged mice challenged with tunicamycin as compared to control. *xbp1s* mRNA, a spliced version of *xbp1* indicative of initiation of the UPR[63], was also measured. Young mice showed no significant differences when challenged with tunicamycin, however, aged mice showed a 3.5-fold increase (figure 4). Abundance of BiP protein was measured via western blot, and no differences between young and aged were seen after challenge with tunicamycin.

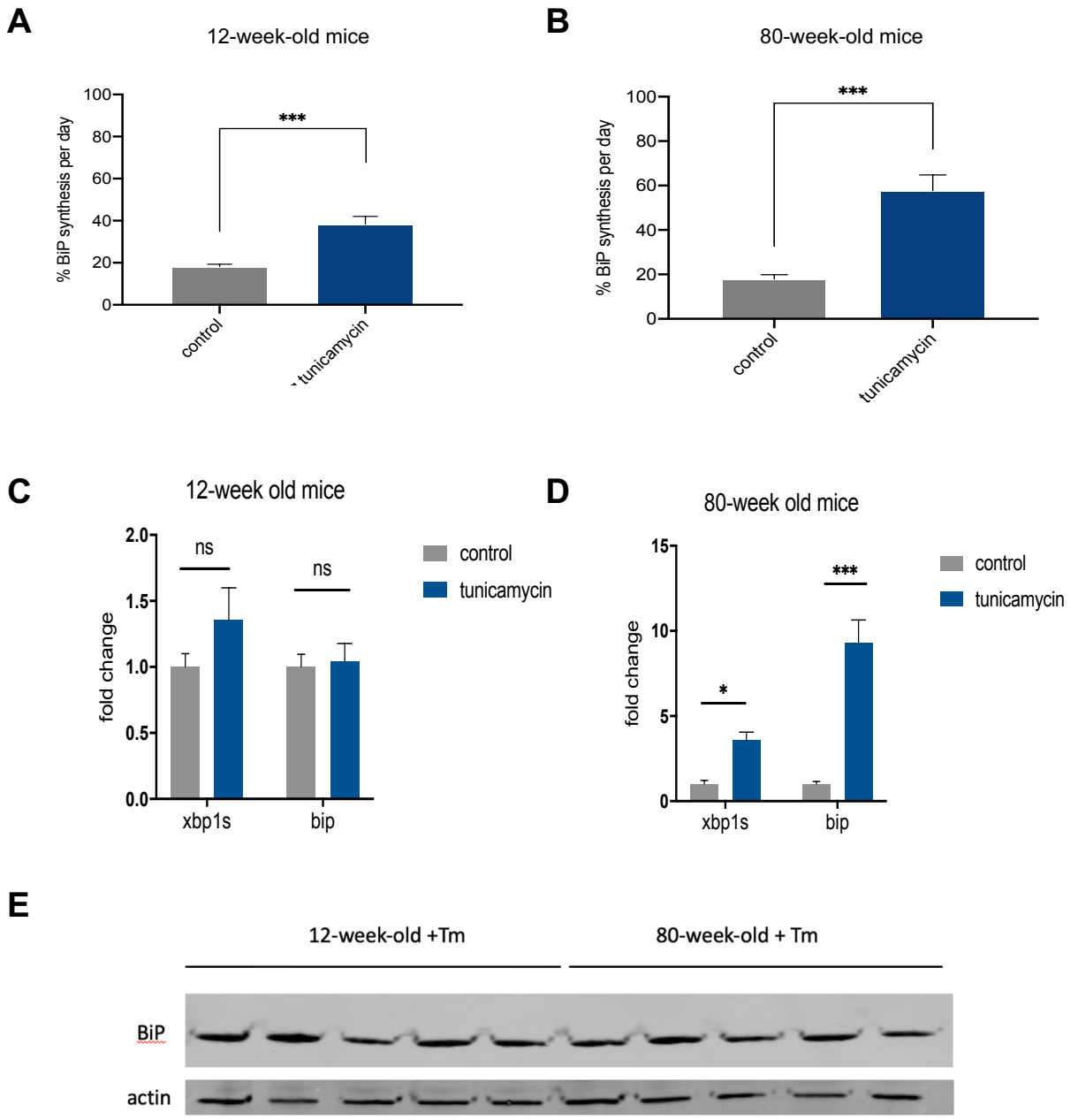

Figure 3.5. (a) BiP protein synthesis rate per day for 12-week-old mice (n=5). (b) BiP protein synthesis rate per day for 80-week-old mice (n=5). (c) RT-qPCR for bip and xbp1s in 12-week-old mice (n=5). (d) RT-qPCR for bip and xbp1s in 80-week-old mice (n=5). (e) Western blot for BiP and loading control, actin, for 12-week-old mice vs 80-week-old mice treated with tunicamycin. (n=5 per group). ns= no significance, * = <0.05, ** = < 0.01, *** = < 0.001.

De novo lipogenesis (DNL) is suppressed by both induction of the UPR and age

The contribution from DNL to liver lipids during the treatment period was measured. Rates of DNL were measured for both palmitate incorporated into hepatic phospholipid and triglyceride fractions. Young mice experiencing chronic ER stress showed a significant reduction in *de novo* palmitate incorporation into triglycerides but there was no significant change in DNL contribution to phospholipids. In contrast, aged mice experiencing chronic ER stress displayed a

significant reduction in *de novo* palmitate incorporation into both triglyceride and phospholipid fractions (figure 5).

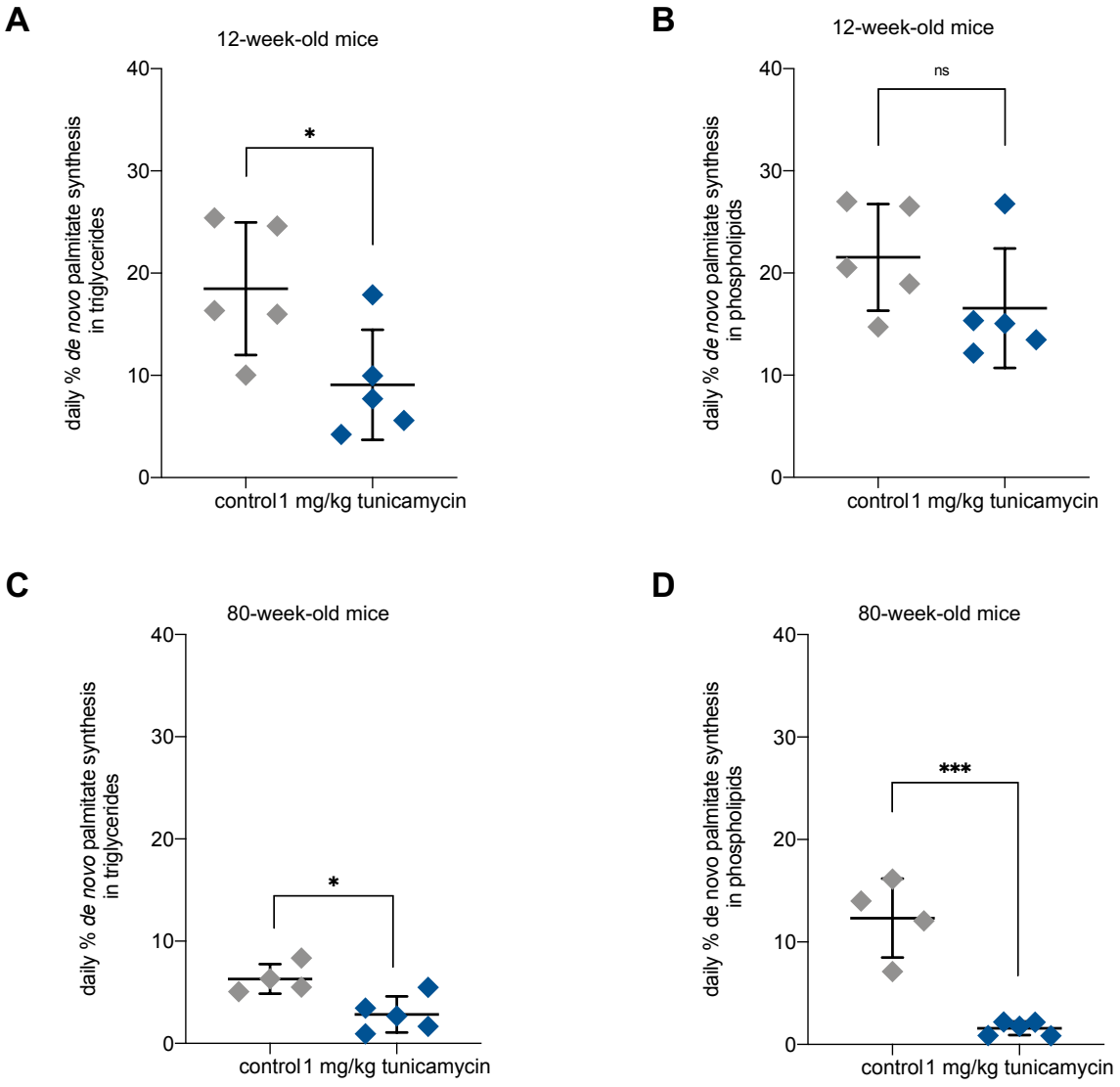

Figure 3.6. (a) De novo lipogenesis (DNL) fractional contribution to palmitate incorporated into triglycerides in 12-week-old control and tunicamycin treated mice (n=5 per group). (b) DNL contribution to palmitate incorporated into phospholipids in 12-week-old control and tunicamycin treated mice (n=5 per group). (c) DNL contribution to palmitate incorporated into triglycerides in 80-week-old control and tunicamycin treated mice (n=5 per group). (d) DNL contribution to palmitate incorporated into phospholipids in 80-week-old control and tunicamycin treated mice (n=5 per group). ns= no significance, * = <0.05, ** = < 0.01, *** = < 0.001.

3.3 Discussion

Several observations are of interest related to metabolic fluxes induced by chronic ER stress. Young mice challenged with chronic ER stress for 4 days demonstrated increased

translation of proteins involved in *protein processing in the ER*, however, showed modest changes in other ontologies. We have previously shown that acute tunicamycin administration in mice markedly reduces protein synthesis across the global proteome in liver for the first 72 hours[30]. The data here suggest that by day 4 of repeated tunicamycin treatment, these mice may be starting to recover from the induced ER stress. In contrast, with chronic ER stress synthesis rates of key UPR^{ER} regulators such as chaperones and BiP remained upregulated. The increase of chaperones and BiP synthesis with suppressed synthesis of proteins involved in lipid metabolism indicates a still partially active UPR, but with no reduction in most other ontologies. Interestingly, we found significantly increased BiP synthesis rates despite no change in *bip* mRNA levels after UPR induction in young mice. This again demonstrates that directly measuring protein synthesis rates may be more sensitive to changes in translational activity than measurement of mRNA levels[64].

Aged mice experiencing chronic ER stress showed a more exaggerated UPR signature compared to their young counterparts. Aged mice had suppressed rates of translation across the proteome but sustained the same increase in translation of proteins involved in *protein processing in the ER*. This ontology (supplementary table 2) encompasses many known UPR proteins such as BiP and protein disulfide isomerases seen in our data set. BiP synthesis was indeed significantly increased in aged mice challenged with tunicamycin as compared to young mice, which was consistent with *bip* mRNA levels. Abundance of BiP protein by Western blot appeared to be the same when measured in both young and aged mice challenged with tunicamycin, in contrast to higher message levels and synthesis rates increased in aged mice. This may be indicative of more rapid clearance of BiP in aged mice, compensating for higher synthesis rate, or may reflect less sensitivity of the protein measurement. These data highlight the complex translational control mechanisms used to restore protein homeostasis. Overall,we saw suppression of protein synthesis rates for most ontologies in aged mice under ER stress conditions but not in young mice at day 4 of tunicamycin administration, exemplifying an exaggerated UPR^{ER} in the aged animals. A decrease in glutathione metabolism in aged mice under ER stress conditions compared to young mice was seen as well, which may predispose to altered redox homeostasis[65].

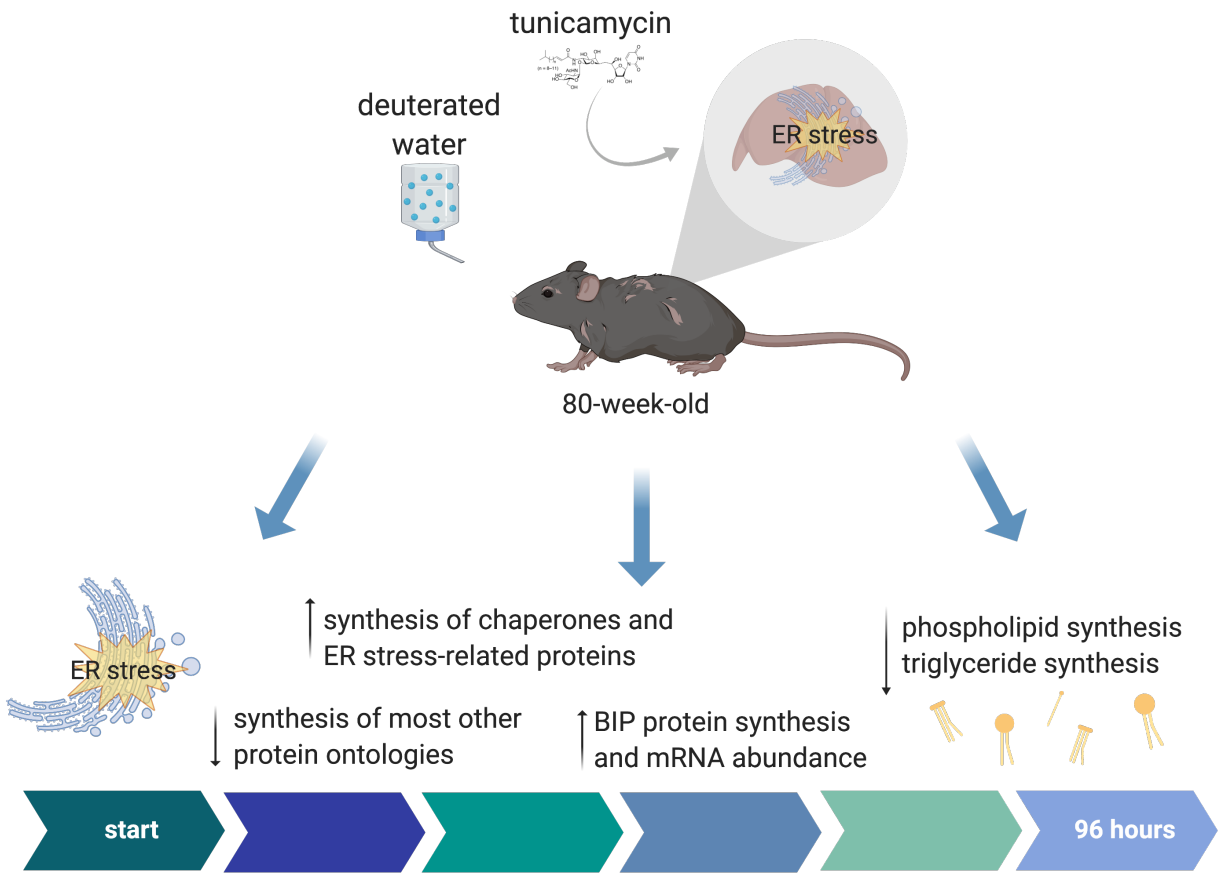

Figure 3.7. Summary figure. Exaggerated UPR signature in aged animals, with higher translation of ER stress-related proteins, lower translation of all other proteins, lower rates of de novo lipogenesis, and BiP protein synthesis and mRNA abundance higher in aged animals with tunicamycin induced ER stress.

Ontologies involved in lipid metabolism, such as *fatty acid degradation* and *PPAR signaling* were more suppressed in aged mice challenged with tunicamycin, which was consistent with our data showing *de novo* fatty acid synthesis rates were more broadly reduced with aging and ER stress. These categories are likely related to fatty acid beta-oxidation programmed by PPARα. Hence, decreased lipid degradation might also be contributing to aging-related hepatic lipid accumulation and non-alcoholic fatty liver disease. Aged mice showed a more striking decline in DNL as compared to young mice, specifically in the phospholipid fraction. Phospholipids comprise membranes, so reduced *de novo* synthesis their ability to expand their ER membranes under states of ER stress[44]. In contrast, young mice exhibited decline in DNL contribution to palmitate incorporated into triglycerides, but not phospholipids. We have previously shown that with acute ER stress, palmitate synthesis and incorporation into phospholipids declines starting 48 hours after tunicamycin treatment and remains significantly decreased at 72 hours post treatment[30]. In this chronic ER stress phenotype after 4 days we see no significant decline in DNL of phospholipid fractions, which suggests young mice are better able to resume synthesis of palmitate and subsequent incorporation into phospholipids after 4 days of repeated ER stress. Other groups have seen a similar lower DNL phenotype *in vivo* as well[12,13], indicative of a systemic difference in lipogenic response to UPR^{ER} induction *in vivo* as compared to cellular models[11] which typically show increased rates of lipogenesis under ER

stress. These differences can be reconciled by the ability of a whole organism to draw from other tissues for lipid sources *in vivo*. We have previously shown that fatty acids are taken up by the liver and utilized from other tissues, such as the adipose tissue, under ER stress conditions[30]. In yeast, ER membrane expansion has been seen with initiation of the UPR, so it might be speculated that this decrease in phospholipid synthesis in aged mice could hinder their ability to recover from ER stress[14].

We conclude that aging leads to an exaggerated chronic ER stress metabolic signature, including ongoing suppression of synthesis in most protein ontologies, with the exception of *protein processing in the ER*, which remains upregulated (figure 6). These data in combination with higher BiP synthesis and dysregulated lipid metabolism in aged mice that are challenged with tunicamycin indicate that aged mice are not as efficient at handling and recovering from ER stress: they sustained high levels of BiP synthesis throughout the 4-day treatment period, whereas young mice showed less increase in BiP synthesis and no significant upregulation of *bip* mRNA; they exhibited prolonged suppression of proteome-wide protein synthesis, whereas young mice showed no general suppression at day 4 of tunicamycin; and they exhibited much greater suppression of *de novo* synthesis of liver lipids, particularly phospholipids which may be required for membrane expansion. In summary, our data suggests that aging leads to impaired efficiency of the UPR^{ER}, leading to a prolonged and exaggerated UPR metabolic flux signature. This impairment in the UPR^{ER} with age may be a contributing factor to diseases that manifest with age. In the liver, specifically, a less capable UPR^{ER} and decreased lipid degradation with aging may contribute to metabolic diseases including non-alcoholic fatty liver disease.

Table 3.1. Individual protein synthesis rate ratios of aged control mice treated with tunicamycin. Ratio of above 1 indicates a higher synthesis rate with age and/or tunicamycin treatment. Ratio of below 1 indicates a lower synthesis rate with age and/or tunicamycin treatment.

Protein	ratio aged tm/control	ratio young tm/control	ratio aged tm/young tm
10 kDa heat shock protein, mitochondrial	1.21	1.11	1.10
2-iminobutanoate/2-iminopropanoate deaminase	0.83	1.00	0.83
3-hydroxyacyl-CoA dehydrogenase type-2	0.35	1.06	0.33
3-ketoacyl-CoA thiolase A, peroxisomal	1.41	1.00	1.41
3-ketoacyl-CoA thiolase B, peroxisomal	0.76	0.79	0.95
3-ketoacyl-CoA thiolase, mitochondrial	0.76	0.89	0.85
40S ribosomal protein S4, X isoform	1.42	1.31	1.08
60 kDa heat shock protein, mitochondrial	1.10	1.19	0.92
60S ribosomal protein L29	0.90	1.08	0.83
60S ribosomal protein L6	1.72	1.38	1.24
Actin, alpha skeletal muscle	1.17	1.19	0.98
Actin, cytoplasmic 2	1.11	1.11	1.00
Acyl-CoA synthetase family member 2,	0.43	0.48	0.88

mitochondrial			
Acyl-CoA-binding protein	0.57	0.69	0.83
Acyl-coenzyme A synthetase ACSM1, mitochondrial	1.05	1.50	0.70
Adenosylhomocysteinase	1.10	1.37	0.80
Alanine--glyoxylate aminotransferase 2, mitochondrial	0.30	1.69	0.18
Alcohol dehydrogenase 1	0.43	0.67	0.64
Alcohol dehydrogenase class-3	0.58	0.78	0.74
Aldehyde dehydrogenase family 8 member A1	0.96	1.39	0.69
Aldehyde dehydrogenase, cytosolic 1	0.64	1.17	0.55
Aldehyde dehydrogenase, mitochondrial	0.73	0.79	0.92
Alpha-1-antitrypsin 1-3	0.84	1.41	0.60
Alpha-enolase	0.77	0.94	0.81
Arginase-1	0.77	1.13	0.68
Argininosuccinate synthase	1.11	1.34	0.83
Aspartate aminotransferase, mitochondrial	0.80	1.30	0.62
ATP synthase subunit alpha, mitochondrial	0.73	1.02	0.72
ATP synthase subunit beta, mitochondrial	0.69	1.06	0.66
Betaine--homocysteine S-methyltransferase 1	0.69	0.50	1.38
Bifunctional epoxide hydrolase 2	0.78	1.24	0.63
Calreticulin	3.79	1.88	2.01
Carbamoyl-phosphate synthase [ammonia], mitochondrial	0.64	0.97	0.66
Carbonic anhydrase 2	0.15	0.91	0.17
Carbonic anhydrase 3	0.17	0.33	0.51
Carboxylesterase 1D	0.26	0.57	0.46
Carboxylesterase 1F	0.34	0.65	0.52
Carboxylesterase 3A	0.38	0.60	0.63
Carboxylesterase 3B	0.56	0.39	1.45
Catalase	0.74	0.72	1.03
Clathrin heavy chain 1	0.86	1.04	0.82
Cystathionine gamma-lyase	1.13	2.34	0.48
Cysteine sulfinic acid decarboxylase	0.16	0.59	0.28
Cytochrome c oxidase subunit 6A1, mitochondrial	1.22	1.00	1.21

Cytochrome P450 2D10	0.94	1.85	0.51
Cytosolic 10-formyltetrahydrofolate dehydrogenase	0.53	0.93	0.57
D-dopachrome decarboxylase	1.19	1.20	0.99
Delta-1-pyrroline-5-carboxylate dehydrogenase, mitochondrial	0.65	0.68	0.96
Electron transfer flavoprotein subunit alpha, mitochondrial	0.97	1.08	0.90
Electron transfer flavoprotein subunit beta	0.84	1.16	0.73
Elongation factor 1-alpha 1	1.29	1.41	0.91
Elongation factor 2	0.86	0.70	1.22
Endoplasmic reticulum chaperone BiP	3.22	2.11	1.53
Endoplasmin	3.53	2.92	1.21
Estradiol 17 beta-dehydrogenase 5	0.32	0.64	0.50
Fatty acid synthase	0.93	1.61	0.58
Fatty acid-binding protein, liver	0.52	0.47	1.12
Ferritin light chain 1	1.10	1.25	0.88
Formimidoyltransferase-cyclodeaminase	1.39	1.75	0.79
Fructose-1,6-bisphosphatase 1	1.33	1.50	0.88
Fructose-bisphosphate aldolase B	0.84	1.31	0.64
Fumarylacetoacetase	0.75	1.02	0.74
Glutamate dehydrogenase 1, mitochondrial	0.55	0.61	0.89
Glutathione peroxidase 1	0.65	0.78	0.83
Glutathione S-transferase A1	0.52	0.76	0.69
Glutathione S-transferase A3	0.47	0.87	0.54
Glutathione S-transferase Mu 1	1.17	2.50	0.47
Glutathione S-transferase Mu 3	1.34	2.95	0.46
Glutathione S-transferase P 1	0.52	0.77	0.68
Glyceraldehyde-3-phosphate dehydrogenase	0.85	1.26	0.67
Glycine N-methyltransferase	1.26	1.53	0.83
Glycogen phosphorylase, liver form	0.56	0.70	0.80
Glyoxylate reductase/hydroxypyruvate reductase	1.11	1.33	0.83
Heat shock cognate 71 kDa protein	2.75	0.80	3.44
Heat shock protein HSP 90-beta	0.75	1.47	0.51
Hemoglobin subunit alpha	0.60	0.81	0.73

Hemoglobin subunit beta-1	0.63	0.85	0.74
Homogentisate 1,2-dioxygenase	0.50	1.50	0.34
Hydroxyacyl-coenzyme A dehydrogenase, mitochondrial	0.47	0.47	1.01
Hydroxymethylglutaryl-CoA lyase, mitochondrial	1.07	0.99	1.08
Hydroxymethylglutaryl-CoA synthase, mitochondrial	0.96	1.28	0.75
Isochorismatase domain-containing protein 2A	0.77	1.88	0.41
Isocitrate dehydrogenase [NADP] cytoplasmic	1.07	0.84	1.27
L-lactate dehydrogenase A chain	0.86	1.00	0.86
Major urinary protein 1	0.55	0.89	0.61
Major urinary protein 17	0.67	0.84	0.80
Major urinary protein 2	0.46	1.03	0.44
Malate dehydrogenase, cytoplasmic	1.05	1.39	0.76
Malate dehydrogenase, mitochondrial	1.32	1.59	0.83
Maleylacetoacetate isomerase	1.20	1.21	0.99
Medium-chain specific acyl-CoA dehydrogenase, mitochondrial	0.44	1.41	0.31
Methanethiol oxidase	0.75	0.55	1.37
Methylmalonate-semialdehyde dehydrogenase [acylating], mitochondrial	1.16	1.27	0.92
Microsomal glutathione S-transferase 1	0.80	0.84	0.96
NADP-dependent malic enzyme	0.75	0.52	1.44
Non-specific lipid-transfer protein	0.58	0.88	0.65
Nucleoside diphosphate kinase B	1.48	1.11	1.33
Ornithine carbamoyltransferase, mitochondrial	0.75	0.67	1.11
Peptidyl-prolyl cis-trans isomerase A	0.89	1.10	0.81
Peroxiredoxin-1	0.78	1.17	0.67
Peroxiredoxin-6	0.81	0.74	1.10
Peroxisomal acyl-coenzyme A oxidase 1	1.34	1.54	0.87
Phenylalanine-4-hydroxylase	1.27	1.27	0.99
Phosphoglucomutase-1	0.76	1.89	0.40
Phosphoglycerate kinase 1	1.21	1.40	0.87
Phosphoglycerate mutase 1	0.73	0.82	0.90
Polycystic kidney disease protein 1-like 1	0.30	0.22	1.35

Pregnancy zone protein	1.18	1.52	0.77
Protein disulfide-isomerase	1.66	1.99	0.83
Protein disulfide-isomerase A3	1.86	1.62	1.15
Protein disulfide-isomerase A4	3.90	1.46	2.67
Protein disulfide-isomerase A6	2.51	9.38	0.27
Protein/nucleic acid deglycase DJ-1	0.94	1.38	0.68
Pyruvate carboxylase, mitochondrial	0.62	0.66	0.94
Regucalcin	0.28	0.55	0.51
Retinal dehydrogenase 1	0.59	0.97	0.61
S-adenosylmethionine synthase isoform type-1	1.36	1.48	0.92
S-formylglutathione hydrolase	1.06	2.05	0.52
S-methylmethionine--homocysteine S-methyltransferase BHMT2	0.54	0.50	1.09
Sarcosine dehydrogenase, mitochondrial	1.24	0.90	1.38
SEC14-like protein 2	0.88	0.80	1.09
Selenium-binding protein 2	0.67	0.43	1.54
Serum albumin	0.40	0.63	0.64
Short-chain specific acyl-CoA dehydrogenase, mitochondrial	0.53	0.89	0.60
Sorbitol dehydrogenase	0.56	1.32	0.42
Succinate--CoA ligase [ADP/GDP-forming] subunit alpha, mitochondrial	0.14	2.61	0.05
Superoxide dismutase [Cu-Zn]	0.72	1.07	0.67
Transketolase	0.68	1.68	0.40
Trifunctional enzyme subunit alpha, mitochondrial	0.92	1.04	0.89
Triokinase/FMN cyclase	0.54	0.90	0.60
Triosephosphate isomerase	0.84	1.45	0.57
Tubulin beta-2B chain	1.09	1.27	0.86
Tubulin beta-4B chain	1.04	1.21	0.86
Valacyclovir hydrolase	1.13	0.94	1.20
Xanthine dehydrogenase/oxidase	1.12	1.68	0.67
Xylulose kinase	0.65	1.56	0.41

3.4 Materials and Methods

Animals

C57BL/6J male mice acquired from The Jackson Laboratory were used for this study. Mice were aged to either 12 or 80 weeks. All mice were housed according to the Animal Care and Use Committee (ACUC) standards in the animal facility at UC Berkeley. Mice were fed a standard chow diet and water ad libitum.

Deuterated water labeling and tunicamycin treatment in mice

Mice were labeled with deuterated water (heavy water, ^2H_2O) beginning at time point 0 (t^0) through the end of the experiment. Proteins synthesized after t^0 will incorporate deuterium-labeled amino acids, thus enabling the measurement of proteins synthesized during the period of exposure to heavy water. Deuterium is rapidly incorporated throughout the body of an organism after treatment, bringing the deuterium enrichment in body water up to 5%. Deuterium enrichment is maintained through the intake of 8% ^2H_2O given as drinking water, thus making it an optimal labeling approach for *in vivo* experimental study. Mice are injected intraperitoneally (IP) with 100% ^2H_2O containing either tunicamycin dissolved in DMSO, or DMSO control. Mice were treated at 1 mg/kg tunicamycin one per day, or no drug control, and tissues were harvested 96 hours after injections (n=5 mice per group).

Body water enrichment analysis

Mouse liver were distilled overnight upside down on a bead bath at 85°C to evaporate out body water. Deuterium present in the body water were exchanged onto acetone, and deuterium enrichment in the body water was measured via gas chromatography mass spectrometry (GC-MS)[52].

Tissue preparation for liquid chromatography-mass spectrometry (LC-MS)

Tissues were flash frozen after harvest and homogenized in homogenization buffer (100 mM PMSF, 500 mM EDTA, EDTA-free Protease Inhibitor Cocktail (Roche, catalog number 11836170001), PBS) using a 5 mm stainless steel bead at 30 hertz for 45 seconds in a TissueLyser II (Qiagen). Samples were then centrifuged at 10,000 rcf for 10 minutes at 4°C. The supernatant was saved and protein was quantified using a Pierce BCA protein assay kit (ThermoFisher, catalog number 23225). 100 ug of protein was used per sample. 25 uL of 100 mM ammonium bicarbonate solution, 25 uL TFE, and 2.3 uL of 200 mM DTT were added to each sample and incubated at 60°C for 1 hour. 10 uL 200 mM iodoacetamide was then added to each sample and allowed to incubate at room temperature in the dark for 1 hour. 2 uL of 200 mM DTT was added and samples were incubated for 20 minutes in the dark. Each sample was then diluted with 300 uL H_2O and 100 uL 100 mM ammonium bicarbonate solution. Trypsin was added at a ratio of 1:50 trypsin to protein (trypsin from porcine pancreas, Sigma Aldrich, catalog number T6567). Samples were incubated at 37°C overnight. The next day, 2 uL of formic acid was added. Samples were centrifuged at 10,000 rcf for 10 minutes, collecting the supernatant. Supernatant was speedvac'd until dry and re-suspended in 50 uL of 0.1 % formic acid/3% acetonitrile/96.9% LC-MS grade water and transferred to LC-MS vials to be analyzed via LC-MS.

Liquid chromatography-mass spectrometry (LC-MS) analysis

Trypsin-digested peptides were analyzed on a 6550 quadropole time of flight (Q-ToF) mass spectrometer equipped with Chip Cube nano ESI source (Agilent Technologies). High performance liquid chromatography (HPLC) separated the peptides using capillary and nano binary flow. Mobile phases were 95% acetonitrile/0.1% formic acid in LC-MS grade water.

Peptides were eluted at 350 nl/minute flow rate with an 18 minute LC gradient. Each sample was analyzed once for protein/peptide identification in data-dependent MS/MS mode and once for peptide isotope analysis in MS mode. Acquired MS/MS spectra were extracted and searched using Spectrum Mill Proteomics Workbench software (Agilent Technologies) and a mouse protein database (www.uniprot.org). Search results were validated with a global false discovery rate of 1%. A filtered list of peptides was collapsed into a nonredundant peptide formula database containing peptide elemental composition, mass, and retention time. This was used to extract mass isotope abundances (M0-M3) of each peptide from MS-only acquisition files with Mass Hunter Qualitative Analysis software (Agilent Technologies). Mass isotopomer distribution analysis (MIDA) was used to calculate peptide elemental composition and curve-fit parameters for predicting peptide isotope enrichment based on precursor body water enrichment (p) and the number (n) of amino acid C-H positions per peptide actively incorporating hydrogen (H) and deuterium (D) from body water. Subsequent data handling was performed using python-based scripts, with input of precursor body water enrichment for each subject, to yield fractional synthesis rate (FSR) data at the protein level. FSR data were filtered to exclude protein measurements with fewer than 2 peptide isotope measurements per protein. Details of FSR calculations and data filtering criteria were described previously[19].

Calculation of fractional replacement (f) and replacement rate constant (k) for individual proteins
Details of f calculations were previously described[15]. These values were used to generate the ratio of tunicamycin treated to untreated synthesis rates.

Statistical analysis
Data were analyzed using GraphPad Prism software (version 8.0).

Tissue preparation for gas chromatography-mass spectrometry (GC-MS)
A chloroform methanol extraction was used to isolate lipids from the liver tissue. These lipids were run on a thin-layer chromatography (TLC) plate to separate phospholipid and triglyceride fractions. These fractions containing the palmitate were further derivatized for GC-MS analysis.

Gas chromatography-mass spectrometry (GC-MS) analysis
Palmitate isotopic enrichments were measured by GC-MS (Agilent models 6890 and 5973; Agilent, Inc., Santa Clara, CA) using helium carrier gas, a DB-225 (DB 17 for cholesterol and DB 225 for palmitates) fused silica column (30M x 0.25mm ID x 0.25um), electron ionization mode, and monitoring m/z 385, 386, and 387 for palmitates for M0, M1, and M2 respectively, as previously described[53,54]. Palmitate methyl ester enrichments were determined by GC-MS using a DB-17 column (30M x 0.25mm ID x 0.25um), with helium as carrier gas, electron ionization mode, and monitoring m/z 270, 271, and 272 for M0, M1, and M2. Baseline unenriched standards for both analytes were measured concurrently to correct for abundance sensitivity.

Calculation of de novo lipogenesis (DNL)
The measurement of newly synthesized fatty acids formed during $^{2}H_2O$ labeling period was assessed using a combinatorial model of polymerization biosynthesis, as described previously[53,54]. Mass isotopomer distribution analysis (MIDA) along with body $^{2}H_2O$ enrichment, representing the precursor pool enrichment (p), is used to determine the theoretical maximum enrichment of each analyte. Using the measured deuterium enrichments, fractional and absolute contributions

from DNL are then calculated. The value for f DNL represents the fraction of total triglyceride or phospholipid palmitate in the depot derived from DNL during the labeling period, and absolute DNL represents grams of palmitate synthesized by the DNL pathway.

Western blot

Starting with frozen tissue, tissue was homogenized in homogenization buffer (100 mM PMSF, 500 mM EDTA, EDTA-free Protease Inhibitor Cocktail (Roche, catalog number 11836170001), PBS) using a 5 mm stainless steel bead at 30 hertz for 45 seconds in a TissueLyser II (Qiagen). Samples were then centrifuged at 10,000 rcf for 10 minutes at 4C. The supernatant was saved and protein was quantified using a Pierce BCA protein assay kit (ThermoFisher, catalog number 23225). 30 ug of protein was used per sample. 2X Laemmli sample buffer was added (Sigma, catalog number S3401) at a 1:1 ratio. Samples were brought to the same volume with 1% SDS, vortexed briefly, and heated in a heating block for 10 minutes at 95°C. Samples were tip sonicated for 10 seconds and then centrifuged for 5 minutes at 15,000 g. 4-12% gradient poly-acrylamide gels were used with MES buffer and gels were run at 120V until loading dye line passed through gel. iBlot2 was used to transfer the gel onto a PVDF membrane. Membranes were washed 3 times with PBST and then blocked with 5% milk for 1 hour. Membranes were then washed again with PBST 3 times. BiP (Cell Signaling Technology, catalog number 3183S) and actin (Santa Cruz technology, catalog number 47778) antibodies were diluted in 5% BSA and rotated at 4°C overnight. Membranes were then washed 3 times with PBST, and LiCor secondary antibodies diluted in 5% BSA were added and rotated for 2 hours at room temperature. Membranes were washed 3 times with PBST and then imaged using a LiCor imaging system.

Quantitative reverse transcription PCR (RT-qPCR)

RNA was isolated using standard Trizol protocol and RNA concentrations were obtained using a Nanodrop. After normalizing concentrations, cDNA was synthesized using 2 ug RNA with RevertAid RT Kit (Thermofisher, catalog number K1691). Maxima SYBR Green/ROX qPCR Master Mix (ThermoFisher, catalog number K0221) was used for RT-qPCR. Actin was used to normalize. Oligonucleotide sequences used:

bip F: CGAGGAGGAGGACAAGAAGG
bip R: CACCTTGAACGGCAAGAACT
xbp1s forward: TGCTGAGTCCGCAGCAGGTG
xbp1s reverse: GCTGGCAGGCTCTGGGGAAG
actin forward: CGAATCATGAGCATTGTAGAC
actin reverse: GTAATTCTTATCTCCAGCCAG

KEGG pathway analysis

Protein fractional synthesis rates were weighted by the peptide count and averaged according to their KEGG pathway involvements. We used the Uniprot.ws package in R from Bioconductor to find mappings between UniProt accession numbers and their corresponding KEGG IDs for each protein. Tables were generated for the entire known proteome for mice. We then used the Bio.KEGG module of Biopython in Python to access the REST API of the KEGG database to get a list of pathways to which each protein belongs. A set of all the pathways relevant to the experiment was generated and each protein and its corresponding fold change value were assigned to each pathway. KEGG pathways with no less than five proteins were used for representation of the data.

4. Region-specific shifts in metabolic flux in the aging brain

4.1 Introduction

Aging is the most significant risk factor in the development of neurodegenerative disease. The accumulation of protein aggregates and protein dysregulation is a major feature of complex disorders associated with impaired cognition, including Alzheimer's disease, Parkinson's disease, Huntington's disease, and prion disease[15]. By inference, protein homeostasis is likely a crucial factor in maintaining brain health. Loss of protein homeostasis, or proteostasis, is a central hallmark of aging and helps to explain why these protein-folding diseases become manifest as organisms grow older[66].

In brain tissue, protein aggregation in neurons and subsequent neuronal death can lead to cognitive disease[67,68]. Neuron death in regions of the brain such as the hippocampus, well characterized for its involvement in memory, can lead to phenotypes of neurodegenerative disease[24]. Blockage of synapses by protein aggregation can also dysregulate neurotransmitter signaling in the brain, disrupt normal brain function, and lead to axonal dystrophy and neurodegeneration[69–71]. Protein synthesis is key in the formation of long-term memories, another central cognitive process thus affected by dysregulation of protein homeostasis[72,73].

Lipid metabolism and homeostasis in the brain are also crucial to maintaining a healthy brain[74]. At birth, around 50 percent of the human brain is made from phospholipids, declining to around 25% after age eight[75]. As organisms age, brain weight and volume decreases. In humans, this decline occurs particularly after the age of fifty[76]. Although lipids provide essential phospholipid membranes for cells and their organelles, and that much of the brain matter is made from lipid, accumulation of lipid droplets inside the cell has been associated with disease[77,78]. Specifically, in microglia lipid-droplet accumulation represents a dysfunctional and proinflammatory state in the aging brain[79].

How lipid synthesis rates change regionally in the brain with age is poorly understood. Through stable isotope labeling, we measured synthesis of palmitate and its subsequent incorporation into phospholipids in both the hippocampus, chosen for its involvement in memory, and the whole brain[80]. Previous groups have used alternative stable isotope labeling methods to measure rates of protein synthesis across regions of the brain, however, the question remains how these rates change with age[81]. Measurement of both protein replacement rates and *de novo* lipogenesis in the brain offer unique perspectives into the underlying biology of proteostasis in the aging brain and the cellular responses of aging. Through stable isotope labeling and mass spectrometric analysis, we have measured the altered metabolic processes and changes in *de novo* lipogenesis that occur with age across regions of the brain. Our dataset of region-specific protein and lipid dynamics in aged and young mice begins to reveal how homeostasis of these biomolecules changes across brain regions with age.

4.2 Results

Region-specific lipid synthesis

Region-specific measurement of palmitate synthesis and subsequent incorporation into phospholipids revealed significantly lower rates of synthesis in the hippocampus compared to the brain as a whole. However, these findings did not change as mice aged and there were no

significant differences in these brain region specific lipid synthesis rates in young compared to aged mice.

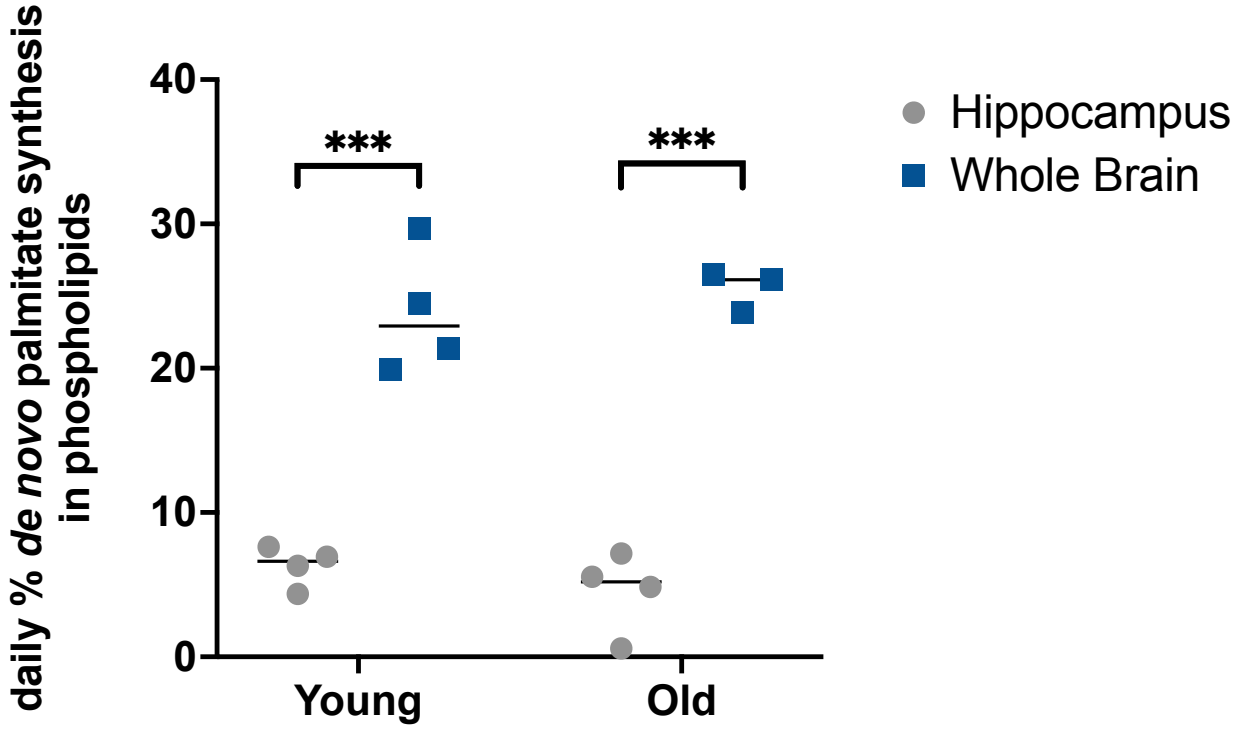

Figure 4.1. *De novo* lipogenesis fractional contribution to palmitate incorporated into phospholipids in 12-week-old and 80-week-old mice (n=3-5 per group). (b) DNL contribution to palmitate incorporated into phospholipids in 12-week-old control and tunicamycin treated mice (n=5 per group). (c) DNL contribution to palmitate incorporated into triglycerides in 80-week-old control and tunicamycin treated mice (n=5 per group). (d) DNL contribution to palmitate incorporated into phospholipids in 80-week-old control and tunicamycin treated mice (n=5 per group). ns= no significance, * = <0.05, ** = < 0.01, *** = < 0.001.

Region-specific global protein synthesis

Dynamic proteomics revealed no significant trends in global increase or decline of synthesis rates with age. However, many specific proteins were both up or down regulated in their synthesis rates in aged compared to young mice. Figure 4.2 highlights specific proteins significantly changed in their synthesis rate in aged compared to young mice in the cortex, hippocampus, and hypothalamus. To better understand global trends, we used KEGG analysis to view pathway specific changes that occur with age, displayed in figure 4.3. Table 4.1 demonstrates the ratio of aged to young protein synthesis rates for individual proteins measured in cortex, hippocampus, and hypothalamus.

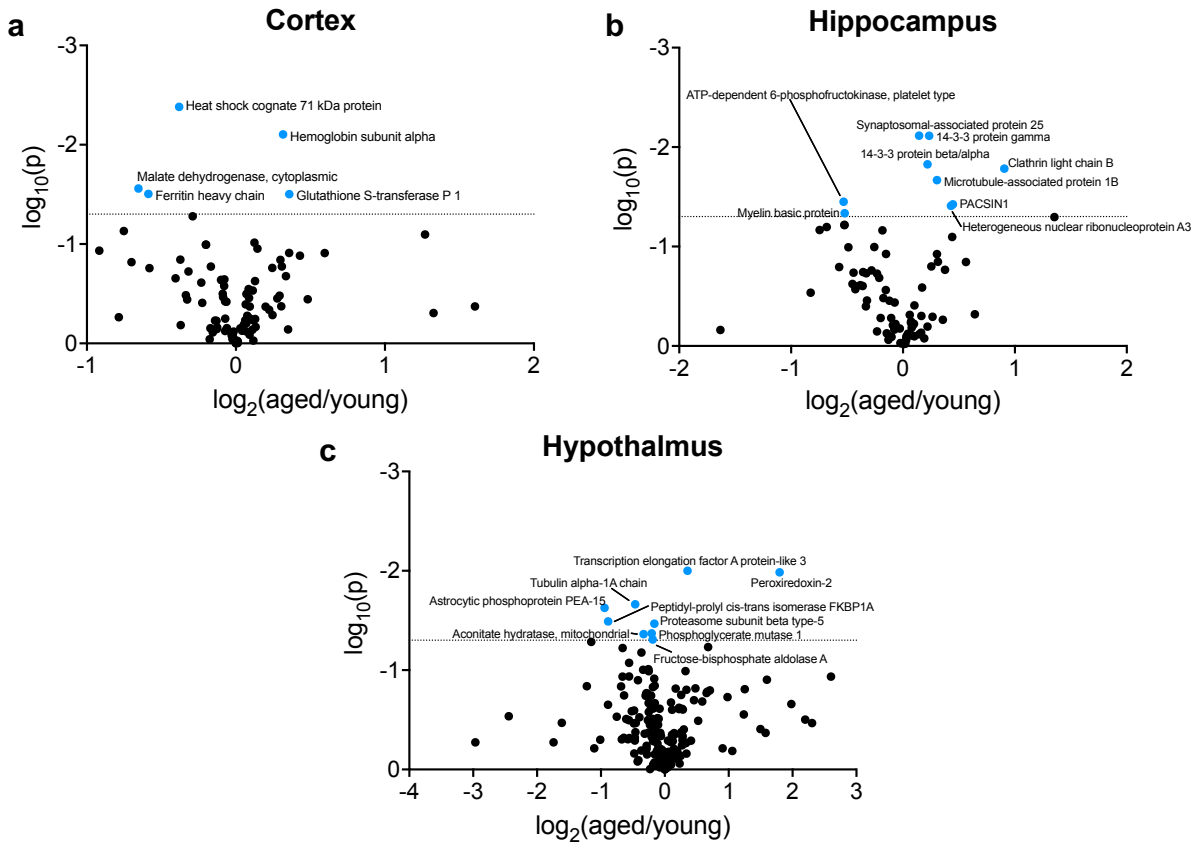

Figure 4.2. (a-c) Volcano plot of all proteins for which fractional synthesis rates were measured in isolated cortex, hypothalamus, and hippocampus. Points expressed as log2 fold-change aged/young on x-axis and - log10(p-value), obtained from 2-tailed t-test, on y-axis. Significantly changes proteins highlighted and labeled.

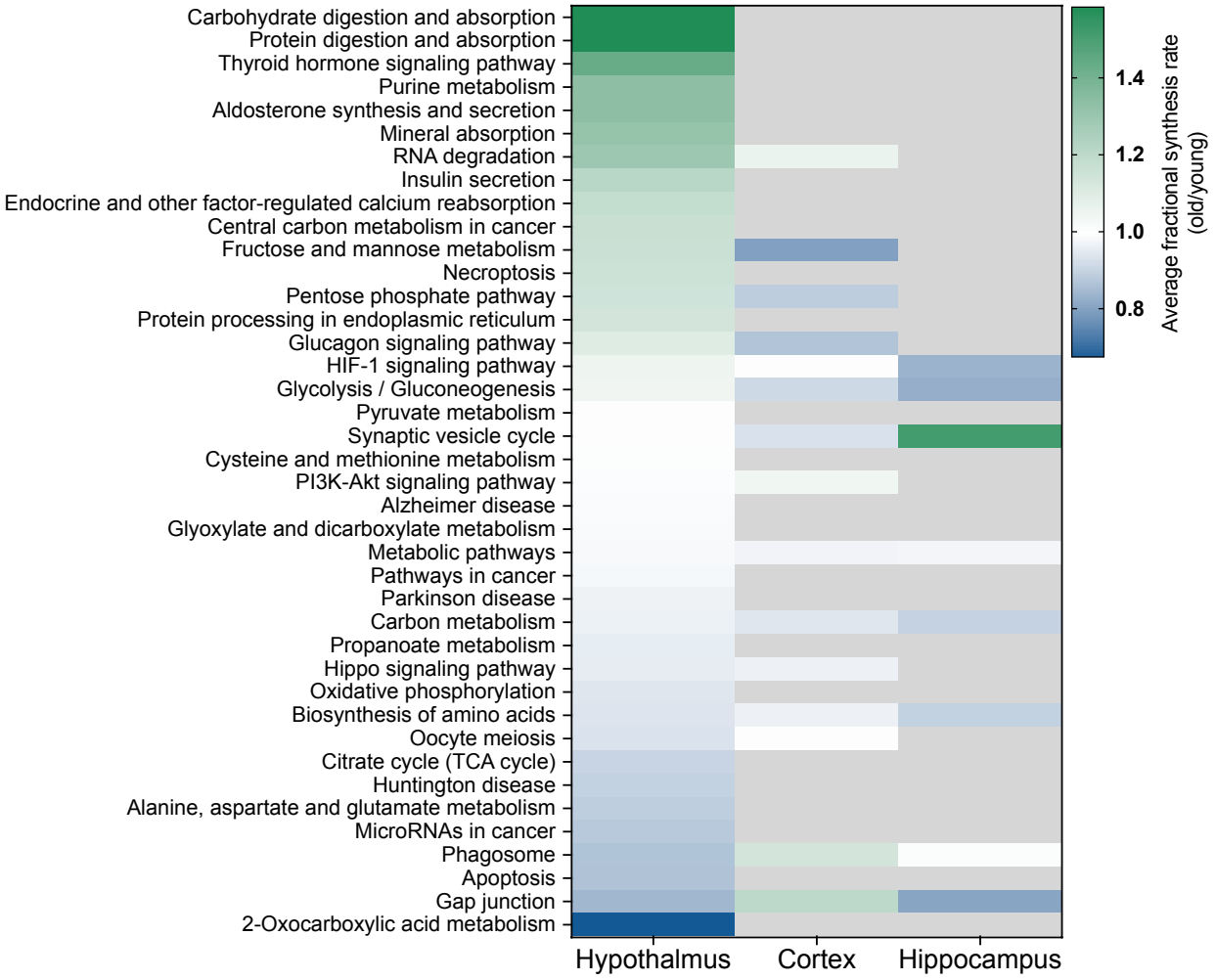

Figure 4.3. KEGG-pathway analysis for fractional synthesis rates of significant (p=<0.05 per 2-tailed t-test) proteins from aged/young mice in the hypothalamus, cortex, and hippocampus. n=at least 5 proteins per pathway.

Table 4.1. Individual protein synthesis rate ratios of aged/young mice. Ratio of above 1 indicates a higher synthesis rate with age. Ratio of below 1 indicates a lower synthesis rate with age.

	Synthesis rate ratio aged/young		
Protein	**Cortex**	**Hypothalamus**	**Hippocampus**
1-phosphatidylinositol 4,5-bisphosphate phosphodiesterase beta-1		0.95	
10 kDa heat shock protein, mitochondrial		0.85	
14-3-3 protein beta/alpha	0.94	0.90	1.16
14-3-3 protein epsilon		1.03	
14-3-3 protein eta		0.84	
14-3-3 protein gamma	0.94	0.95	1.18
14-3-3 protein theta	1.05	0.95	
14-3-3 protein zeta/delta	1.05	1.04	1.36
2-oxoglutarate dehydrogenase, mitochondrial		1.12	
2',3'-cyclic-nucleotide 3'-phosphodiesterase		0.54	
4-aminobutyrate aminotransferase, mitochondrial		0.88	
60 kDa heat shock protein, mitochondrial	0.89	1.98	1.06
60S acidic ribosomal protein P1		1.06	
78 kDa glucose-regulated protein		1.25	
Acetyl-CoA acetyltransferase, mitochondrial		0.85	
Aconitate hydratase, mitochondrial	1.01		
Aconitate hydratase, mitochondrial		0.79	
Actin-related protein 3		0.89	
Actin, alpha skeletal muscle	0.87	1.00	1.06
Actin, cytoplasmic 2	0.87	0.99	1.06
Acyl-CoA-binding protein		0.99	
Adenylate kinase isoenzyme 1	0.88	2.99	1.14
Adenylyl cyclase-associated protein 1			
ADP-ribosylation factor 5		1.87	
Alpha-centractin		0.46	
Alpha-enolase	1.26	0.93	0.74
Alpha-synuclein		1.05	

Amphiphysin		1.59	
Annexin A5		0.90	
AP-2 complex subunit alpha-2		0.13	
AP2-associated protein kinase 1	0.95	0.84	1.01
Aspartate aminotransferase, cytoplasmic		0.98	
Aspartate aminotransferase, mitochondrial		0.94	
Astrocytic phosphoprotein PEA-15		0.52	
ATP synthase subunit alpha, mitochondrial	1.28	1.11	0.85
ATP synthase subunit beta, mitochondrial		0.88	
ATP-dependent 6-phosphofructokinase, liver type		1.39	
ATP-dependent 6-phosphofructokinase, muscle type	0.80	1.17	
ATP-dependent 6-phosphofructokinase, platelet type	0.94	1.60	0.69
ATPase inhibitor, mitochondrial		1.22	
Band 4.1-like protein 3	1.23	1.04	
Beta-synuclein	1.18	1.21	0.93
Brain acid soluble protein 1	0.62	1.09	0.91
Brevican core protein		2.38	
Calbindin		0.95	
Calcium/calmodulin-dependent protein kinase type II subunit alpha		0.77	
Calmodulin-1		1.02	
Calreticulin		0.97	
Calretinin		1.03	
Carbonic anhydrase 2		0.83	
Cathepsin D		0.63	
Citrate synthase, mitochondrial	1.51	1.25	1.12
Clathrin coat assembly protein AP180	0.98	0.50	1.07
Clathrin heavy chain 1		0.75	
Clathrin light chain A	0.94	0.93	1.07
Clathrin light chain B	0.91	1.21	1.87
Cofilin-1	1.35	0.98	

Complexin-1	0.77	0.97	1.16
Complexin-2	1.07	0.90	1.20
Copper transport protein ATOX1		0.73	
Creatine kinase B-type	0.89	0.97	0.82
Creatine kinase U-type, mitochondrial		1.21	
Cullin-associated NEDD8-dissociated protein 1		0.70	
Cytochrome c, somatic		1.17	
Cytosolic acyl coenzyme A thioester hydrolase		1.26	
D-tyrosyl-tRNA(Tyr) deacylase 1		1.11	
Dihydrolipoyl dehydrogenase, mitochondrial		1.07	
Dihydropteridine reductase		0.99	
Dihydropyrimidinase-related protein 1	1.19	0.90	0.78
Dihydropyrimidinase-related protein 2	1.06	1.04	0.90
Dihydropyrimidinase-related protein 3	0.90		0.62
Dihydropyrimidinase-related protein 3		0.71	
Dynamin-1		1.10	
Dynein light chain 2, cytoplasmic		0.85	
Electron transfer flavoprotein subunit alpha, mitochondrial		0.72	
Elongation factor 1-alpha 1		0.76	
Elongation factor 1-alpha 2		1.06	
Endophilin-A1		0.96	
ES1 protein homolog, mitochondrial			
Eukaryotic translation initiation factor 4H	1.09	1.06	
Excitatory amino acid transporter 2	0.77		1.19
Fascin		0.62	
Fatty acid-binding protein, epidermal		0.89	
Ferritin heavy chain	0.67	1.00	0.85
Fructose-bisphosphate aldolase A	0.59		
Fructose-bisphosphate aldolase A		0.88	0.94
Fructose-bisphosphate aldolase C	1.09	1.03	0.86
Fumarate hydratase, mitochondrial		0.97	
Gamma-enolase	1.40	0.90	0.67

Glucose-6-phosphate isomerase		0.87	
Glutamate dehydrogenase 1, mitochondrial		0.92	
Glutamine synthetase	0.99	1.00	1.00
Glutathione S-transferase Mu 1		1.01	
Glutathione S-transferase P 1	1.28	0.99	0.79
Glyceraldehyde-3-phosphate dehydrogenase	0.93	0.86	1.05
Glycerol-3-phosphate dehydrogenase [NAD(		3.95	
Glycerol-3-phosphate phosphatase		0.88	
Glycogen phosphorylase, brain form			
Guanine deaminase		0.88	
Guanine nucleotide-binding protein G(I)/G(S)/G(T) subunit beta-1	1.24	0.72	
Heat shock 70 kDa protein 12A	1.08		
Heat shock 70 kDa protein 4		1.17	
Heat shock cognate 71 kDa protein	0.77	0.98	1.28
Heat shock protein HSP 90-alpha		0.73	
Heat shock protein HSP 90-beta		1.57	
Hematological and neurological expressed 1 protein	1.00	1.19	
Hemoglobin subunit alpha	1.25	0.88	1.13
Hemoglobin subunit beta-1		0.95	
Hemoglobin subunit beta-2		0.33	
Heterogeneous nuclear ribonucleoprotein A1	1.05		
Heterogeneous nuclear ribonucleoprotein A3	0.99	0.68	1.35
Heterogeneous nuclear ribonucleoprotein U	0.96		
Heterogeneous nuclear ribonucleoproteins A2/B1	1.00	0.96	1.04
High mobility group protein B1		2.82	
Histidine triad nucleotide-binding protein 1		1.14	0.98
Histone H2A type 1-F		1.26	
Isocitrate dehydrogenase [NAD] subunit alpha, mitochondrial	0.91		1.11
Ketimine reductase mu-crystallin		1.21	
L-lactate dehydrogenase A chain		1.03	

L-lactate dehydrogenase B chain	1.04	0.96	0.90
Lactoylglutathione lyase		0.82	
LIM and SH3 domain protein 1		1.03	
Malate dehydrogenase, cytoplasmic	0.64	0.93	1.02
Malate dehydrogenase, mitochondrial		1.12	
Metallothionein-3	1.01	1.04	1.05
Microtubule-associated protein 1A	0.96	1.26	0.98
Microtubule-associated protein 1B	1.04		1.23
Microtubule-associated protein 2	1.05	1.08	0.95
Microtubule-associated protein 4	0.82	0.66	0.80
Microtubule-associated protein 6	1.10	1.08	0.93
Microtubule-associated protein tau	1.08	0.89	1.30
Myelin basic protein	0.67	0.63	0.70
Nck-associated protein 1		0.30	
NEDD8		0.94	
Neurocalcin-delta		1.07	
Neurogranin	1.02		0.80
Neuromodulin	1.23	1.00	1.12
Neuron-specific calcium-binding protein hippocalcin	1.01	0.68	
Nucleophosmin		1.33	
Nucleoside diphosphate kinase A		1.03	
Nucleoside diphosphate kinase B		1.04	
Nucleosome assembly protein 1-like 4		0.99	
Peptidyl-prolyl cis-trans isomerase A	0.95	0.89	0.88
Peptidyl-prolyl cis-trans isomerase D		0.59	
Peptidyl-prolyl cis-trans isomerase FKBP1A		0.54	
Peroxiredoxin-1		0.81	
Peroxiredoxin-2		3.47	
Peroxiredoxin-5, mitochondrial		1.37	
Peroxiredoxin-6		1.03	
Phosphatidylethanolamine-binding protein 1		0.92	0.32
Phosphoglucomutase-1		1.23	

Phosphoglycerate kinase 1		1.02	
Phosphoglycerate kinase 2		0.84	
Phosphoglycerate mutase 1	0.53	0.87	0.77
ProSAAS		0.72	
Proteasome subunit beta type-5		0.89	
Protein disulfide-isomerase A3		1.01	
Protein DJ-1		0.43	
Protein kinase C and casein kinase substrate in neurons protein 1	0.95	0.75	1.36
Protein NDRG2	0.79	0.64	1.03
Protein phosphatase 1 regulatory subunit 1B	0.95		1.02
Protein phosphatase 1 regulatory subunit 7		6.07	
Protein-L-isoaspartate(D-aspartate) O-methyltransferase		2.08	
Purkinje cell protein 4		0.95	
Puromycin-sensitive aminopeptidase		0.95	
Pyridoxal kinase		0.83	
Pyruvate carboxylase, mitochondrial		2.36	1.48
Pyruvate dehydrogenase E1 component subunit beta, mitochondrial		1.50	
Pyruvate kinase PKM		0.84	
Rab GDP dissociation inhibitor alpha	1.15	0.95	0.87
Rab GDP dissociation inhibitor beta	1.27	0.90	0.56
Ras-related protein Rab-3A		0.68	
Retinal-specific ATP-binding cassette transporter		0.94	
Rho GDP-dissociation inhibitor 1		0.82	
Secernin-1	1.08	0.94	1.56
Secretogranin-2		0.92	
Septin-7		0.87	
Serine/threonine-protein phosphatase 2B catalytic subunit alpha isoform	1.05		0.99
Serotransferrin		0.87	
Serum albumin	1.06	0.92	1.02
Sodium/potassium-transporting ATPase subunit		0.72	

alpha-1			
Sodium/potassium-transporting ATPase subunit alpha-2		0.93	
Sodium/potassium-transporting ATPase subunit alpha-3		1.03	
Sodium/potassium-transporting ATPase subunit beta-1		4.59	
Sodium/potassium-transporting ATPase subunit beta-2		0.64	
Spectrin alpha chain, non-erythrocytic 1		4.95	
Stathmin	1.00	0.92	0.92
Stress-70 protein, mitochondrial	1.11	1.08	
Stress-induced-phosphoprotein 1		1.06	
Succinate-semialdehyde dehydrogenase, mitochondrial	0.86	0.63	0.60
Succinyl-CoA:3-ketoacid coenzyme A transferase 1, mitochondrial		0.74	
Superoxide dismutase [Cu-Zn]	1.08	1.01	0.84
Synapsin-1	1.09	1.21	1.24
Synapsin-2		0.88	
Synaptic vesicle glycoprotein 2A	2.41		
Synaptojanin-1	1.07	0.68	0.95
Synaptosomal-associated protein 25	1.05	1.63	1.10
Syntaxin-binding protein 1		3.03	
T-complex protein 1 subunit delta		1.03	
Tenascin-R		1.19	
Transaldolase		1.07	
Transcription elongation factor A protein-like 3	1.07	1.28	
Transgelin-3		0.88	
Transitional endoplasmic reticulum ATPase	1.21	1.44	1.07
Transketolase	1.03	1.08	0.95
Triosephosphate isomerase	0.58	0.91	
Tropomyosin alpha-1 chain		0.86	
Tropomyosin alpha-3 chain		0.92	
Tropomyosin beta chain		0.90	

Tubulin alpha chain-like 3		0.90	
Tubulin alpha-1A chain	0.98	0.72	0.70
Tubulin alpha-1B chain	0.99	0.79	0.70
Tubulin alpha-4A chain	0.80	0.85	0.75
Tubulin alpha-8 chain		0.89	
Tubulin beta-2A chain	0.91	0.90	1.23
Tubulin beta-2B chain		0.84	
Tubulin beta-3 chain	0.76	0.87	0.90
Tubulin beta-4A chain	1.17	0.85	0.78
Tubulin beta-4B chain	1.23	0.84	0.74
Tubulin beta-5 chain	0.95	0.78	0.71
Tubulin beta-6 chain	3.04	0.82	
Tubulin polymerization-promoting protein	0.85	0.88	0.73
Tubulin polymerization-promoting protein family member 3		0.95	
Ubiquitin carboxyl-terminal hydrolase isozyme L1	0.94	1.01	0.89
Ubiquitin-40S ribosomal protein S27a		1.02	
Ubiquitin-like modifier-activating enzyme 1	2.51	1.14	
UMP-CMP kinase		0.45	
V-type proton ATPase catalytic subunit A	1.06	0.97	2.55
V-type proton ATPase subunit B, brain isoform		1.09	
V-type proton ATPase subunit E 1		0.80	
V-type proton ATPase subunit G 2	0.92	0.82	
Vasopressin-neurophysin 2-copeptin		1.19	
Vesicle-associated membrane protein 2		0.18	
Vesicle-fusing ATPase		0.67	
Vimentin		0.82	

4.3 Discussion

Region-specific lipid synthesis

Hippocampus had significantly slower rates of lipid synthesis compared to whole brain lysate. Interestingly, these differences in region-specific lipid synthesis rates were not significant across ages. This leads us to believe that if lipid metabolism differences are seen with age, these changes are not derived from alternations in rates of local *de novo* lipogenesis in the brain. Interestingly,

de novo lipogenesis in the liver is significantly decreased with age, as discussed in chapter 3 (figure 3.6). The brain appears to be protected from this decline in lipogenesis.

Region-specific global protein synthesis

Through measuring rates of protein synthesis in young and aged mice in isolated hypothalamus, cortex, and hippocampus, we identified several notable region-specific KEGG pathway differences (figure 4.3). Metabolically, proteins involved in fructose and mannose metabolism and pentose phosphate pathways were synthesized at higher rates in the hypothalamus in aged mice compared to young mice, but synthesized at slower rates in the cortex of aged mice compared to young mice. Another notable difference is that the aged hippocampus had much higher synthesis rates of proteins involved in the synaptic vesicle cycle than the cortex and hippocampus regions compared to their young counterparts. As synaptic vesicles are involved in mediating neurotransmitter release[82], increased translation of synaptic vesicle proteins likely ties to either increased neurotransmitter release or a faulty feedback loop leading to increased translation of vesicles due to impaired trafficking or recycling[83]. Hypoxia inducible factor-1 (HIF-1) pathway signaling proteins were also synthesized at slower rates in aged mice hippocampus compared to aged cortex and hypothalamus compared to their young counterparts. Interestingly, HIF-1 has been well characterized for potential involvement in cancer progression[84,85], but also as a therapy for mitochondrial diseases[86]. Heat shock protein-71, an important chaperone, was synthesized at a significantly slower rate in aged cortex compared to young cortex, which could be related to decline in proteostasis seen with age.

While these experiments are preliminary, they demonstrate that stable isotope techniques can be applied to measure both global protein synthesis rates and *de novo* lipogenesis in a region-specific manner in the brain. These methods can be applied to better understand how and why distinct regions of the brain respond differently to aging. Understanding how protein and lipid metabolic flux signatures change with age-preventative interventions can help elucidate the mechanisms of emerging anti-aging therapeutics and preventative lifestyle changes. These techniques could be improved using methods to separate neurons from glia, providing a snapshot of the metabolic differences between brain cell types in different regions. It is likely that cell-type specific pathways deteriorate with age, causing detrimental aging phenotypes and the methods presented here could help understand these effects[87]. Overall, these preliminary findings indicate that developing flux signatures of the brain could provide a powerful tool to assess cell specific and region-specific changes with age, and give a metric to assess the effectiveness of anti-aging therapeutic interventions.

4.4 Materials and Methods

Animals

C57BL/6J male mice acquired from The Jackson Laboratory were used for this study. Mice were aged to either 12 or 80 weeks. All mice were housed according to the Animal Care and Use Committee (ACUC) standards in the animal facility at UC Berkeley. Mice were fed a standard chow diet and water ad libitum.

Deuterated water labeling and tunicamycin treatment in mice

Mice were labeled with deuterated water (heavy water, ^2H_2O) beginning at time point 0 (t^0) through the end of the experiment. Proteins synthesized after t^0 will incorporate deuterium-labeled amino

acids, thus enabling the measurement of proteins synthesized during the period of exposure to heavy water. Deuterium is rapidly incorporated throughout the body of an organism after treatment, bringing the deuterium enrichment in body water up to 5%. Deuterium enrichment is maintained through the intake of 8% $^{2}H_2O$ given as drinking water, thus making it an optimal labeling approach for *in vivo* experimental study. Mice are injected intraperitoneally (IP) with 100% $^{2}H_2O$ containing either tunicamycin dissolved in DMSO, or DMSO control. Tissues were harvested 96 hours after injections (n=5 mice per group).

Body water enrichment analysis
Mouse liver were distilled overnight upside down on a bead bath at 85°C to evaporate out body water. Deuterium present in the body water was exchanged onto acetone, and deuterium enrichment in the body water was measured via gas chromatography mass spectrometry (GC-MS)[52].

Tissue preparation for liquid chromatography-mass spectrometry (LC-MS)
Tissues were flash frozen after harvest and homogenized in homogenization buffer (100 mM PMSF, 500 mM EDTA, EDTA-free Protease Inhibitor Cocktail (Roche, catalog number 11836170001), PBS) using a 5 mm stainless steel bead at 30 hertz for 45 seconds in a TissueLyser II (Qiagen). Samples were then centrifuged at 10,000 rcf for 10 minutes at 4°C. The supernatant was saved and protein was quantified using a Pierce BCA protein assay kit (ThermoFisher, catalog number 23225). 100 ug of protein was used per sample. 25 uL of 100 mM ammonium bicarbonate solution, 25 uL TFE, and 2.3 uL of 200 mM DTT were added to each sample and incubated at 60°C for 1 hour. 10 uL 200 mM iodoacetamide was then added to each sample and allowed to incubate at room temperature in the dark for 1 hour. 2 uL of 200 mM DTT was added and samples were incubated for 20 minutes in the dark. Each sample was then diluted with 300 uL H_2O and 100 uL 100 mM ammonium bicarbonate solution. Trypsin was added at a ratio of 1:50 trypsin to protein (trypsin from porcine pancreas, Sigma Aldrich, catalog number T6567). Samples were incubated at 37°C overnight. The next day, 2 uL of formic acid was added. Samples were centrifuged at 10,000 rcf for 10 minutes, collecting the supernatant. Supernatant was speedvac'd until dry and re-suspended in 50 uL of 0.1 % formic acid/3% acetonitrile/96.9% LC-MS grade water and transferred to LC-MS vials to be analyzed via LC-MS.

Liquid chromatography-mass spectrometry (LC-MS) analysis
Trypsin-digested peptides were analyzed on a 6550 quadropole time of flight (Q-ToF) mass spectrometer equipped with Chip Cube nano ESI source (Agilent Technologies). High performance liquid chromatography (HPLC) separated the peptides using capillary and nano binary flow. Mobile phases were 95% acetonitrile/0.1% formic acid in LC-MS grade water. Peptides were eluted at 350 nl/minute flow rate with an 18 minute LC gradient. Each sample was analyzed once for protein/peptide identification in data-dependent MS/MS mode and once for peptide isotope analysis in MS mode. Acquired MS/MS spectra were extracted and searched using Spectrum Mill Proteomics Workbench software (Agilent Technologies) and a mouse protein database (www.uniprot.org). Search results were validated with a global false discovery rate of 1%. A filtered list of peptides was collapsed into a nonredundant peptide formula database containing peptide elemental composition, mass, and retention time. This was used to extract mass isotope abundances (M0-M3) of each peptide from MS-only acquisition files with Mass Hunter Qualitative Analysis software (Agilent Technologies). Mass isotopomer distribution analysis

(MIDA) was used to calculate peptide elemental composition and curve-fit parameters for predicting peptide isotope enrichment based on precursor body water enrichment (p) and the number (n) of amino acid C-H positions per peptide actively incorporating hydrogen (H) and deuterium (D) from body water. Subsequent data handling was performed using python-based scripts, with input of precursor body water enrichment for each subject, to yield fractional synthesis rate (FSR) data at the protein level. FSR data were filtered to exclude protein measurements with fewer than 2 peptide isotope measurements per protein. Details of FSR calculations and data filtering criteria were described previously[19].

Calculation of fractional replacement (f) and replacement rate constant (k) for individual proteins
Details of f calculations were previously described[15]. These values were used to generate the ratio of tunicamycin treated to untreated synthesis rates.

Statistical analysis
Data were analyzed using GraphPad Prism software (version 8.0).

Tissue preparation for gas chromatography-mass spectrometry (GC-MS)
A chloroform methanol extraction was used to isolate lipids from the liver tissue. These lipids were run on a thin-layer chromatography (TLC) plate to separate phospholipid and triglyceride fractions. These fractions containing the palmitate were further derivatized for GC-MS analysis.

Gas chromatography-mass spectrometry (GC-MS) analysis
Palmitate isotopic enrichments were measured by GC-MS (Agilent models 6890 and 5973; Agilent, Inc., Santa Clara, CA) using helium carrier gas, a DB-225 (DB 17 for cholesterol and DB 225 for palmitates) fused silica column (30M x 0.25mm ID x 0.25um), electron ionization mode, and monitoring m/z 385, 386, and 387 for palmitates for M0, M1, and M2 respectively, as previously described[53,54]. Palmitate methyl ester enrichments were determined by GC-MS using a DB-17 column (30M x 0.25mm ID x 0.25um), with helium as carrier gas, electron ionization mode, and monitoring m/z 270, 271, and 272 for M0, M1, and M2. Baseline unenriched standards for both analytes were measured concurrently to correct for abundance sensitivity.

Calculation of de novo lipogenesis (DNL)
The measurement of newly synthesized fatty acids formed during $^{2}H_2O$ labeling period was assessed using a combinatorial model of polymerization biosynthesis, as described previously[53,54]. Mass isotopomer distribution analysis (MIDA) along with body $^{2}H_2O$ enrichment, representing the precursor pool enrichment (p), is used to determine the theoretical maximum enrichment of each analyte. Using the measured deuterium enrichments, fractional and absolute contributions from DNL are then calculated. The value for f DNL represents the fraction of total triglyceride or phospholipid palmitate in the depot derived from DNL during the labeling period, and absolute DNL represents grams of palmitate synthesized by the DNL pathway.

KEGG pathway analysis
Protein fractional synthesis rates were weighted by the peptide count and averaged according to their KEGG pathway involvements. We used the Uniprot.ws package in R from Bioconductor to find mappings between UniProt accession numbers and their corresponding KEGG IDs for each protein. Tables were generated for the entire known proteome for mice. We then used the

Bio.KEGG module of Biopython in Python to access the REST API of the KEGG database to get a list of pathways to which each protein belongs. A set of all the pathways relevant to the experiment was generated and each protein and its corresponding fold change value were assigned to each pathway. KEGG pathways with no less than five proteins were used for representation of the data.

5. Conclusion and Future Outlook

Homeostasis of protein and lipid synthesis changes with age. These perturbations in kinetics lead to many diseases of aging, including metabolic and neurodegenerative diseases. Through better understanding how the global proteome changes with age and under diseased states, we can progress therapeutic research for diseases of aging. In summary, the data from my doctoral research extend the metabolic alterations invoked during the UPR^{ER} and their importance in metabolic homeostasis. I discovered that the source of accumulated lipid droplets and ER lipids during ER stress in the liver *in vivo* is from lipids taken up from outside the liver not synthesized *de novo* locally. Under ER stress conditions, key metabolic pathways including lipid and cholesterol synthesis are reduced while other pathways are perturbed in complex and not entirely predictable ways, including mobilization of lipids from adipose tissue to the liver. Prolonged disruption of these pathways may lead to progression of diseases involving altered lipid and protein homeostasis such as non-alcoholic fatty liver disease. The surprising source of liver lipids during ER stress conditions is useful as a differential pathogenic signature of ER stress in contrast to insulin-induced lipid accumulation in the liver, for example, where *de novo* lipogenesis is highly elevated[51]. These findings support that the UPR^{ER} may have implications for metabolic diseases characterized by accumulation of lipids.

Using the same stable isotope labeling technique, I discovered that aging leads to an exaggerated chronic ER stress metabolic signature in the liver, including suppressed synthesis of most protein ontologies, with the exception of protein processing in the ER, which remains upregulated. These data, in combination with higher BiP synthesis and dysregulated lipid metabolism in aged mice challenged with tunicamycin, indicate that aged mice are not as capable at handling and recovering from ER stress. They sustained high levels of BiP synthesis throughout the 4-day treatment period, whereas young mice showed less increase in BiP synthesis and no significant upregulation of *bip* mRNA. In summary, aging leads to breakdown in efficiency of the UPR, leading to the exaggerated UPR metabolic flux signature seen in these data.

Although chapters 2 and 3 focus on better understanding metabolic flux changes that occur under ER stress conditions in age, I wanted to apply these sample stable isotope labeling techniques to develop metabolic signatures of the brain due to its central involvement in diseases of aging. I demonstrate in chapter 4 the ability to apply stable isotope labeling using deuterated water treatment to develop region-specific metabolic flux signatures of the brain. Going forward, these metabolic flux signatures developed in chapter 4 could be applied to study metabolic differences between neurons and glia as organisms age, especially because metabolism can be quite different in these two cell types. Historically, glia have been thought of as support cells to neurons, however, recent work has unveiled their involved role as dynamic cells that sense neuronal metabolic changes and regular metabolism through transferring metabolites to neurons[88]. Glial cells play diverse roles in maintaining brain tissue homeostasis, much of which is just beginning to be discovered[89]. Through better understanding lipid metabolism as the brain ages, we can develop therapies to aid in treatment of age-related brain diseases such as neurodegeneration. Research supports that living an active lifestyle can perturb or delay onset of brain related diseases of aging[90]. However, little is understood about the connection between the broad metabolic changes caused by habitual exercise and region-specific effects on brain metabolism. Although most scientists can agree that lifestyle interventions, for example a healthy diet and regular exercise, can lead to healthier aging, scientists have worked for decades to generate anti-aging mimetics. One example includes a drug to slow down degradation of the blood brain barrier. The blood brain

barrier acts to protect the brain from unwanted circulating peripheral material, and aging and neurological disorders have been associated with blood brain barrier defects. As we age, our blood brain barrier becomes more permeable, thus allowing previously unwanted material into the brain. Albumin infiltration into the brain in particular has been shown to be involved in the pathogenesis of neurodegenerative diseases[91,92]. Through inhibition of transforming growth-factor β, known for its involvement in astrocyte signaling and cognitive impairments, aged mice showed reversal of the pathological aging phenotype usually associated with blood brain barrier decay[93]. Another promising anti-aging, or reversal of aging, therapy may one day include blood factors found to transfer the benefits of exercise in the aged brain[94]. After identifying glycosylphosphatidylinositol–specific phospholipase D1 as an important circulating factor post exercise, it was demonstrated to ameliorate age-related regenerative and cognitive impairments by altering signaling cascades downstream of GPI-anchored substrate cleavage. On the diet front, calorie restriction is another popular (and unpopular) anti-aging theory that has been well studied for its potential anti-aging, or slowed aging, effects. Through limiting calorie intake, a range of healthspan extending mechanisms have been proposed, although effect size in human studies has been found to be markedly more modest than across other model organisms studied[95–97]. Through the technologies discussed in this work, our lab has demonstrated that stable isotope labeling and subsequent quantification of newly synthesized lipids and proteins is a useful tool in assessing global changes in an organism to assess effectiveness and pathway specific differences with various anti-aging therapies, including calorie restriction[98,99]. By using the approaches characterized in my research, we can apply these techniques to gain a region-targeted broad-spectrum perspective of changes in protein and lipid synthesis, providing insight into how the brain changes with age and how preventative measures, for example drugs that improve blood brain barrier integrity and exercise mimetics, affect these metabolic signatures. Assessing how metabolic flux signatures of the brain are perturbed through different interventions, including anti-aging therapeutics and preventative lifestyle interventions, could provide a powerful tool to assess cell-specific and region-specific changes with age, and provide a metric to assess intervention effectiveness.

References

1. Frakes AE, Dillin A. The UPRER: Sensor and Coordinator of Organismal Homeostasis. *Mol Cell*. 2017;66(6):761-771.
2. Wang M, Kaufman RJ. Protein misfolding in the endoplasmic reticulum as a conduit to human disease. *Nature*. 2016;529(7586):326-335.
3. Salvadó L, Palomer X, Barroso E, Vázquez-Carrera M. Targeting endoplasmic reticulum stress in insulin resistance. *Trends Endocrinol Metab*. 2015;26(8):438-448.
4. Fu S, Watkins SM, Hotamisligil GS. The role of endoplasmic reticulum in hepatic lipid homeostasis and stress signaling. *Cell Metab*. 2012;15(5):623-634.
5. Cnop M, Foufelle F, Velloso LA. Endoplasmic reticulum stress, obesity and diabetes. *Trends Mol Med*. 2012;18(1):59-68.
6. Rutkowski DT, Wu J, Back S-H, et al. UPR pathways combine to prevent hepatic steatosis caused by ER stress-mediated suppression of transcriptional master regulators. *Dev Cell*. 2008;15(6):829-840.
7. Rutkowski DT. Liver function and dysfunction - a unique window into the physiological reach of ER stress and the unfolded protein response. *FEBS J*. 2019;286(2):356-378.
8. Hotamisligil GS. Endoplasmic reticulum stress and the inflammatory basis of metabolic disease. *Cell*. 2010;140(6):900-917.
9. Bertolotti A, Zhang Y, Hendershot LM, Harding HP, Ron D. Dynamic interaction of BiP and ER stress transducers in the unfolded-protein response. *Nat Cell Biol*. 2000;2(6):326-332.
10. Walter P, Ron D. The Unfolded Protein Response: From Stress Pathway to Homeostatic Regulation. *Science*. 2011;334(6059):1081-1086. doi:10.1126/science.1209038
11. Lee J-S, Mendez R, Heng HH, Yang Z-Q, Zhang K. Pharmacological ER stress promotes hepatic lipogenesis and lipid droplet formation. *Am J Transl Res*. 2012;4(1):102-113.
12. DeZwaan-McCabe D, Sheldon RD, Gorecki MC, et al. ER Stress Inhibits Liver Fatty Acid Oxidation while Unmitigated Stress Leads to Anorexia-Induced Lipolysis and Both Liver and Kidney Steatosis. *Cell Rep*. 2017;19(9):1794-1806.
13. Herrema H, Zhou Y, Zhang D, et al. XBP1s Is an Anti-lipogenic Protein. *J Biol Chem*. 2016;291(33):17394-17404.
14. Schuck S, Prinz WA, Thorn KS, Voss C, Walter P. Membrane expansion alleviates endoplasmic reticulum stress independently of the unfolded protein response. *J Cell Biol*. 2009;187(4):525-536.
15. Taylor RC, Dillin A. Aging as an event of proteostasis collapse. *Cold Spring Harb Perspect Biol*. 2011;3(5). doi:10.1101/cshperspect.a004440
16. Taylor RC, Dillin A. XBP-1 is a cell-nonautonomous regulator of stress resistance and longevity. *Cell*. 2013;153(7):1435-1447.
17. Hellerstein MK, Neese RA. Mass isotopomer distribution analysis at eight years: theoretical, analytic, and experimental considerations. *Am J Physiol*. 1999;276(6):E1146-E1170.
18. Hellerstein MK, Neese RA. Mass isotopomer distribution analysis: a technique for measuring biosynthesis and turnover of polymers. *Am J Physiol*. 1992;263(5 Pt 1):E988-E1001.
19. Holmes WE, Angel TE, Li KW, Hellerstein MK. Dynamic Proteomics: In Vivo Proteome-Wide Measurement of Protein Kinetics Using Metabolic Labeling. *Methods Enzymol*. 2015;561:219-276.
20. Hudgins LC, Parker TS, Levine DM, Hellerstein MK. A dual sugar challenge test for

lipogenic sensitivity to dietary fructose. *J Clin Endocrinol Metab*. 2011;96(3):861-868.
21. Wyss-Coray T. Ageing, neurodegeneration and brain rejuvenation. *Nature*. 2016;539(7628):180-186.
22. Weissberg I, Wood L, Kamintsky L, et al. Albumin induces excitatory synaptogenesis through astrocytic TGF-β/ALK5 signaling in a model of acquired epilepsy following blood–brain barrier dysfunction. *Neurobiol Dis*. 2015;78:115-125.
23. Mattson MP, Arumugam TV. Hallmarks of Brain Aging: Adaptive and Pathological Modification by Metabolic States. *Cell Metab*. 2018;27(6):1176-1199.
24. Agranoff BW, Davis RE, Brink JJ. Memory fixation in the goldfish. *Proc Natl Acad Sci U S A*. 1965;54(3):788-793.
25. Saez I, Vilchez D. The Mechanistic Links Between Proteasome Activity, Aging and Agerelated Diseases. *Curr Genomics*. 2014;15(1):38-51.
26. Vilchez D, Saez I, Dillin A. The role of protein clearance mechanisms in organismal ageing and age-related diseases. *Nat Commun*. 2014;5:5659.
27. Tanaka K, Matsuda N. Proteostasis and neurodegeneration: the roles of proteasomal degradation and autophagy. *Biochim Biophys Acta*. 2014;1843(1):197-204.
28. Massey AC, Kaushik S, Sovak G, Kiffin R, Cuervo AM. Consequences of the selective blockage of chaperone-mediated autophagy. *Proc Natl Acad Sci U S A*. 2006;103(15):5805-5810.
29. Lipinski MM, Zheng B, Lu T, et al. Genome-wide analysis reveals mechanisms modulating autophagy in normal brain aging and in Alzheimer's disease. *Proc Natl Acad Sci U S A*. 2010;107(32):14164-14169.
30. Schneider CP, Peng L, Yuen S, et al. Metabolic flux signatures of the ER unfolded protein response in vivo reveal decreased hepatic de novo lipogenesis and mobilization of lipids from adipose tissue to liver. *bioRxiv*. Published online October 29, 2020:2020.10.29.360073. doi:10.1101/2020.10.29.360073
31. Neese RA, Faix D, Kletke C, et al. Measurement of endogenous synthesis of plasma cholesterol in rats and humans using MIDA. *Am J Physiol*. 1993;264(1 Pt 1):E136-E147.
32. Turner SM, Murphy EJ, Neese RA, et al. Measurement of TG synthesis and turnover in vivo by 2H2O incorporation into the glycerol moiety and application of MIDA. *Am J Physiol Endocrinol Metab*. 2003;285(4):E790-E803.
33. Mohan S, R PRM, Brown L, Ayyappan P, G RK. Endoplasmic reticulum stress: A master regulator of metabolic syndrome. *Eur J Pharmacol*. 2019;860:172553.
34. Ron D, Walter P. Signal integration in the endoplasmic reticulum unfolded protein response. *Nat Rev Mol Cell Biol*. 2007;8(7):519-529.
35. Rendleman J, Cheng Z, Maity S, et al. New insights into the cellular temporal response to proteostatic stress. *Elife*. 2018;7:e39054.
36. Reid DW, Chen Q, Tay ASL, Shenolikar S, Nicchitta CV. The unfolded protein response triggers selective mRNA release from the endoplasmic reticulum. *Cell*. Published online 2014. https://www.sciencedirect.com/science/article/pii/S0092867414010435
37. Shankaran M, King CL, Angel TE, et al. Circulating protein synthesis rates reveal skeletal muscle proteome dynamics. *J Clin Invest*. 2016;126(1):288-302.
38. Greenbaum D, Colangelo C, Williams K, Gerstein M. Comparing protein abundance and mRNA expression levels on a genomic scale. *Genome Biol*. 2003;4(9):117.
39. Liu Y, Beyer A, Aebersold R. On the dependency of cellular protein levels on mRNA abundance. *Cell*. Published online 2016.

https://www.sciencedirect.com/science/article/pii/S0092867416302707
40. Maier T, Güell M, Serrano L. Correlation of mRNA and protein in complex biological samples. *FEBS Lett*. 2009;583(24):3966-3973.
41. Vandewynckel Y-P, Laukens D, Bogaerts E, et al. Modulation of the unfolded protein response impedes tumor cell adaptation to proteotoxic stress: a PERK for hepatocellular carcinoma therapy. *Hepatol Int*. 2015;9(1):93-104.
42. Borgese N, Francolini M, Snapp E. Endoplasmic reticulum architecture: structures in flux. *Curr Opin Cell Biol*. 2006;18(4):358-364.
43. Daniele JR, Higuchi-Sanabria R, Durieux J, et al. UPRER promotes lipophagy independent of chaperones to extend life span. *Sci Adv*. 2020;6(1):eaaz1441.
44. Sriburi R, Jackowski S, Mori K, Brewer JW. XBP1: a link between the unfolded protein response, lipid biosynthesis, and biogenesis of the endoplasmic reticulum. *J Cell Biol*. 2004;167(1):35-41.
45. Colgan SM, Tang D, Werstuck GH, Austin RC. Endoplasmic reticulum stress causes the activation of sterol regulatory element binding protein-2. *Int J Biochem Cell Biol*. 2007;39(10):1843-1851.
46. Kim KE, Jung Y, Min S, et al. Caloric restriction of db/db mice reverts hepatic steatosis and body weight with divergent hepatic metabolism. *Sci Rep*. 2016;6:30111.
47. Han J, Kaufman RJ. The role of ER stress in lipid metabolism and lipotoxicity. *J Lipid Res*. 2016;57(8):1329-1338.
48. Ho N, Yap WS, Xu J, et al. Stress sensor Ire1 deploys a divergent transcriptional program in response to lipid bilayer stress. *J Cell Biol*. 2020;219(7). doi:10.1083/jcb.201909165
49. Estrada AL, Hudson WM, Kim PY, et al. Short-term changes in diet composition do not affect in vivo hepatic protein synthesis in rats. *Am J Physiol Endocrinol Metab*. 2018;314(3):E241-E250.
50. Fu S, Fan J, Blanco J, et al. Polysome profiling in liver identifies dynamic regulation of endoplasmic reticulum translatome by obesity and fasting. *PLoS Genet*. 2012;8(8):e1002902.
51. Smith GI, Mittendorfer B, Klein S. Metabolically healthy obesity: facts and fantasies. *J Clin Invest*. 2019;129(10):3978-3989.
52. Yang D, Diraison F, Beylot M, et al. Assay of Low Deuterium Enrichment of Water by Isotopic Exchange with [U-13C3]Acetone and Gas Chromatography–Mass Spectrometry. *Analytical Biochemistry*. 1998;258(2):315-321. doi:10.1006/abio.1998.2632
53. Hellerstein MK, Neese RA, Letscher A, Linfoot P, Turner S. Hepatic glucose-6-phosphatase flux and glucose phosphorylation, cycling, irreversible disposal, and net balance in vivo in rats. Measurement using the secreted glucuronate technique. *Metabolism*. 1997;46(12):1390-1398.
54. Hellerstein MK, Christiansen M, Kaempfer S, et al. Measurement of de novo hepatic lipogenesis in humans using stable isotopes. *J Clin Invest*. 1991;87(5):1841-1852.
55. Eden E, Navon R, Steinfeld I, Lipson D, Yakhini Z. GOrilla: a tool for discovery and visualization of enriched GO terms in ranked gene lists. *BMC Bioinformatics*. 2009;10:48.
56. Schneider CP, Peng L, Yuen S, Halstead J, Palacios H. Aging alters the metabolic flux signature of the ER unfolded protein response in vivo in mice. *bioRxiv*. Published online 2021. https://www.biorxiv.org/content/10.1101/2021.04.14.439896v1.abstract
57. Gardner BM, Walter P. Unfolded proteins are Ire1-activating ligands that directly induce the unfolded protein response. *Science*. 2011;333(6051):1891-1894.

58. Sano R, Reed JC. ER stress-induced cell death mechanisms. *Biochim Biophys Acta*. 2013;1833(12):3460-3470.
59. Hotamisligil GS. Inflammation and metabolic disorders. *Nature*. 2006;444(7121):860-867.
60. Harding HP, Zhang Y, Bertolotti A, Zeng H, Ron D. Perk is essential for translational regulation and cell survival during the unfolded protein response. *Mol Cell*. 2000;5(5):897-904.
61. van Meer G, Voelker DR, Feigenson GW. Membrane lipids: where they are and how they behave. *Nat Rev Mol Cell Biol*. 2008;9(2):112-124.
62. Volmer R, Ron D. Lipid-dependent regulation of the unfolded protein response. *Curr Opin Cell Biol*. 2015;33:67-73.
63. Lee K, Tirasophon W, Shen X, et al. IRE1-mediated unconventional mRNA splicing and S2P-mediated ATF6 cleavage merge to regulate XBP1 in signaling the unfolded protein response. *Genes Dev*. 2002;16(4):452-466.
64. Beysen C, Angel TE, Hellerstein MK, Turner SM. Isotopic Tracers for the Measurement of Metabolic Flux Rates. In: Krentz AJ, Weyer C, Hompesch M, eds. *Translational Research Methods in Diabetes, Obesity, and Nonalcoholic Fatty Liver Disease: A Focus on Early Phase Clinical Drug Development*. Springer International Publishing; 2019:211-243.
65. Circu ML, Aw TY. Glutathione and modulation of cell apoptosis. *Biochim Biophys Acta*. 2012;1823(10):1767-1777.
66. Lim J, Yue Z. Neuronal aggregates: formation, clearance, and spreading. *Dev Cell*. 2015;32(4):491-501.
67. Hetz C, Mollereau B. Disturbance of endoplasmic reticulum proteostasis in neurodegenerative diseases. *Nat Rev Neurosci*. 2014;15(4):233-249.
68. Hetz C, Saxena S. ER stress and the unfolded protein response in neurodegeneration. *Nat Rev Neurol*. 2017;13(8):477-491.
69. Alvarez-Castelao B, Schuman EM. The Regulation of Synaptic Protein Turnover. *J Biol Chem*. 2015;290(48):28623-28630.
70. Martinez-Vicente M, Cuervo AM. Autophagy and neurodegeneration: when the cleaning crew goes on strike. *Lancet Neurol*. 2007;6(4):352-361.
71. Neefjes J, van der Kant R. Stuck in traffic: an emerging theme in diseases of the nervous system. *Trends Neurosci*. 2014;37(2):66-76.
72. Davis HP, Squire LR. Protein synthesis and memory: a review. *Psychol Bull*. 1984;96(3):518-559.
73. Sweeney P, Park H, Baumann M, et al. Protein misfolding in neurodegenerative diseases: implications and strategies. *Translational Neurodegeneration*. 2017;6(1). doi:10.1186/s40035-017-0077-5
74. Adibhatla RM, Hatcher JF. Role of Lipids in Brain Injury and Diseases. *Future Lipidol*. 2007;2(4):403-422.
75. Dawson G. Measuring brain lipids. *Biochim Biophys Acta*. 2015;1851(8):1026-1039.
76. Conde JR, Streit WJ. Microglia in the aging brain. *J Neuropathol Exp Neurol*. 2006;65(3):199-203.
77. Greenberg AS, Coleman RA, Kraemer FB, et al. The role of lipid droplets in metabolic disease in rodents and humans. *J Clin Invest*. 2011;121(6):2102-2110.
78. Krahmer N, Farese RV Jr, Walther TC. Balancing the fat: lipid droplets and human disease. *EMBO Mol Med*. 2013;5(7):973-983.
79. Marschallinger J, Iram T, Zardeneta M, et al. Lipid-droplet-accumulating microglia

represent a dysfunctional and proinflammatory state in the aging brain. *Nat Neurosci*. 2020;23(2):194-208.
80. Morrison JH, Hof PR. Life and death of neurons in the aging brain. *Science*. 1997;278(5337):412-419.
81. Fornasiero EF, Mandad S, Wildhagen H, et al. Precisely measured protein lifetimes in the mouse brain reveal differences across tissues and subcellular fractions. *Nat Commun*. 2018;9(1):4230.
82. Sudhof TC. The synaptic vesicle cycle. *Annu Rev Neurosci*. 2004;27:509-547.
83. Shupliakov O, Bloom O, Gustafsson JS, et al. Impaired recycling of synaptic vesicles after acute perturbation of the presynaptic actin cytoskeleton. *Proc Natl Acad Sci U S A*. 2002;99(22):14476-14481.
84. Lee JW, Ko J, Ju C, Eltzschig HK. Hypoxia signaling in human diseases and therapeutic targets. *Exp Mol Med*. 2019;51(6):1-13.
85. Masoud GN, Li W. HIF-1α pathway: role, regulation and intervention for cancer therapy. *Acta Pharm Sin B*. 2015;5(5):378-389.
86. Jain IH, Zazzeron L, Goli R, et al. Hypoxia as a therapy for mitochondrial disease. *Science*. 2016;352(6281):54-61.
87. López-Otín C, Blasco MA, Partridge L, Serrano M, Kroemer G. The hallmarks of aging. *Cell*. 2013;153(6):1194-1217.
88. Jha MK, Morrison BM. Glia-neuron energy metabolism in health and diseases: New insights into the role of nervous system metabolic transporters. *Exp Neurol*. 2018;309:23-31.
89. Afridi R, Kim J-H, Rahman MH, Suk K. Metabolic Regulation of Glial Phenotypes: Implications in Neuron-Glia Interactions and Neurological Disorders. *Front Cell Neurosci*. 2020;14:20.
90. Kramer AF, Erickson KI, Colcombe SJ. Exercise, cognition, and the aging brain. *J Appl Physiol*. 2006;101(4):1237-1242.
91. Bar-Klein G, Cacheaux LP, Kamintsky L, et al. Losartan prevents acquired epilepsy via TGF-β signaling suppression. *Ann Neurol*. 2014;75(6):864-875.
92. Cacheaux LP, Ivens S, David Y, et al. Transcriptome profiling reveals TGF-beta signaling involvement in epileptogenesis. *J Neurosci*. 2009;29(28):8927-8935.
93. Senatorov VV Jr, Friedman AR, Milikovsky DZ, et al. Blood-brain barrier dysfunction in aging induces hyperactivation of TGFβ signaling and chronic yet reversible neural dysfunction. *Sci Transl Med*. 2019;11(521). doi:10.1126/scitranslmed.aaw8283
94. Horowitz AM, Fan X, Bieri G, et al. Blood factors transfer beneficial effects of exercise on neurogenesis and cognition to the aged brain. *Science*. 2020;369(6500):167-173.
95. Redman LM, Smith SR, Burton JH, Martin CK, Il'yasova D, Ravussin E. Metabolic Slowing and Reduced Oxidative Damage with Sustained Caloric Restriction Support the Rate of Living and Oxidative Damage Theories of Aging. *Cell Metab*. 2018;27(4):805-815.e4.
96. Fontana L, Villareal DT, Das SK, et al. Effects of 2-year calorie restriction on circulating levels of IGF-1, IGF-binding proteins and cortisol in nonobese men and women: a randomized clinical trial. *Aging Cell*. 2016;15(1):22-27.
97. Ravussin E, Redman LM, Rochon J, et al. A 2-Year Randomized Controlled Trial of Human Caloric Restriction: Feasibility and Effects on Predictors of Health Span and Longevity. *J Gerontol A Biol Sci Med Sci*. 2015;70(9):1097-1104.
98. Thompson ACS, Bruss MD, Price JC, et al. Reduced in vivo hepatic proteome replacement

rates but not cell proliferation rates predict maximum lifespan extension in mice. *Aging Cell*. 2016;15(1):118-127.
99. Price JC, Khambatta CF, Li KW, et al. The effect of long term calorie restriction on in vivo hepatic proteostatis: a novel combination of dynamic and quantitative proteomics. *Mol Cell Proteomics*. 2012;11(12):1801-1814.